

Sub-mesoscale Dynamics in the Southern Ocean

Isabella Rosso

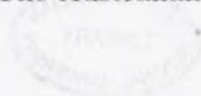
*Research School of Earth Sciences, The Australian National University
Australian Research Council Centre of Excellence in Climate System Science*

and

*Commonwealth Scientific and Industrial Research Organisation
Wealth from Oceans Flagship*

April, 2015

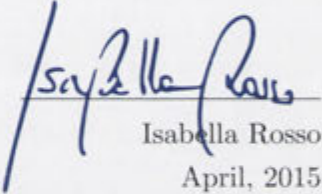
This thesis is submitted for the degree of Doctor of Philosophy
of The Australian National University



Declaration

This thesis is an account of research undertaken between March 2011 and April 2015 at the Research School of Earth Sciences, The Australian National University, Canberra, Australia.

Except where acknowledged in the customary manner, the material presented in this thesis is, to the best of my knowledge, original and has not been submitted in whole or part for a degree in any university.



Isabella Rosso
April, 2015

Abstract

The Southern Ocean circulation is dominated by the Antarctic Circumpolar Current (ACC), a quasi-zonal current that encircles Antarctica. Typical features of the ACC are an energetic eddy field and jets that influence both the large scale flow and heat and carbon fluxes and, consequently, impact the climate system. Due to the strong zonal flow and weak stratification of the Southern Ocean, topography steers and influences the ACC. For example, Rossby waves or stationary meanders can be found in the lee of topographic features and the structure of jets and fronts can be modified by topography. ACC dynamics are very complex and understanding these dynamics is crucial, given the Southern Ocean role in the global climate system.

The Southern Ocean is an environment where, despite a large nutrient availability, the biological productivity is very low. This biological activity is limited by light irradiance and iron availability. However, there exist several locations in the Southern Ocean where, due to a natural iron fertilisation, phytoplankton blooms can be observed. One such location is the Kerguelen Plateau (KP) region in the south Indian Ocean.

Numerous physical mechanisms that drive iron into the euphotic zone of KP waters have been identified. However, in these studies sub-mesoscale dynamics, occurring at horizontal scales of several kilometers, have never been included and their contribution to the iron supply never estimated. These structures have been seen to dramatically trigger an ecosystem response in other parts of the ocean, suggesting that they might represent a significant contribution to Southern Ocean blooms.

This thesis is focused on the development and analysis of the first sub-mesoscale-resolving ($1/80^\circ$ resolution) ocean model of the KP area. Resolving sub-mesoscale structures results in an enhancement of vertical velocities and transport, compared to mesoscale-resolving simulations ($1/20^\circ$).

Results show that sub-mesoscale fields, such as eddy kinetic energy or vertical velocities, are spatially inhomogeneous. Evidence is presented that this inhomogeneity is strongly related to the topographic features of this region. In particular, it is in part due to internal waves excited by the interaction of the large-scale flow with topography and largely due to an indirect generation by the topography: topography controls mesoscale flows, which in turn generate sub-mesoscale activity. The correlation between mesoscale eddy kinetic energy and strain rate fields with sub-mesoscale vertical velocities suggests a possible new route to parameterise sub-mesoscales in coarser resolution models.

The modelled velocity field is used to advect Lagrangian particles. The $1/80^\circ$ resolution experiments are compared to the $1/20^\circ$ case, finding that waters reach greater depths at the highest resolution. Built on these Lagrangian experiments is the development of an innovative technique for the study of iron supply, used to contrast the contribution of

mesoscales and sub-mesoscales. This technique highlights the sensitivity of iron supply to the horizontal resolution, showing a clear enhancement of iron fluxes (by a factor of 2) at higher resolution. Thus, the vertical motion induced by the sub-mesoscales represents a new process to drive iron into the euphotic waters of the KP region.

Acknowledgements

*Sometimes you wake up. Sometimes the fall kills you.
And sometimes, when you fall, you fly.*
Neil Gaiman, The Sandman

I would like to give my first and special thanks to my supervisor Andy Hogg. There is no exaggeration in admitting that, without his constant support, encouragement, criticism and valuable guidance, I would not have had the strength and courage to pursue my dream to be, one day, an oceanographer. Certainly, I would not be here, writing these lines. He represented a beacon in my “darker-than-a-moonless-night” falls (which have been more than sporadic during these 4 years of Ph.D. life). He has been an inspiration and a mentor to me, and a true example of what a successful oceanographer should be. With his guidance, my expertise grew parallel to my confidence. There are really no words to express my gratitude towards him.

My gratitude goes also to my advisor Andrew Kiss, whose encouragement and guidance have been equally precious and have helped me to direct my research in a more precise and comprehensive way. Through long and very productive discussions, I learnt to take my research to new depths and to investigate my questions with more accuracy.

It has been a real pleasure not only to work with both of them, but also to share numerous and beautiful life experiences, all of which have helped to make my years in Australia a wonderful journey.

I am also very grateful for the opportunity I had to collaborate with Peter Strutton and Richard Matear, both of whom were a part of my supervisory panel. They provided indispensable guidance that allowed me to direct my work along a biological (and very mysterious) route and explore the extremely complicated interconnection between the biological and physical components of the ocean.

My gratitude goes also to Bishakh Gayen, for the fundamental guidance on internal waves physics to the second Chapter of my thesis. For the multiple discussions, helpful comments and suggestions, I am very grateful to Stephanie Downes and Maxim Nikurashin. I must also thank Helen Phillips, Liam Brannigan and Shane Keating for constructive discussions, Rosemary Morrow for providing the altimetry regional Kerguelen experimental product from AVISO and Matthew Mazloff for providing the SOSE fields used throughout the simulations. Numerical simulations and analyses were conducted using the National Facility of the Australian National Computational Infrastructure.

This section cannot continue without thanking the people who had represented, or

still represent, the soul of the GFD group at RSES. They have never lacked in offering me advice, providing valuable discussions or capitalising on every occasion to have fun together. With their enthusiasm in celebrating life, my social time here has been unpredictable, joyful and rich. Thereby, my thoughts go especially to Adele, Kate, Marshall, Andy, Juan and Natanya, Claire and Christopher, Madi, Steph, Bishakh and Yvan.

To Magda, Malte, Nur and TheBella I owe my profound gratitude. For all the fun, the ocean trips, the chats, the dinners, the movies (and the bites of TheBella). With their friendship here, my life has been incredibly beautiful and never solitary. And my special gratitude goes to my friends Nick, Paul, Bernie, Bojana, Veronica and Stu, for their love, enthusiasm and constant support.

Finally, my deepest thanks go to my husband Diego, my friend Chiara and my family, for their constant support of my choice, with unconditional love and faith. They have clearly taught me that any physical distance separating us is actually nothing more than an empty concept. To them, I dedicate this work.

Contents

Declaration	iii
Abstract	v
Acknowledgements	vii
Contents	x
Figures	xvi
Tables	xvii
Preamble	xix
1 Introduction	1
1.1 The Southern Ocean circulation	1
1.2 Biological activity in the Southern Ocean	3
1.3 Sub-mesoscale dynamics	6
1.4 The Kerguelen Plateau	8
1.5 Research orientation	10
2 Vertical transport in the ocean due to sub-mesoscale structures: Impacts in the Kerguelen region	11
2.1 Introduction	11
2.2 Method	13
2.2.1 MITgcm configuration for 1/20° resolution	14
2.2.2 MITgcm configuration for 1/80° resolution	15
2.2.3 Connectivity Modelling System	15
2.3 Model evaluation	18
2.4 Results	21
2.4.1 Frontal structures	21
2.4.2 Particle analysis	28
2.5 Discussion and conclusions	32
3 Topographic influence on sub-mesoscale dynamics in the Southern Ocean	37
3.1 Introduction	37
3.2 Methods	38

3.3	Results	39
3.3.1	Frontal structures	39
3.3.2	Causes of patchiness	42
3.3.3	A proxy for sub-mesoscales	46
3.4	Conclusions	47
4	Quantifying the influence of sub-mesoscale dynamics on the supply of iron to Southern Ocean phytoplankton blooms	49
4.1	Introduction	50
4.2	Sub-mesoscale impact on Lagrangian paths	51
4.2.1	Lagrangian trajectories	51
4.2.2	Depth distribution of tracked particles	53
4.3	Methods	54
4.3.1	FeRRO _{SO}	55
4.3.2	Sensitivity to FeRRO _{SO} parameters	57
4.4	Results	58
4.4.1	Iron Concentration	59
4.4.2	Vertical fluxes of <i>DFe</i>	60
4.4.3	Primary production estimates	62
4.5	Discussion and Conclusions	63
5	Conclusions	67
5.1	Summary	67
5.2	Future directions	68
5.2.1	Towards more realistic simulations	68
5.2.2	Coupling of high-resolution models and observations	70
5.2.3	Improved parameterisation in global ocean models	70

List of Figures

1.1	Orthographic projection of the southern hemisphere. In colour is the absolute velocity, showing the energetic eddy field of the ACC (data from global MOM 1/10° resolution). Visible in grey are the main continents and black contours are the first 3000 m (600 m step) of the south Indian ocean main topographic features: the Kerguelen Plateau (KP) and the south east Indian Ridge (SEIR). ACC fronts are the blue contours and their locations are from Orsi et al. (1995): the Subantarctic Front (SAF), the Polar Front (PF) and the Southern ACC Front (SACCF). Meridians and parallels are drawn with a spacing of 20° (the first parallel is at 80°S).	2
1.2	Schematic representation of the Southern Ocean meridional circulation based on Marshall and Speer (2012). Wind directions are indicated by the circles, while cooling (warming) is shown by blue (red) arrows. Colours show density layers, while topography is in black. The circulation of the two cells is indicated by the black arrows.	3
1.3	Schematic of the biological pump in the ocean, that shows a simplified depiction of the major processes involved. Arrows indicate the direction of the relative processes and exchanges of carbon. Drawn are the sun, the ocean surface (blue contour), the euphotic layer (green line), the ocean floor, phytoplankton, zooplankton and aggregates.	4
1.4	Ocean colour image of a South Atlantic summer bloom, which forms an 8-shape (ESA Envisat image). The different blues and greens are due to different types and quantities of phytoplankton, while white represents clouds. The image has been captured from satellite with a resolution of 300 m.	5
1.5	Surface vorticity $\zeta(x, y)$ from a 1/80° model of the Kerguelen Plateau. Note that at these latitudes $f \sim 10^{-4} \text{ s}^{-1}$. Grey contours indicate the topography for the first 3000 m, with a step of 600 m.	6
1.6	Sub-mesoscale processes (adapted from Taylor and Ferrari (2011)).	8
1.7	Schematic of the circulation in the Kerguelen Plateau region from a 1/20° resolution model, adapted from Park et al. (2009). The topography for the first 3000 m is shaded in grey. Blue contours are temporal averages of the sea surface height (indicative contours with value, from the bottom: -0.8 m, -0.4 m and 0.5 m), while land contours are in white. Red arrows show the major pathways around the plateau, where the values of their relative cumulative transports are from Park et al. (2009).	9

1.8	Monthly climatology (December 2002-2012) of chlorophyll <i>a</i> concentration in the south Indian basin (data from Aqua MODIS 9km). Black lines are topographic contours of the first 3000 m, with a step of 600 m. The main topographic features visible are the Kerguelen Plateau, the south east Indian Ridge and Antarctica, at the bottom, where land is in white.	10
2.1	Monthly climatology (December 2002-2012) of chlorophyll <i>a</i> concentration in the south Indian basin (data are taken from Aqua MODIS 9 km and expressed as base 10 logarithms). Also shown are land surface (white), bathymetric contours with a contour interval of 600 m and the initial location of particles for the Lagrangian experiments (see section 2.2.3). The bathymetry data are taken from the 1-min SRTM bathymetry.	12
2.2	SOSE wind stress field overlying the 1-min SRTM zonally periodic bathymetry. The white contours represent the coastlines and the white box defines the domain of the $1/80^\circ$ model.	15
2.3	SOSE climatology surface field from 2005: (a) sea surface temperature and (b) fresh water fluxes (negative values represent fluxes into the ocean). The grey contour lines show topographic depths, with a contour interval of 600 m. The white colour represents land.	16
2.4	Northern boundary restoring salinity (in colour) and temperature (black lines, units are $^\circ\text{C}$) fields for KERG20.	17
2.5	Temporal mean of sea surface temperature (in colour) for (a) KERG20 and (b) KERG80. White contours represent contours of temporal mean of SSH, the black line shows the 3°C contour and the grey lines show the bathymetry levels for the first 3000 m, with a step of 600 m. The black arrows represent the surface mean flow.	19
2.6	Cumulative transport for the KERG20 experiment, following the path drawn on the picture. Numbers are transports in Sv and the dotted bars report transports from Park et al. (2009).	21
2.7	(a) 9-month average (05/2011 to 02/2012) of the eddy kinetic energy (resolution of $1/8^\circ$), computed from a regional high-resolution altimetry product around the Kerguelen Plateau (data from AVISO); the white box indicates the area in panels (b) and (c). The 200-day average of surface eddy kinetic energy for (b) KERG20 and (c) KERG80 (the colormap is saturated and peak values are $0.4 \text{ m}^2 \text{ s}^{-2}$). Contours are bathymetry levels with 600 m steps.	22
2.8	Time and zonal average of total kinetic energy spectra at 5 m depths, for KERG20 (blue) and KERG80 (magenta), computed in the KERG80 region. Plotted are also typical spectrum slopes: -3 (solid), -2 (dashed) and -5/3 (dotted).	23

-
- 2.9 Snapshots of the magnitude of surface horizontal velocity for (a) KER20 and (b) KER80. In black are shown the topography contours for the first 3000 m, with an interval of 600m. The instantaneous fields are taken at the same model day. 24
- 2.10 Frontal structures at approximately 50 m depth, for KER20 and KER80 cases. (a)-(b) $|\nabla_H \rho|$ (10^{-5}kg/m^4) and in black the topography contours for the first 3000 m, with an interval of 600 m. (c)-(d) $w(x, y)$ for the subdomains indicated by the white boxes in (a) and (b). In (c) and (d) contours represent $|\nabla_H \rho|$ with an interval of $1 \times 10^{-5} \text{kg/m}^4$ and the dashed black lines indicate the location of the vertical slices of $w(x, z)$ (e) and $w(y, z)$ (f). White lines in (e) and (f) indicate the mixed layer depths, while grey lines are isopycnals, with an interval of 0.1kg/m^3 . The instantaneous fields are taken at the same model day used in Fig. 2.9, for both resolutions. Note the different colour scales in (c)-(f). 25
- 2.11 Meridional profiles of vertical velocities near the surface (5 m depth, dashed black) and at 70 m (solid black), for the dotted line shown in Fig. 2.10 d. The magenta line shows the profile for $10^7 |\nabla_h \rho|$ near the surface. 26
- 2.12 Two-dimensional map of the 200-day temporal root mean square of w at roughly 50 m depth for (a) KER20 and (b) KER80. The numbers in (b) indicate three different regimes of vertical motion (see text) and the arrows the temporal mean circulation at 50 m depth. The scales for $w_{rms,2D}$ are different in the two cases. 27
- 2.13 Vertical profiles of rms of the vertical velocity: total component (magenta), mesoscale (black) and sub-mesoscale (blue). Dashed lines show the profiles for KER20, solid are for KER80. 27
- 2.14 Example of Lagrangian particle trajectories over 100 days in the backward experiment for $1/20^\circ$ (dashed lines) and $1/80^\circ$ (solid) resolutions. The particles have been selected for display reasons and in order to capture the main paths. Horizontal paths are shown in (a), where coastlines are in white and the bathymetry is shown by the greyscale. Temporal vertical excursions are plotted in the panel (b). 28
- 2.15 Log (base 10) of the particle counts at different depths with 50 m bins, in 6-hourly snapshots, over the 100-day integration and normalised by the total number of particles and snapshots. (a) Backward in time experiments (KER20 is dashed, KER80 is solid). (b) Forward experiments (including only particles released north of KP; colours refer to the depth of particle release; the dashed lines represent the KER20 runs, while KER80 results are shown by solid lines). 29

- 2.16 Lagrangian particle trajectories (over at most 100 days) in the forward experiment (north of KP) for (dashed lines) $1/20^\circ$ resolution and (solid) $1/80^\circ$, with particles released at 200 m depth. (a) shows horizontal paths, while vertical displacement of particles, as a function of longitude, is shown in panel (b). Shown in (a) are also \overline{SSH} contours (white) as in Fig. 2.5. The particles have been selected with a step of 0.65° for display reasons and in order to capture the main paths. Color mapped in panel (a) is the bathymetry. 30
- 2.17 Depths through which particles have passed (over at most the previous 100 days) before their last arrival in the range 10–150 m (arrival depths indicated by A). (a) The total number of particles reaching the arrival depths as a function of the release depths ($R_i = \{48, 102, 146, 202, 296, 396\}$ m) is plotted in the inset. Here, blue bars are for KERG20 and red for KERG80. The main part of the plot represents the % of those particles reaching A , grouped by each release depth, and passing through different source depths (S_n , $n = 1, 2, 3$) before reaching A . S_1 refers to source depths in the range (200–400) m (black), S_2 to (400–600) m (magenta) and S_3 to depths below 600 m (cyan). The pale-coloured bars are for KERG20, while solid bars are for KERG80. In panel (b) a schematic plot of arrival, source and release depths is shown. 31
- 2.18 Lagrangian tracking of particles for the third series of experiments (particles initialised south of Kerguelen Island). (a)-(b) are the horizontal paths overlying the temporal average of temperature at 50 m depth, while (c)-(d) show the vertical displacement. The test case with initial depth at 50 m is shown. Contours in panels (a) and (b) represent the bathymetry for the first 3000 m, with an interval of 600 m. 32
- 3.1 (a) The colours show a snapshot of surface density gradients $|\nabla_{H\rho}|$ over the entire $1/80^\circ$ domain, nested within the $1/20^\circ$ domain (the larger white area). Black contours are 200-day averages of sea surface height from the $1/20^\circ$ model (indicative values are, from the southernmost contour: -0.8 m, -0.4 m and 0.5 m), grey contours are isobaths for the first 3000 m, with 600 m steps, and land contours are in cyan. The red box in panel a defines the boundaries of the sub-region illustrated in panel b. 40
- 3.2 200-day temporal averages of (a) magnitude of sub-mesoscale vertical velocity at 400 m (colour scale is saturated), (b) surface sub-mesoscale eddy kinetic energy, (c) surface mesoscale strain rate, (d) surface mesoscale eddy kinetic energy and (e) bottom sub-mesoscale eddy kinetic energy. Boxes indicate sub-regions for the analysis shown in Fig. 3.3. Grey (black) contours in panel a (b-e) are topographic contours for the first 3000 m, with a step of 600 m (maximum depth is 5000 m). The black contour in panel a is the 400 m isobath. 41

-
- 3.3 Vertical profiles of 200-day average of spatial root mean square mesoscale (magenta) and sub-mesoscale (black) vertical velocity for the boxes in Fig. 3.2 (x-axis indicates values in $[\text{m d}^{-1}]$); histograms show the probability density function of topographic depth. 43
- 3.4 (a,b) Snapshot vertical sections at approximately 51°S (in KP_3 region) and (c,d) at 88°E (in KP_4). Panels a and c show mesoscale components of vertical velocity, while b and d show the sub-mesoscale components. The black lines represent the mixed layer depth, computed with a temperature criterion of $\Delta T = 0.05^\circ\text{C}$ 44
- 3.5 Vertical velocity dependence on mesoscale (a) surface eddy kinetic energy and (b) surface strain rate. Fields are 200-day and $2^\circ \times 2^\circ$ averages (vertical velocity is also averaged over the top 400 m) and the standard deviation computed for each box (216 boxes in total) is illustrated by the vertical bars. 47
- 4.1 Kerguelen Plateau bathymetry. In green the area *ON* the plateau (defined by the 500 m isobath); in red is the transition zone, between the *ON* and *OFF* plateau area (grey shading, delimited by the 1500 m isobaths). The black and blue boxes delineate the particle release locations. 52
- 4.2 Examples of Lagrangian trajectories, daily sampled, color-coded depending on the daily depth, for the $1/80^\circ$ resolution experiment. Circular markers indicate the particle release location, while triangular the source position. Topography is shaded in grey. Green contours indicate the boundaries of the *ON* source, while red the *OFF* plateau source. 53
- 4.3 Probability density function of particle depth for the two regions of investigation, R_1 and R_2 . Colors indicate the different resolution (red is for the $1/20^\circ$ and black is for the $1/80^\circ$). Dashed lines are the profiles for the *ON* particles, dotted for the *OFF* and solid for the total amount of particles (*TOT*). 54
- 4.4 (a) Vertical profiles of (blue) decay rate $\lambda(z_i)$ from equation (4.2) and (green) structure function $f(z_i)$ for the relaxation term (4.3). (b) Vertical profiles of $\langle DFe \rangle_i$ as computed by solving (4.4), for the *ON* (green line) and *OFF* (black) the plateau areas, and in the transition zone (red) (for clarity, only the first 500 m are shown). 56
- 4.5 Sensitivity of dissolved iron concentration (a, b) and vertical iron fluxes (c, d) to decay rate (a, c) and relaxing timescale (b, d) for the particles in region R_1 (black lines) and R_2 (blue). Shown are results for the $1/80^\circ$ resolution experiment. The ordinate axis indicates the difference from the reference case, expressed as a percentage. 59

-
- 4.6 (a) Average dissolved iron concentration (particles released at both 75 m and 200 m are considered), (b) vertical fluxes of dissolved iron at 200 m and (c) export production estimated from the fluxes at 75 m for the two regions of analysis (R_1 and R_2). Red (black) bars show the results for the $1/20^\circ$ ($1/80^\circ$) resolution model. The contribution due to the *ON*, *OFF*, as a proportion of the total number of particles, are indicated by the different shading. The blue dashed line in panel a indicates the $[DFe]$ over the plateau as observed by Blain et al. (2007). In panel b, the horizontal dashed lines identify estimates by Bowie et al. (2014): vertical flux due to upwelling (blue), total vertical flux due to the sum of diffusion, upwelling and entrainment (black) and lateral advective iron supply (magenta). Blue line in panel c is the observed net primary production observed in region R_1 by Bowie et al. (2014). 60

List of Tables

2.1	Parameters used in the model.	18
4.1	Dissolved iron concentration, vertical iron fluxes and estimated production for the two regions of analysis, due to <i>TOT</i> , <i>ON</i> and <i>OFF</i> particles, and at the two resolutions. The export production estimates (EP) are computed from a DFe/C ratio of $0.021 \text{ mmol Fe mol}^{-1} C$ (from Bowie et al., 2014), and then converted into total production using an fe ratio of 0.49 (from Sarthou et al., 2008).	61

Preamble

The main body of the thesis (Chapters 2 to 4) is composed by either accepted or submitted for publication papers in a scientific journal. The thesis author was the primary researcher and author of each paper. Coauthors supervised and guided the research and were involved in editing the manuscript. The above-mentioned articles are:

Chapter 2 Rosso I., Hogg A. McC., Strutton P. G., Kiss A. E., Matear R., Klocker A. and van Sebille E. (2014) Vertical transport in the ocean due to sub-mesoscale structures: Impacts in the Kerguelen region. *Ocean Modell.*, 80, 10–23

Chapter 3 Rosso I., Hogg A. McC., Kiss A. E. and Gayen B. (2015) Topographic influence on sub-mesoscale dynamics in the Southern Ocean. *Geophys. Res. Lett.*, 42, doi:10.1002/2014GL062720.

Chapter 4 Rosso I., Hogg A. McC., Matear R. and Strutton P. G. Quantifying the influence of sub-mesoscale dynamics on the supply of iron to Southern Ocean phytoplankton blooms. Submitted to *Deep Sea Res., Part I*.

Introduction

1.1 The Southern Ocean circulation

The Southern Ocean includes the band of latitudes south of $\sim 30^\circ\text{S}$ (Fig. 1.1). The westerly winds, blowing between 40°S – 60°S , drive an equatorward Ekman transport of surface waters, and the wind stress curl causes upwelling south of $\sim 50^\circ\text{S}$ and downwelling north of the wind maximum (Fig. 1.2) (Marshall and Speer, 2012). Easterly winds, which blow close to Antarctica, drive an Ekman transport toward the Antarctic continent and a consequent downwelling of waters (Talley et al., 2011).

The circulation in the Southern Ocean is exceptionally complex and is considered central in the role of the ocean in the global climate system. Specifically, its circulation is dominated by the predominantly eastward and deep-reaching Antarctic Circumpolar Current (ACC), the largest ocean current, whose volume transport reaches about 135 Sv ($1 \text{ Sv} = 10^6 \text{ m}^3 \text{ s}^{-1}$) at the Drake Passage (the gap between south America and Antarctica) (Cunningham et al., 2003). Driven by a combination of westerly winds and surface buoyancy fluxes, the ACC is one of the strongest ocean currents on Earth, with speeds reaching up to $\sim 1 \text{ m s}^{-1}$. Uninterrupted by any land masses, the ACC flows around Antarctica, acting as the principal conduit between the Pacific, Atlantic and Indian basins, and redistributing heat and mixing water properties amongst the three oceans.

The ACC is not purely zonal and its dynamics depend upon a complex interplay between wind, eddy and buoyancy fluxes. In particular, the ACC is characterised by jets and fronts (shown in Fig. 1.1 and studied by e.g. Orsi et al., 1995; Sokolov and Rintoul, 2009a) and by a rich field of mesoscale eddies. The narrow currents within the fronts are strong and predominantly eastward, while waters between the fronts are dominated by eddies. Talley et al. (2011) identified three major fronts as part of the ACC (Fig. 1.1): the Subtropical Front (considered as the northern limit of the ACC), the Polar Front and the Southern ACC Front (the ACC southern limit).

The complexity of the ACC is enhanced by its interaction with topography, which, due to the weak stratification of the Southern Ocean compared to lower latitudes and its equivalent barotropic nature (Ward and Hogg, 2011), can directly affect the surface flow. In particular, the circulation is steered by the topography, such that its structure is deeply constrained and modified: jets and fronts, for instance, can deviate from the zonal direction, in space (e.g. Sokolov and Rintoul, 2009b) and time (Chapman and Morrow,

2014). Furthermore, downstream from topographic features quasi-stationary meanders (Naveira-Garabato et al., 2009) or Rossby waves (e.g. Colton and Chase, 1983) can be generated by the interaction with the topography. Topography can excite hotspots of eddy kinetic energy (Thompson and Sallée, 2012), generate energetic internal tides (e.g. Park et al., 2008a) and enhance vertical mixing (e.g. Nikurashin et al., 2013).

Through the Meridional Overturning Circulation (MOC, Fig. 1.2), the Southern Ocean serves as connection between surface and deep waters. The MOC is comprised of two overturning cells: an upper cell, which is associated with northward Ekman transport of dense upwelled water (e.g. formed in the North Atlantic; Toggweiler and Samuels, 1995), becoming fresher and warmer and eventually sinking again forming the Intermediate and Mode waters; and a lower cell in which upwelled water moves southward. In a few

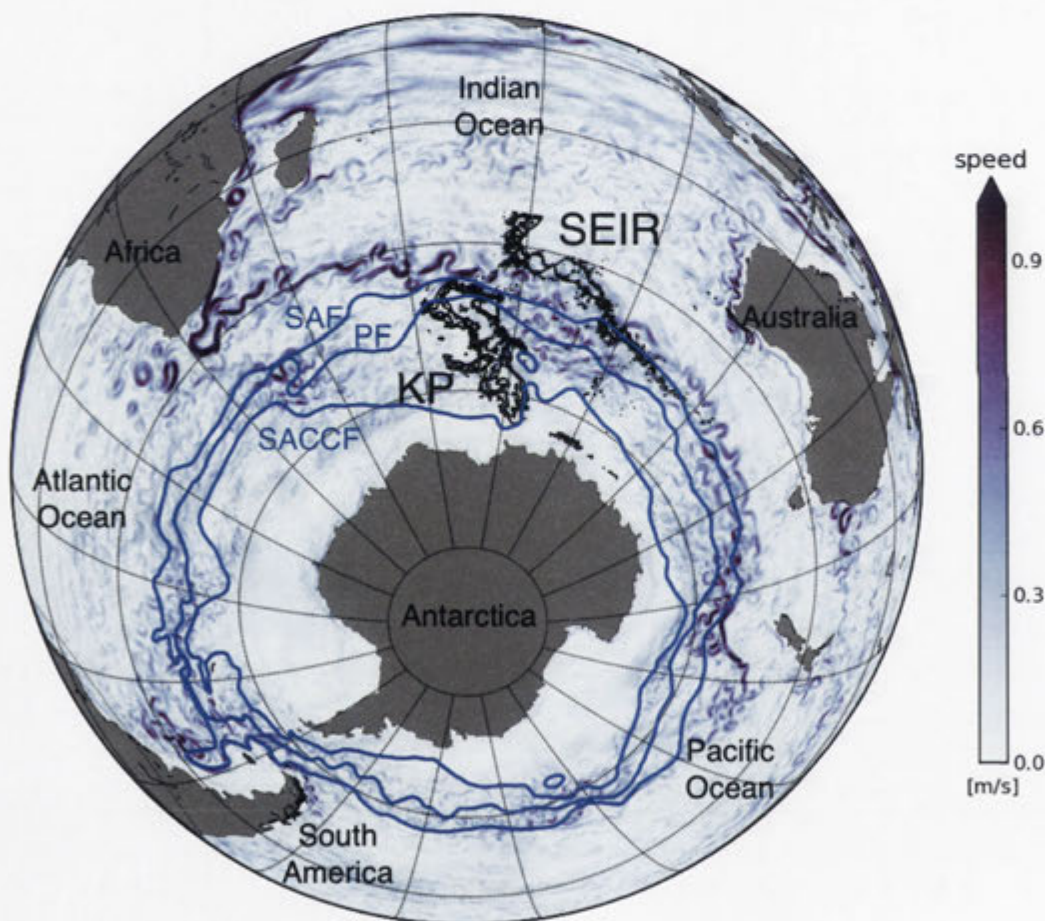


Figure 1.1: Orthographic projection of the southern hemisphere. In colour is the absolute velocity, showing the energetic eddy field of the ACC (data from global MOM 1/10° resolution). Visible in grey are the main continents and black contours are the first 3000 m (600 m step) of the south Indian ocean main topographic features: the Kerguelen Plateau (KP) and the south east Indian Ridge (SEIR). ACC fronts are the blue contours and their locations are from Orsi et al. (1995): the Subantarctic Front (SAF), the Polar Front (PF) and the Southern ACC Front (SACCF). Meridians and parallels are drawn with a spacing of 20° (the first parallel is at 80°S).

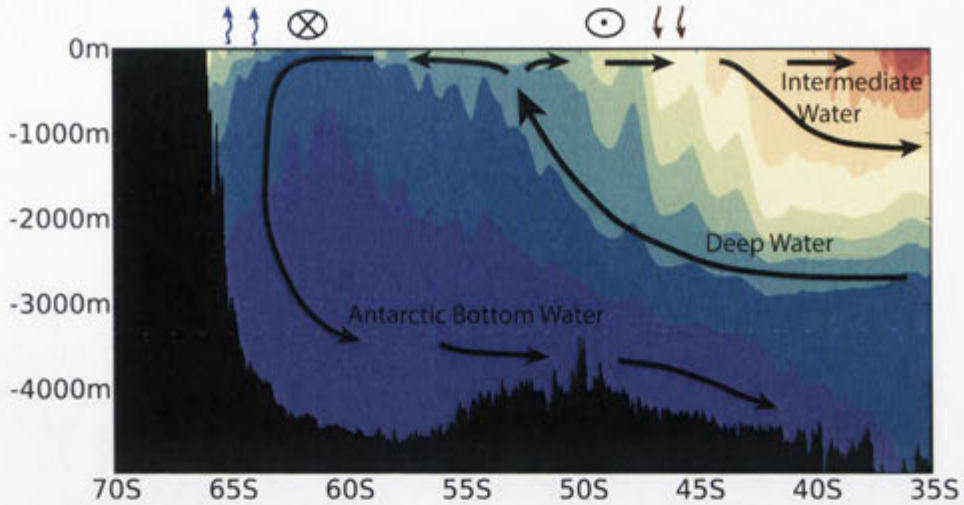


Figure 1.2: Schematic representation of the Southern Ocean meridional circulation based on Marshall and Speer (2012). Wind directions are indicated by the circles, while cooling (warming) is shown by blue (red) arrows. Colours show density layers, while topography is in black. The circulation of the two cells is indicated by the black arrows.

localised regions around Antarctica, such as the Weddell Sea, the Ross Sea and the Mertz Polynya (e.g. Marshall and Speer, 2012; Talley, 2013), water density increases leading to the formation of the world's densest water mass, the Antarctic Bottom Water, which eventually sinks to the abyssal ocean.

The role of the ACC in the mixing of waters between the different basins is just one expression of the central role of the Southern Ocean in the climate system. In fact, the MOC has profound implications for the storage and deep redistribution of heat, carbon, oxygen and other gases in the Southern Ocean, thereby impacting the climate system. In particular, the sinking of waters drive these tracers (absorbed from the atmosphere) into the ocean interior, while at the outcrop of waters they are released into the atmosphere. Viewed from this perspective the connection provided by the Southern Ocean between the different basins controls the transport and distribution of such properties. Given the substantial impact of the Southern Ocean in exporting anthropogenic carbon (over 40% of the global export has been due to the Southern Ocean in 2008; Khatiwala et al., 2009), it is fundamental to understanding the dynamics governing the carbon cycle in this part of the globe.

1.2 Biological activity in the Southern Ocean

The carbon cycle in the ocean is the product of several processes, such as solubility and biological pumps (which act to remove carbon dioxide from the atmosphere), as well as physical mechanisms. In order to better understand the Southern Ocean's primary role in influencing the carbon cycle, precise quantification of the processes that control carbon

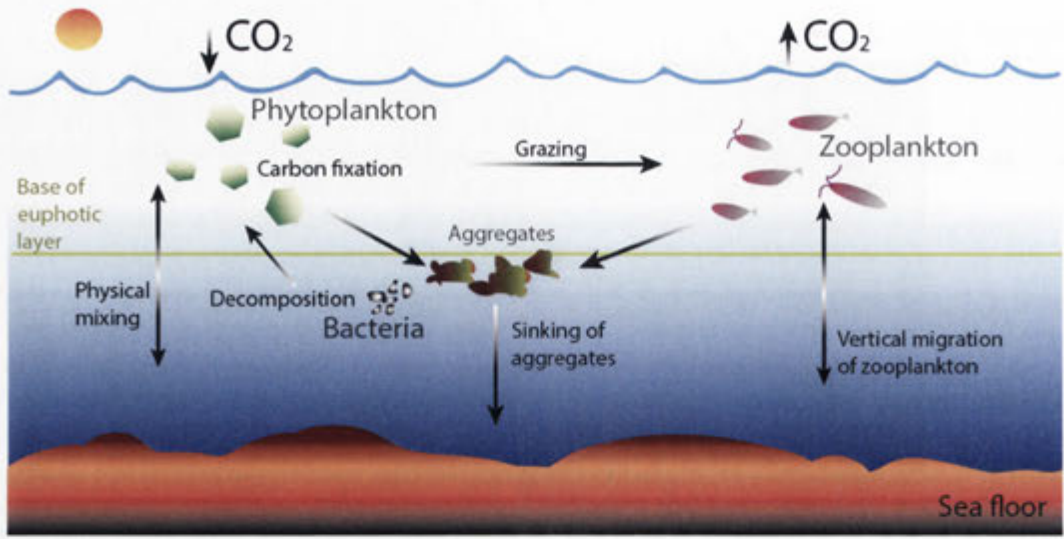


Figure 1.3: Schematic of the biological pump in the ocean, that shows a simplified depiction of the major processes involved. Arrows indicate the direction of the relative processes and exchanges of carbon. Drawn are the sun, the ocean surface (blue contour), the euphotic layer (green line), the ocean floor, phytoplankton, zooplankton and aggregates.

uptake in this region is critical for understanding and predicting our future climate.

Physical mechanisms acting between the surface and the deep ocean are responsible for the transfer of carbon between the atmosphere and the ocean, in what is called the solubility pump (e.g. Carlson et al., 2001). The solubility of carbon dioxide in the sea water increases at higher latitudes, due to the cold temperatures of the ocean surface, consequently generating a flux of carbon into the ocean. For example, at the locations of AABW formation, carbon dioxide is absorbed through the surface and then pumped down to the depths by the downwelling circulation, becoming part of the global ocean circulation which will store the carbon for hundreds of years. Eventually, the carbon will be transported to lower latitudes and, upwelled to the ocean surface, it will flux back to the atmosphere.

The biological pump is a complex system of mechanisms (e.g. Ducklow et al., 2001), that in its very simple form can be understood in three separate phases (Fig. 1.3). The first stage of the biological pump is the production of fixed carbon due to phytoplankton in the euphotic layer, or the amount of new organic matter produced by the photosynthesis. In the photosynthetic process, phytoplankton absorb carbon dioxide and nutrients to produce organic compounds. The amount of production depends on the particular species of phytoplankton and the availability of light and nutrients. Zooplankton, which migrate in the water column on a diurnal cycle, graze on the phytoplankton. Zooplankton excretion or dead phytoplankton and zooplankton form aggregates: part of these aggregates is consumed by bacteria and part is mixed or sink to the ocean floor, transporting carbon to the depths (second stage). In the final phase, aggregates are decomposed by bacteria, and carbon and other nutrients are remineralised. The ocean depth is thereby rich in nutrients

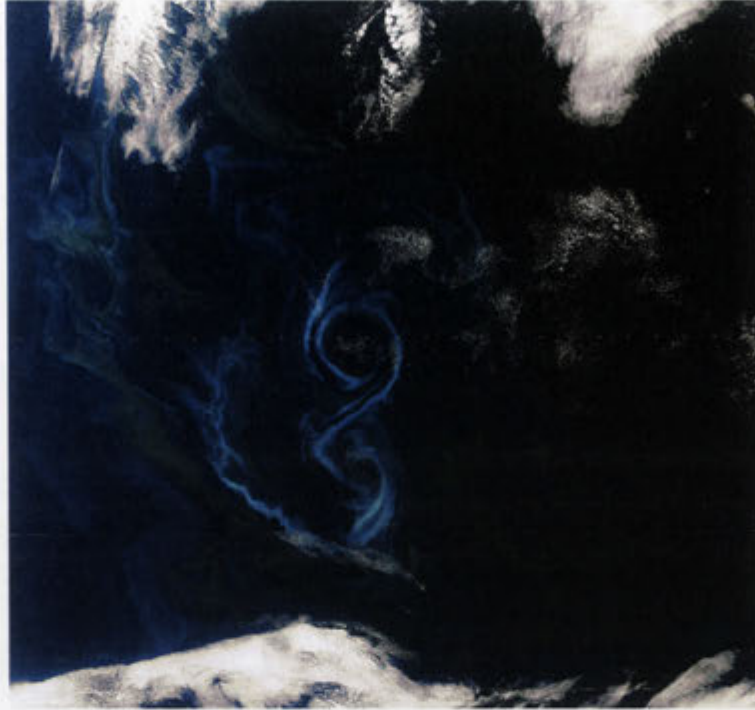


Figure 1.4: Ocean colour image of a South Atlantic summer bloom, which forms an 8-shape (ESA Envisat image). The different blues and greens are due to different types and quantities of phytoplankton, while white represents clouds. The image has been captured from satellite with a resolution of 300 m.

and physical mechanisms are necessary to make them available again to phytoplankton in the euphotic layer.

The Southern Ocean is a “high nutrient, low chlorophyll” environment, meaning that, despite the large availability of nutrients (e.g. nitrate), the productivity is very low. The summer phytoplankton growth in the Southern Ocean is mainly limited by the availability of iron (e.g. Martin, 1990; Boyd et al., 2000; Coale et al., 2004; de Baar et al., 2005). However, it is known that in the Southern Ocean there exist areas of large phytoplankton activity, such as in the Weddell and Scotia Seas (e.g de Baar et al., 1990) or in correlation to large topographic features, such as around the Crozet Islands (e.g. Planquette et al., 2007) or the Kerguelen Plateau (e.g. Chever et al., 2010; Bowie et al., 2014). Understanding the potential iron sources, for the surface waters in these biological hotspot, is of fundamental importance.

From satellite observations, it is possible to estimate the distribution of chlorophyll a (the key light-absorbing pigment contained in phytoplankton), phytoplankton or nutrients, revealing particular features associated with eddies and filamentary structures at scales far smaller than mesoscale eddies, known as sub-mesoscales. Figure 1.4 shows an example of a phytoplankton bloom in the South Atlantic, where structures at different scales can be noticed. Mesoscale eddies are important for nutrient fluxes into the sunlit layers, from the nutrient rich deep waters in the open ocean, thereby stimulating phytoplankton blooms

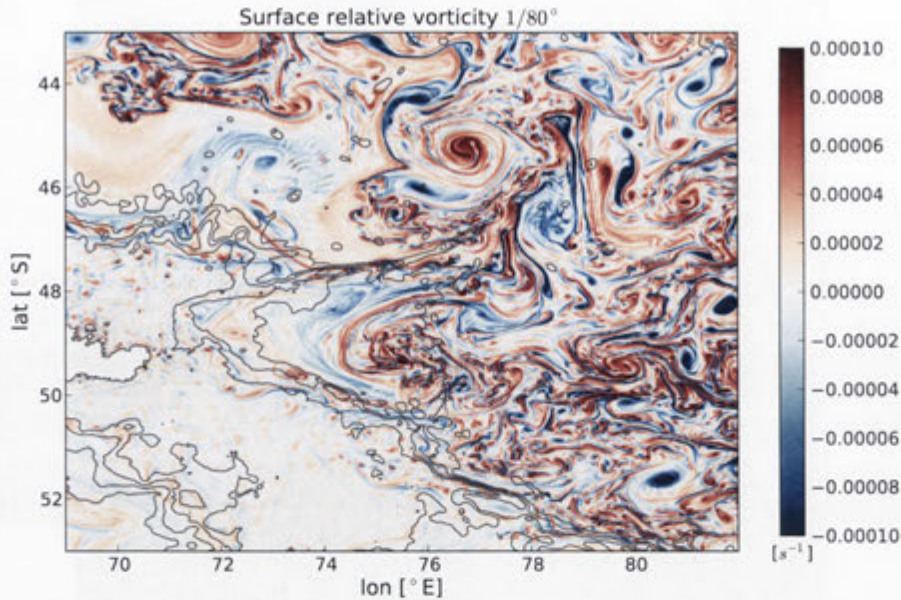


Figure 1.5: Surface vorticity $\zeta(x, y)$ from a $1/80^\circ$ model of the Kerguelen Plateau. Note that at these latitudes $f \sim 10^{-4} \text{ s}^{-1}$. Grey contours indicate the topography for the first 3000 m, with a step of 600 m.

(e.g. McGillicuddy Jr and Robinson, 1997; McGillicuddy et al., 2007). On the other hand, numerical simulations have recently highlighted the tremendous impact that sub-mesoscale flows can have over the productivity in the ocean (e.g. Lévy et al., 2001; Martin et al., 2002).

How these structures alter the biological activity in different parts of the ocean is still unclear, certainly their importance in Southern Ocean's waters is unknown. At the present time there are no existing studies of the role of sub-mesoscales on Southern Oceans dynamics and the impacts that these small-scale flows can have on phytoplankton blooms at these latitudes.

1.3 Sub-mesoscale dynamics

High-resolution numerical models and satellite observations revealed an intricate and ubiquitous web of sub-mesoscale density fronts, which are characterised by horizontal scales of the order of 10 km, a vertical extension of few hundred meters and a lifetime of the order of several days. Their dynamics differs from that of the mesoscale as their Rossby number ($R_o = |\zeta_z/f|$, where $\zeta_z = v_x - u_y$ is the vertical vorticity, f the planetary vorticity, u and v the zonal and meridional velocities, respectively, and the subscripts indicate the derivative) and Richardson number ($R_i = N^2/|\partial_z \vec{u}_h|^2$, where \vec{u}_h is the horizontal velocity and $N^2 = \partial_z b$ the square of the buoyancy frequency $b = -g\rho/\rho_0$, with density ρ , reference density ρ_0 and acceleration due to gravity g) are order of 1. The magnitude of the Rossby number indicates that ζ_z is of order of f (Fig. 1.5).

Due to the fine scale of these structures, their processes are difficult to observe and often require parameterisation in large-scale numerical models (Fox-Kemper et al., 2008). However, in smaller domains their dynamics can be investigated (e.g. McWilliams et al., 2001; Lévy et al., 2001; Mahadevan and Tandon, 2006; Capet et al., 2008a; Molemaker et al., 2005). Sub-mesoscale dynamics are linked to Ertel’s potential vorticity ($q = (f + \zeta_z)N^2 + \omega_h \cdot \nabla_h b$, where $\omega_h = (w_y - v_z, u_z - w_x)$ is the horizontal vorticity and w is the vertical velocity), where processes at these scales tend to lower the magnitude of q (e.g. Thomas et al., 2008; Capet et al., 2008a). Their dynamics can be considered hydrostatic, as numerical simulations of Haine and Williams (2002) and Mahadevan (2006) showed, and they offer a route to dissipation via loss of balance of geostrophic flows (e.g. McWilliams et al., 2001; Molemaker et al., 2005). Several authors have highlighted the influence that sub-mesoscales have on the mixed-layer stratification (Lapeyre et al., 2006; Boccaletti et al., 2007; Fox-Kemper et al., 2008; Thomas and Ferrari, 2008; Mahadevan et al., 2010) and on large-scale flows (Lévy et al., 2010).

Different mechanisms can give rise to such small-scale features in the presence of sharp horizontal gradients, which include frontogenesis and frontal instabilities (e.g. Hoskins and Bretherton, 1972; Boccaletti et al., 2007; Mahadevan and Tandon, 2006; Capet et al., 2008a; Thomas and Ferrari, 2008; Thomas et al., 2008). Frontogenesis arises in regions of front intensification, due to the stirring of large-scale or mesoscale flows acting on geostrophically balanced density fronts. Regions of large strain are associated with large values of ζ_z and R_ρ . Consequently, large ζ_z generates a loss of geostrophic balance, giving rise to an ageostrophic overturning motion (or ageostrophic secondary circulation ASC), with the effect of restoring the geostrophic balance (Fig. 1.6). The ASC generates large vertical velocities at the edges of density fronts (up to one order of magnitude larger than mesoscale vertical velocities), upwelling waters on the light side and downwelling on the dense side (e.g. Capet et al., 2008a). The development of sub-mesoscales and the consequent large w at ocean fronts can also be due to spontaneous ageostrophic baroclinic instabilities (or mixed layer instabilities as Molemaker et al., 2005, defined them), which draw their energy from the available potential energy stored in the horizontal density gradients (Fox-Kemper et al., 2008). Forced instabilities, such as those due to the destabilising action of down-front winds or heat and salt fluxes, can also lead to the intensification of ocean fronts, the generation of large vertical velocity and strong ASC.

Numerical studies have not only revealed that sub-mesoscales control vertical velocities, but that they also play a significant role in the vertical transport of tracers (e.g. Lévy et al., 2001, 2012). The enhancement of vertical transport can influence the carbon cycle by intensifying nutrient supply to the surface euphotic layers and consequently stimulating phytoplankton production (e.g. Lévy et al., 2001; Klein and Lapeyre, 2009). Lévy et al. (2001) found that sub-mesoscales can provide nutrients in a more efficient way than mesoscales, leading to an increment of the primary production by a factor of 2, compared to large-scale-induced production.

High-resolution numerical models have usually investigated sub-mesoscale dynamics

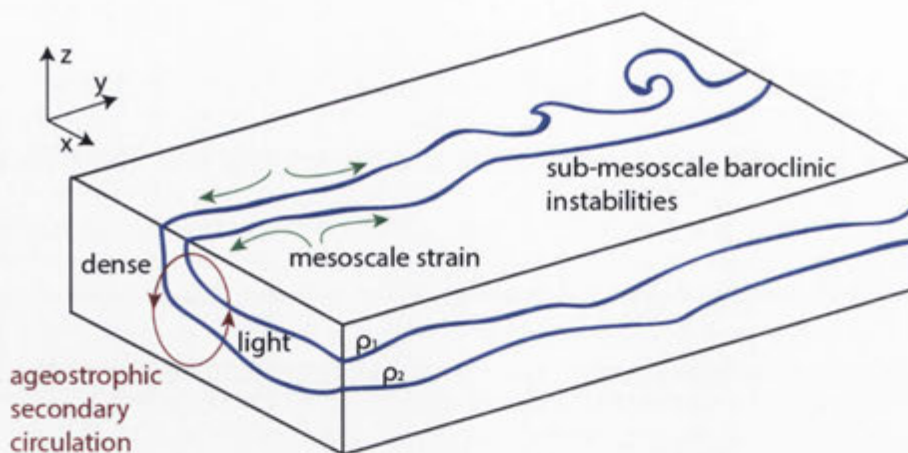


Figure 1.6: Sub-mesoscale processes (adapted from Taylor and Ferrari (2011)).

employing flat-bottom topography (e.g. Lévy et al., 2001; Capet et al., 2008a; Mahadevan, 2006; Mahadevan and Tandon, 2006; Lévy et al., 2012); however, topography may influence the upper-ocean sub-mesoscale dynamics particularly in the Southern Ocean, as regions of high productivity are found associated with large subsurface topography.

This thesis is focused on the role that sub-mesoscales have on the transport of nutrients, and in particular in the investigation of sub-mesoscale processes as a possible route for the supply of iron to the surface. As a case study, the focus is on the iron-limited region of the Kerguelen Plateau (Fig. 1.1).

1.4 The Kerguelen Plateau

The Kerguelen Plateau (KP) is a prominent topographic feature in the south Indian Ocean basin (Fig. 1.1). Its large and shallow topography constitutes a physical barrier to the ACC and drives a complex local circulation (Fig. 1.7). KP constrains the ACC and the location of its major fronts. Most of the ACC transport is pushed to flow north of the plateau (89–94 Sv; Park et al. (2009)), while a large fraction (43 Sv) passes through the Fawn Trough, a sill located at $\sim 56^\circ\text{S}$ which divides the plateau into Northern and Southern Kerguelen plateaus. Over the Northern plateau (KP, between Kerguelen and Heard Islands), the remaining fraction of the ACC flows. Finally, a strong and deep western boundary current circulates northward, along the eastern flank of the plateau (Park et al., 2008b, 2009). KP sets also the position of the Circumpolar fronts: Park et al. (2009) located the Subantarctic Front north of the plateau, the Polar Front south of the Kerguelen Island and the Southern ACC Front through the Fawn Trough (Fig. 1.7).

A summertime phytoplankton bloom is triggered in the northern KP region by natural iron fertilisation (Fig. 1.8). Numerous studies have highlighted the intrinsic relation between physical processes and biological responses and have identified physical mechanisms as main drivers for iron into the upper ocean waters of KP. Different sources have been identified, such as atmospheric dust deposition (e.g. Bucciarelli et al., 2001; Chever et al.,

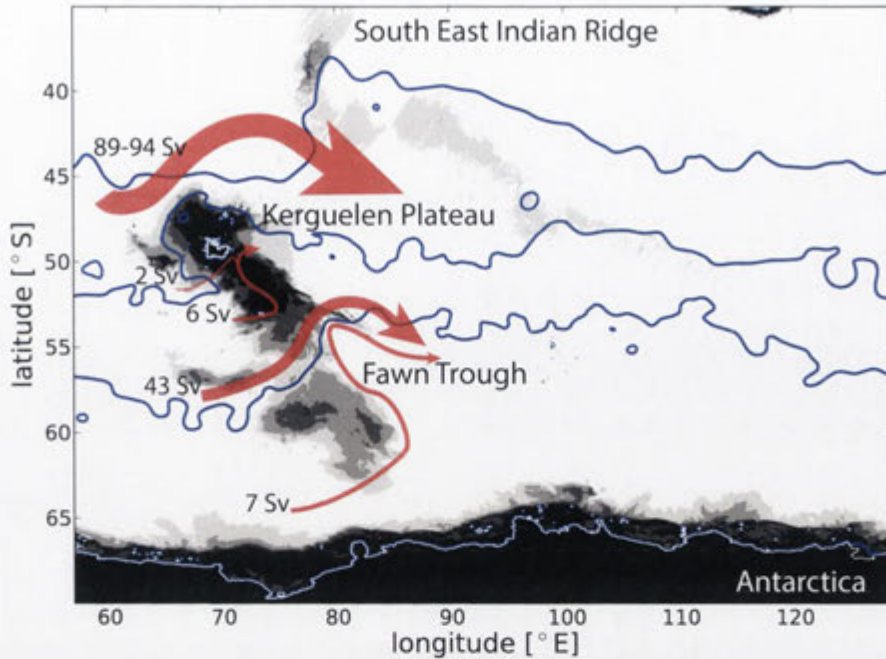


Figure 1.7: Schematic of the circulation in the Kerguelen Plateau region from a $1/20^\circ$ resolution model, adapted from Park et al. (2009). The topography for the first 3000 m is shaded in grey. Blue contours are temporal averages of the sea surface height (indicative contours with value, from the bottom: -0.8 m, -0.4 m and 0.5 m), while land contours are in white. Red arrows show the major pathways around the plateau, where the values of their relative cumulative transports are from Park et al. (2009).

2010), sediment input from the shelf of the plateau and the islands (e.g. Bown et al., 2012) or deep iron-rich waters above the plateau (e.g. Blain et al., 2008). Physical mechanisms that can control the iron delivery from the shelf and deep waters are well documented (e.g. Mongin et al., 2008; Park et al., 2008a,b; Maraldi et al., 2009; Mongin et al., 2009; van Beek et al., 2008; d'Ovidio et al., 2013; Gille et al., 2014) and include turbulent mixing due to tides and internal waves (Park et al., 2008a), eddy stirring (Abraham et al., 2000; d'Ovidio et al., 2013), lateral advection (van Beek et al., 2008; Mongin et al., 2009) and mixing (Maraldi et al., 2009), and wind-induced upwelling (Gille et al., 2014).

The impact that sub-mesoscale dynamics might have on the supply of iron to surface KP waters has never been taken into account. Observations of sub-mesoscale phenomena are difficult, due to both their temporal and spatial scales; and sub-mesoscale-resolving numerical models are computationally very expensive. However, due to the already assessed ecosystem response to sub-mesoscale processes over other parts of the ocean, it is natural to interrogate what their footprint would be in this area of the Southern Ocean.

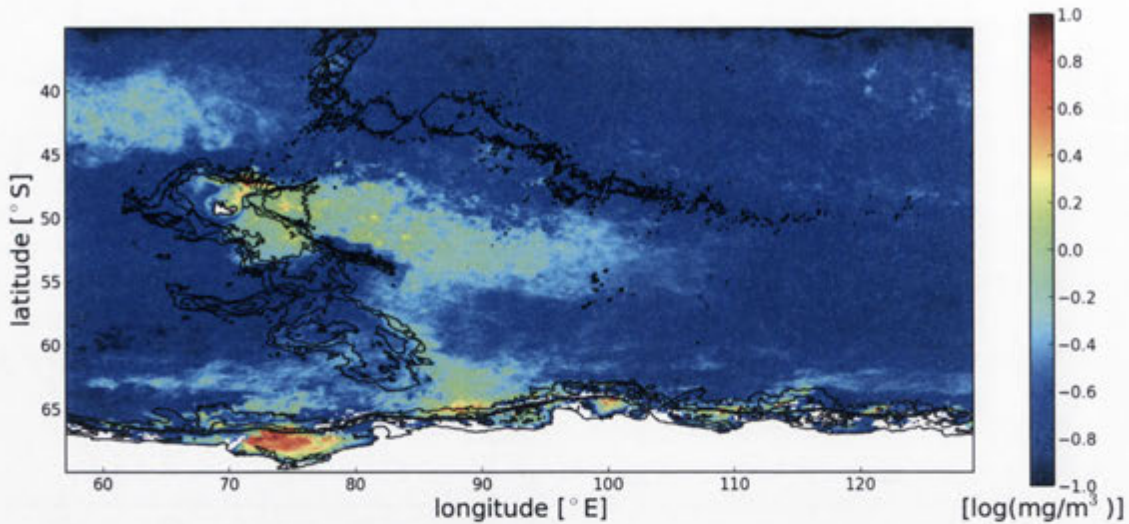


Figure 1.8: Monthly climatology (December 2002-2012) of chlorophyll a concentration in the south Indian basin (data from Aqua MODIS 9km). Black lines are topographic contours of the first 3000 m, with a step of 600 m. The main topographic features visible are the Kerguelen Plateau, the south east Indian Ridge and Antarctica, at the bottom, where land is in white.

1.5 Research orientation

This thesis aims to investigate the sub-mesoscale dynamics in the Kerguelen Plateau region and how the topography might influence them, through the development and analysis of the first sub-mesoscale-resolving numerical model of the ocean circulation in this area. The focus of this research is the contribution of sub-mesoscales to the vertical transport and the quantification of the impact that these dynamics can have over KP productivity.

First, Chapter 2 (Rosso et al., 2014) investigates the sensitivity of vertical velocities to the horizontal resolution, by comparing a mesoscale- ($1/20^\circ$ resolution) with a sub-mesoscale-resolving model ($1/80^\circ$) of the Kerguelen Plateau region. In addition, a Lagrangian particle-tracking tool is used to quantify the vertical transport due to mesoscale and sub-mesoscale dynamics.

In Chapter 3 (Rosso et al., 2015) the topographic influence on the sub-mesoscale field that develops in the Kerguelen Plateau region and further downstream is examined. Different causes for the upper ocean inhomogeneity in the sub-mesoscale fields are considered and their features analysed.

A new methodology for the investigation and the understanding of iron supply in relation to physical structures is the focus of Chapter 4 (Rosso et al., Submitted 2015). The phytoplankton productivity is here inferred from an iron/carbon ratio and results from the mesoscale-resolving-model are contrasted to the $1/80^\circ$ resolution model.

Finally, the conclusions of the thesis are given in Chapter 5. Here, possible future developments are also presented.

Vertical transport in the ocean due to sub-mesoscale structures: Impacts in the Kerguelen region

Abstract

The summertime phytoplankton bloom near the Kerguelen Plateau is in marked contrast to the low-chlorophyll conditions typical of the Southern Ocean and is thought to arise from natural iron fertilisation. The mechanisms of iron supply to the euphotic zone in this region are poorly understood, and numerical studies of iron transport have until now omitted fine-scale (sub-mesoscale) dynamics which have been shown to significantly increase vertical transport in other parts of the ocean.

We present the first sub-mesoscale-resolving study of the flow and vertical transport in this region. The modelled transport and flow structure agree well with observations. We find that an increase in horizontal resolution from mesoscale-resolving ($1/20^\circ$) to $1/80^\circ$ resolves sub-mesoscale filamentary frontal structures in which vertical velocities are dramatically higher and are consistent with available observations. Lagrangian tracking shows that water is advected to the surface from much greater depth in the sub-mesoscale-resolving experiment, and that vertical exchange is far more rapid and frequent. This study of sub-mesoscale vertical velocities sets the foundation for subsequent investigation of iron transport in this environment.

2.1 Introduction

The Southern Ocean is a prominent example of a high-nutrient low-chlorophyll (HNLC) environment, with summer phytoplankton productivity mainly limited by the availability of iron (Boyd et al., 2000). Phytoplankton blooms are an important component of the earth system, primarily via contributions to the oceanic carbon cycle. In the Southern Ocean, anthropogenic carbon uptake is very high (e.g. Sabine et al., 2004; Khatiwala et al., 2009), yet a complete understanding of the mechanisms controlling air-sea CO_2 fluxes in

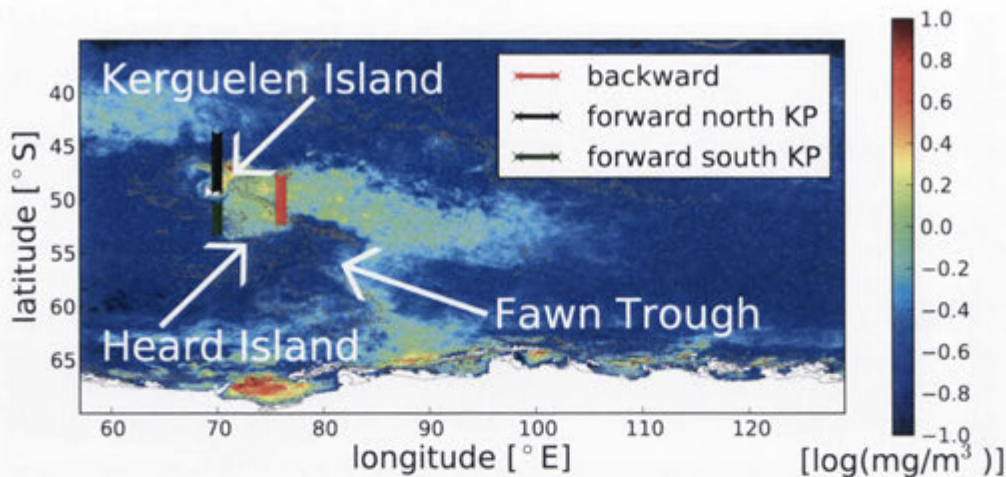


Figure 2.1: Monthly climatology (December 2002-2012) of chlorophyll *a* concentration in the south Indian basin (data are taken from Aqua MODIS 9 km and expressed as base 10 logarithms). Also shown are land surface (white), bathymetric contours with a contour interval of 600 m and the initial location of particles for the Lagrangian experiments (see section 2.2.3). The bathymetry data are taken from the 1-min SRTM bathymetry.

this environment, and their sensitivity to potential changes in biological productivity, is lacking. Despite the HNLC conditions of the Southern Ocean, elevated chlorophyll concentrations occur in several locations of the Southern Ocean, including the seasonal blooms originating on and downstream of the Kerguelen Plateau (Fig. 2.1). The Kerguelen Plateau (KP) is a significant feature in the south Indian Ocean basin, with a topography that drives a complex local circulation (Park et al., 2008b). In this region, the Antarctic Circumpolar Current (ACC) is constrained by the shallow bathymetry of the plateau and divided into different streams: strong currents occur north of the Kerguelen Islands and through the Fawn Trough (located at 56°S), with a weak flow over the shallow plateau between Kerguelen and Heard Islands.

In particular, while the importance of the Kerguelen bloom has been well documented (Abraham et al., 2000; Blain et al., 2007; Mongin et al., 2008; Park et al., 2008a,b; Maraldi et al., 2009; Mongin et al., 2009), the mechanisms that drive vertical iron fluxes to the euphotic zone, and consequently trigger the bloom, are unclear. Possible mechanisms include lateral (e.g. Mongin et al., 2009; Maraldi et al., 2009; Park et al., 2008b) and vertical processes (e.g. Park et al., 2008a; van Beek et al., 2008). These studies have highlighted the intrinsic relation between physical processes and biological responses. Yet, an exhaustive analysis of transport mechanisms in this area is lacking. In particular, a numerical model able to fully represent the dynamics in this area has not yet been developed.

The present study investigates the transport of tracers by small-scale processes, which may control local circulation and be important for the iron supply to the KP region. We build on a series of recent studies which have found that sub-mesoscale structures of scale

$O(10\text{ km})$ may generate a strong vertical transport, upwelling nutrient rich waters from the base of the mixed layer and downwelling depleted waters from the surface (Martin et al., 2002; Mahadevan, 2006; Capet et al., 2008a; Klein and Lapeyre, 2009; Lévy et al., 2001, 2012). The sub-mesoscales arise from the interaction between larger scale structures and are mainly related to frontogenetic processes (Capet et al., 2008b; Ferrari and Wunsch, 2009). High values of simulated surface $p\text{CO}_2$, vertical velocity and vorticity are found close to sub-mesoscale fronts (e.g. Resplandy et al., 2009; Lévy et al., 2001), which act as preferential paths for the exchange of gases between the atmosphere and ocean interior. Frontal instabilities can explain this enhancement by driving an ageostrophic secondary circulation (ASC) occurring in the cross-front plane, upwelling of waters on the light side of the front and downwelling on the dense side (e.g. Capet et al., 2008b).

The aim of this paper is to demonstrate the impact that changing the horizontal resolution has on the vertical motion in numerical simulations of the KP region. We will compare and contrast a pair of regional numerical experiments, run at two different horizontal resolutions ($1/20^\circ$ and $1/80^\circ$) to investigate the relative importance of mesoscale and sub-mesoscale processes to the vertical circulation. A Lagrangian tracking tool is used to quantify the transport due to these fields. We highlight that the use of high horizontal resolution and realistic topography in our model is a significant advance on the series of numerical models previously used to investigate the dynamics of the area. In particular, this is the first comparative study of differences between mesoscales and sub-mesoscales under Southern Ocean conditions. Finally, motivated by the necessity of studying ocean processes in a high productivity area such as the Kerguelen Plateau, this work lays the foundation for a future study into iron transport.

The paper is organised as follows: section 2.2 is divided into three parts, where sections 2.2.1 and 2.2.2 describe the ocean numerical models used to simulate the circulation and section 2.2.3 the Lagrangian particle tool used to study the transport of particles. The validation of the model through a comparison of the mean circulation with observations is given in section 2.3. Section 2.4 shows the results of the different experiments, while section 2.5 gives a discussion of the results.

2.2 Method

The circulation in the area of KP is simulated using the primitive equation model MIT-gcm (Marshall et al., 1997). We use realistic bathymetry from the 1 minute resolution Shuttle Radar Topographic Mission dataset (SRTM, Smith and Sandwell, 1997) and we set the maximum depth at 5000 m (Fig. 2.2). To capture the dynamics at the surface while resolving the topographic features, we use 150 vertical levels with a variable vertical resolution (10 m thickness at the surface, increasing to 50 m at roughly 2000 m depth) via the profile $\Delta z = 30\text{ m} - 20 \tanh[(1000 + z)\pi/1500]\text{m}$. The vertical grid has z-coordinates and uses partially filled cells for the bathymetry (Adcroft et al., 1997), to reduce the vertical velocities arising close to the topography (which were found to otherwise dominate

the deep velocity field when using a step topography). The model uses the non-linear free surface algorithm (Adcroft and Campin, 2004), with a free-slip condition at the northern and southern boundaries (zero-stress at the boundaries) and bottom drag with a typical quadratic drag coefficient of 0.0025. Furthermore, the model uses the Jackett and McDougall (1995) equation of state for seawater. We have implemented different experiments using two horizontal resolutions: one with $1/20^\circ$ resolution, denoted KERG20 for the remainder of this paper, and one with $1/80^\circ$ resolution (KERG80). In section 2.2.1 we present the configuration for KERG20 and in section 2.2.2 the KERG80 implementation. An outline of the physical parameters used for the two models is given in Table 2.1.

The data, in the form of instantaneous fields, are stored daily and the analysis is performed over 200 days for both resolutions. The analysis is performed over an inner area of the domain (69°E - 82°E , 43°S - 53°S) to avoid unrealistic boundary effects arising in KERG80. Analyses include standard surface flow metrics and the statistics of interior vertical velocity. However, the primary mode of analysis is a Lagrangian tracking system which is described in section 2.2.3.

2.2.1 MITgcm configuration for $1/20^\circ$ resolution

The domain of the KERG20 simulation is 57°E - 129°E , 70°S - 35°S . With a horizontal resolution of $1/20^\circ$ the zonal grid spacing ranges between approximately 4.5 km on the northern boundary and 1.9 km to the south, while along the meridional direction the resolution is approximately 5.6 km. At this resolution, the number of points per Rossby radius, in the longitudinal direction, ranges between 12 (northern boundary) and 2, while a range between 5 and 1 has been estimated in the latitudinal direction (Rossby radius derived from Chelton et al., 1998). The $1/20^\circ$ resolution is therefore considered to be eddy-resolving over most of the domain, including the sub-domain of analysis, with effective resolution degrading close to Antarctica.

Southern Ocean State Estimate (SOSE) annual-averaged climatological fields for the year 2005 (Mazloff et al., 2010) are used to estimate surface fluxes of momentum, heat and freshwater. The circulation is forced at each timestep by a temporally constant wind stress (vectors in Fig. 2.2), with values taken from SOSE, relaxing to zero at the northern boundary in a layer of 1° width (to prevent the development of strong counter-currents along the northern boundary). At the surface, temporally constant fresh-water fluxes are applied at each timestep and the climatological SST is used to restore the surface with a timescale of 15 days (Fig. 2.3). There is no seasonal cycle in the model forcing.

The northern boundary is linearly relaxed to SOSE temperature and salinity climatology over a 1° wide sponge layer, with a restoring timescale of 8 days (Fig. 2.4), while bottom topography of the Antarctic continental slope closes the domain on the southern boundary. The domain is zonally periodic; topography, restoring and forcing fields have been smoothed in a band of approximately 4° wide near the western and eastern boundaries and made periodic.

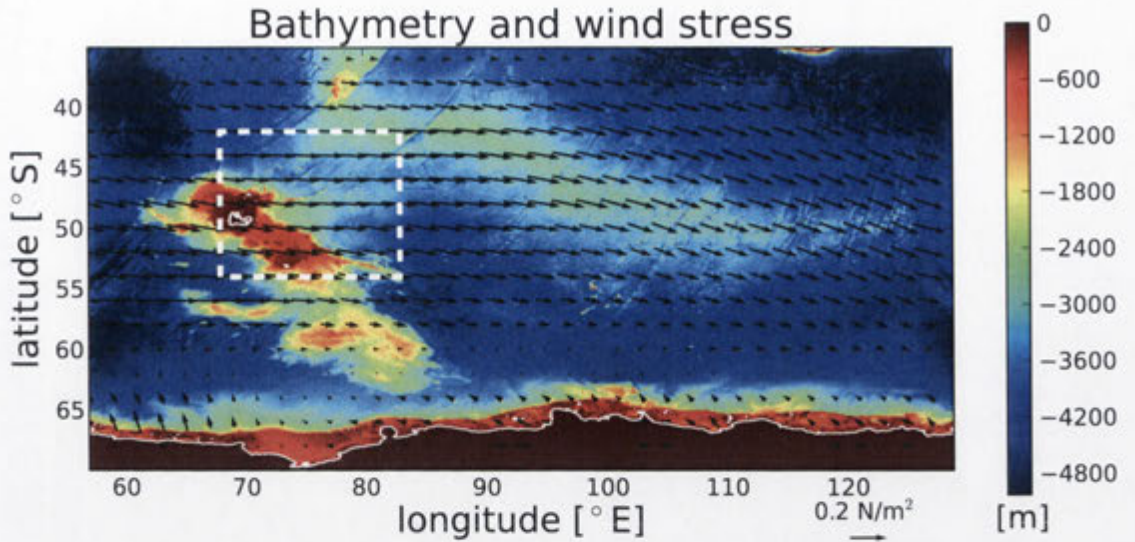


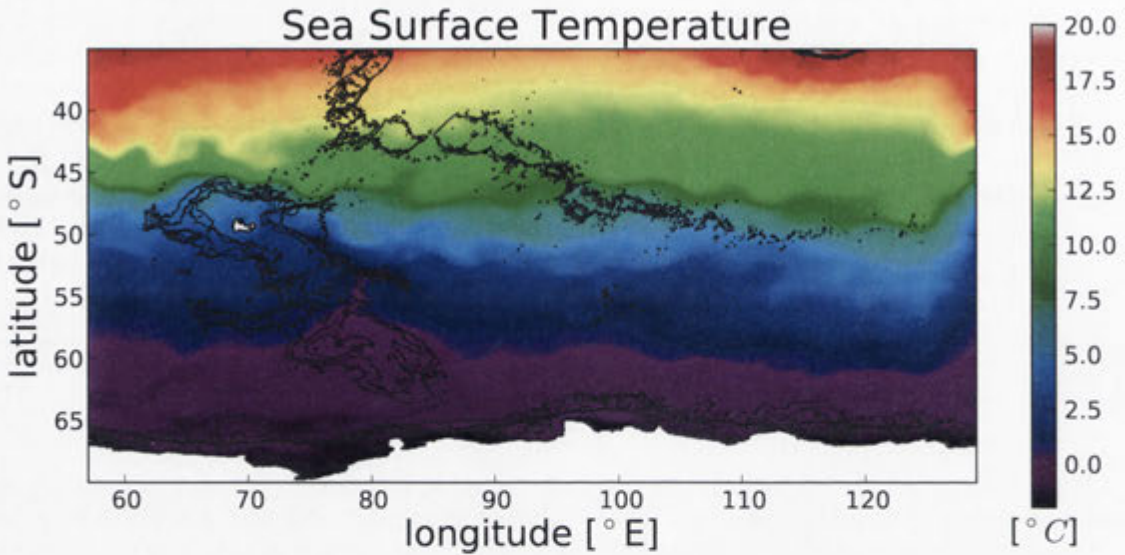
Figure 2.2: SOSE wind stress field overlying the 1-min SRTM zonally periodic bathymetry. The white contours represent the coastlines and the white box defines the domain of the $1/80^\circ$ model.

2.2.2 MITgcm configuration for $1/80^\circ$ resolution

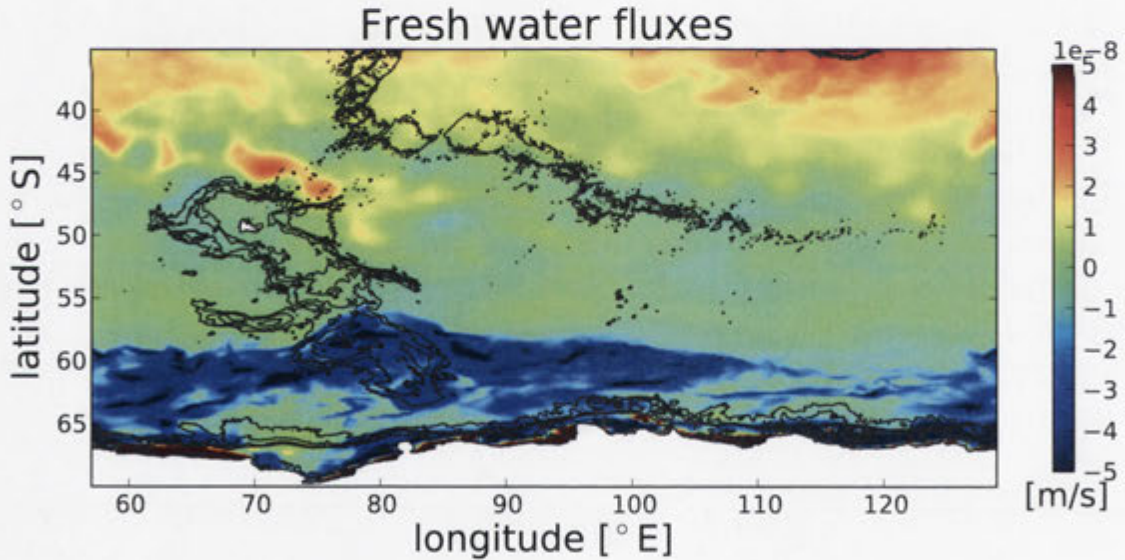
The domain for the KER80 case is a $15^\circ \times 12^\circ$ sub-domain of KER20, 68°E - 83°E , 42°S - 54°S as represented by the white box in Fig. 2.2. The resolution in this case gives a zonal grid spacing between 0.8-1.0 km and a constant meridional grid size of 1.4 km. In this case, we estimate a range of approximately 11 to 23 points (longitudinal direction) and of 6 to 17 (latitudinal) points per Rossby radius. The model is nested in KER20 using one-way open boundary conditions for zonal and meridional velocities, temperature, salinity and sea surface height prescribed by KER20 daily snapshots. Surface conditions of temperature, salinity, horizontal velocity and sea surface height are also restored to KER20 daily fields. For the KER80 bathymetry, the interior points have been interpolated directly from the 1-min SRTM bathymetry and the boundary points from KER20 for consistency. To reduce reflections from the open boundaries we use relaxation boundary conditions for temperature and salinity, with a relaxation time scale of 2 hours and a 20 point linear sponge.

2.2.3 Connectivity Modelling System

The Connectivity Modelling System is used as an offline tool to study the sensitivity of transport to the horizontal resolution (CMS, Paris et al., 2013). Lagrangian particle-tracking models are techniques used to study the circulation of the ocean and the associated response of ecosystems (e.g. van Sebille et al., 2009). In this paper we will use the Lagrangian trajectories to focus on the physical properties of the model, highlighting the differences that the KER20 and KER80 cases have on the horizontal and vertical transport.



(a)



(b)

Figure 2.3: SOSE climatology surface field from 2005: (a) sea surface temperature and (b) fresh water fluxes (negative values represent fluxes into the ocean). The grey contour lines show topographic depths, with a contour interval of 600 m. The white colour represents land.

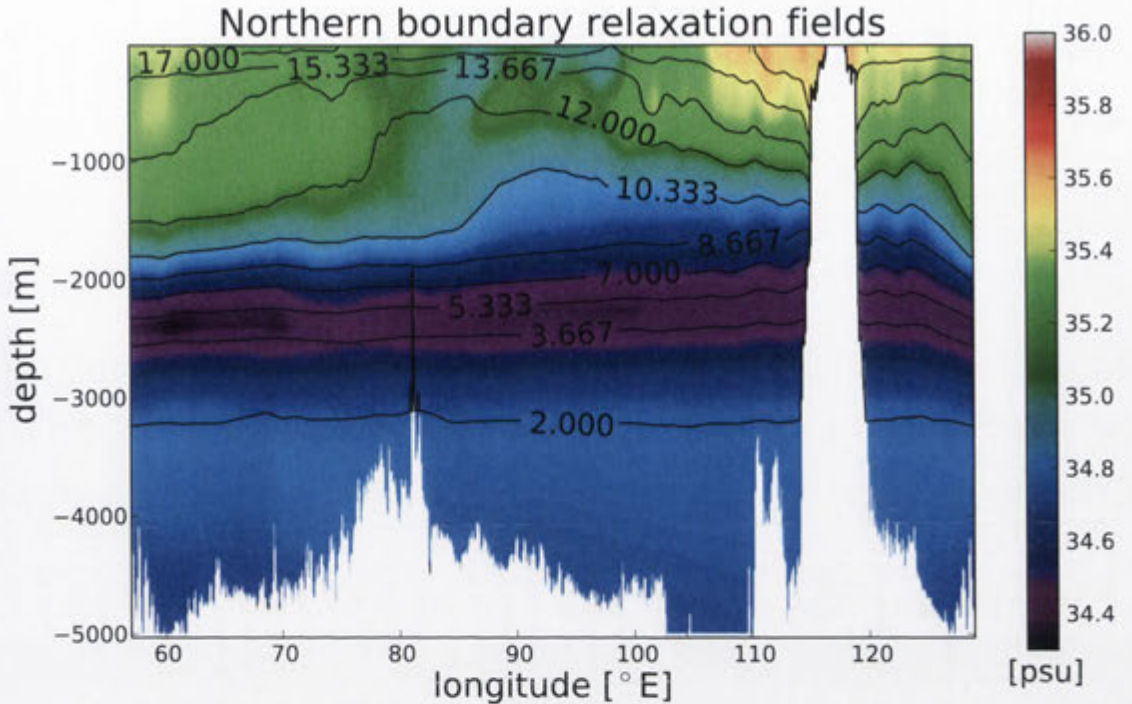


Figure 2.4: Northern boundary restoring salinity (in colour) and temperature (black lines, units are $^{\circ}\text{C}$) fields for KERG20.

We performed several simulations, driving the CMS with daily snapshot fields of zonal, meridional and vertical velocities. The advection of the particles is performed with a 60 second timestep, for a maximum integration time of 100 days (or until the particle exits the region of interest). It should be noted that the Lagrangian tracking takes into account purely resolved advective, but not diffusive, contributions to transport (including within the surface mixed layer).

An advantage of the Lagrangian analysis is that one can track particles either forward or backward in time. We use both of these in our analysis. We track the particles backward in time to study the water sources for particles arriving at the surface in the region of the eastern KP bloom. We integrate particles forward in time to investigate the different patterns of flow from waters upstream of KP, and their sensitivity to initial location and horizontal resolution. The location of the particle placement for the two different analyses is shown in Fig. 2.1. For the backward case 800 particles are placed along a line at 76°E , between 48°S and 52°S and at a depth of 5 m (red markers in Fig. 2.1). Other experiments have been run forward in time, with particles initialised in two different locations: one case north of the plateau and one south. In the first experiment we released particles along a transect at 70°E between 44°S and 49°S (black markers in Fig. 2.1), in order to track the contribution of the strong stream of the ACC north of KP. For the second case the particles were released south of KP (at 70°E between 50.5°S and 53°S , green markers in Fig. 2.1) to investigate the possible sources of waters for the bloom occurring

Description	KERG20	KERG80
Horizontal resolution	1/20°	1/80°
Horizontal gridpoints	(1440 × 700)	(1200 × 960)
Vertical levels	150	150
Coordinates	spherical	spherical
Momentum and tracers timestep	120 s	60 s
Tracers advection scheme	7 th order one-step monotonicity-preserving (Daru and Tenaud, 2004)	non-linear 3 rd order with Flux Limiter
Vertical mixing of tracers and momentum	K-profile parameterisation (KPP, Large et al., 1994)	K-profile parameterisation (KPP, Large et al., 1994)
Background vertical viscosity	$5.66 \times 10^{-4} \text{ m}^2\text{s}^{-1}$	$5.66 \times 10^{-4} \text{ m}^2\text{s}^{-1}$
Background vertical diffusivity	$1 \times 10^{-5} \text{ m}^2\text{s}^{-1}$	$1 \times 10^{-5} \text{ m}^2\text{s}^{-1}$
Harmonic Leith horizontal viscosity coefficient	1.2	1.2
Biharmonic Leith horizontal viscosity coefficient	1.5	1.5
Horizontal salinity and temperature biharmonic diffusivity	$1 \times 10^8 \text{ m}^4\text{s}^{-1}$	$1 \times 10^8 \text{ m}^4\text{s}^{-1}$
Spin-up time	40 years	1 year

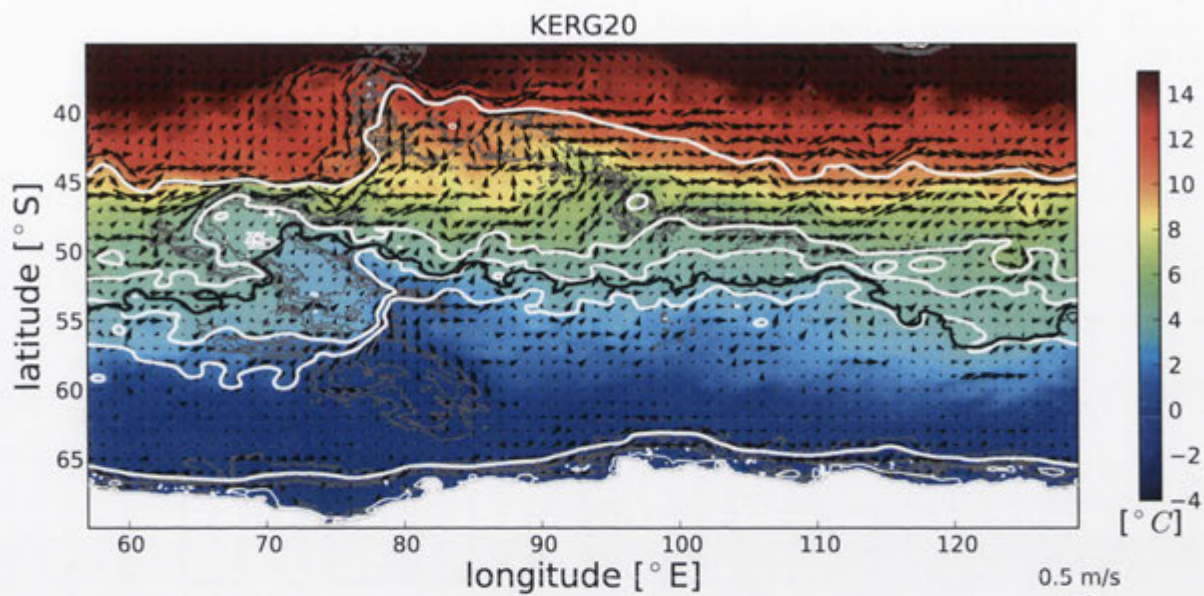
Table 2.1: Parameters used in the model.

over the plateau. In each case, the particles were placed with a spatial step of 0.005° and released simultaneously. We obtained similar patterns using a subset of particles initially spaced 0.5° apart, and in numerous additional Lagrangian experiments (data not shown) confirming the robustness of our results.

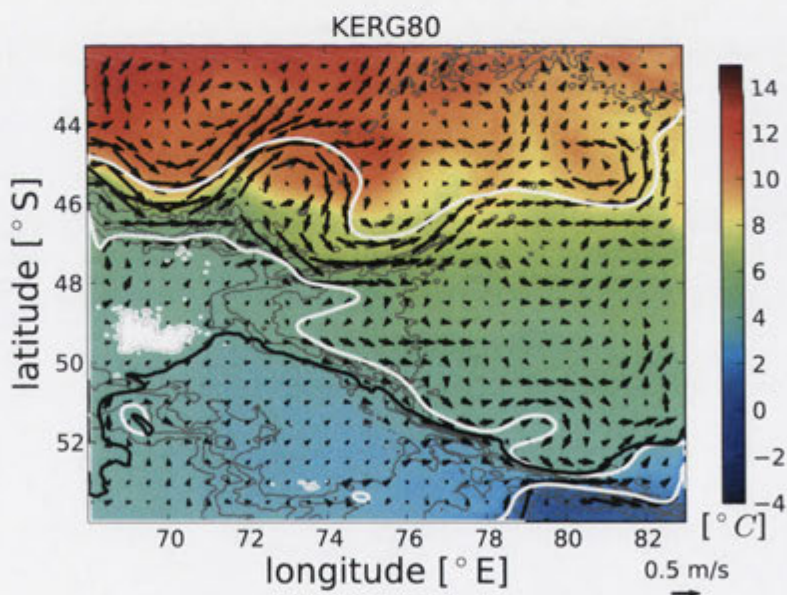
We tested the robustness of the daily sampling by temporally sampling the case with initial depth at 200 m, using the model output with a frequency ranging between three hours and two days (not shown). We found that, while the individual paths of the particles were not identical (due to the chaotic nature of the ocean circulation), the vertical displacements presented a strong correlation between the different cases.

2.3 Model evaluation

The mean circulation (Fig. 2.5) captures the main features of the Indian sector in the Southern Ocean (e.g. Park et al., 2008b). Constrained by the KP bathymetry, two main branches of the ACC are resolved, one flowing north of the KP (evident at both resolutions) and one in the Fawn Trough, which in the KERG80 case is near the edge of the domain (Fig. 2.5 b). These flows are very strong and reach mean magnitudes of 1 m s^{-1} , values which are comparable with the near-surface velocities derived from drifters by Park et al. (2008b). In the KERG80 case we also found a persistent meander centred



(a)



(b)

Figure 2.5: Temporal mean of sea surface temperature (in colour) for (a) KERG20 and (b) KERG80. White contours represent contours of temporal mean of SSH, the black line shows the 3°C contour and the grey lines show the bathymetry levels for the first 3000 m, with a step of 600 m. The black arrows represent the surface mean flow.

at 73°E and 46°S, a feature that has been investigated by the Southern Ocean FINE structure project (SOFINE, Naveira-Garabato et al., 2009) and which will be analysed in section 2.4.2. Furthermore, the Fawn Trough current presents a local circulation which is also comparable to observations. In particular, the flow shifts northward at about 78°E, following the bathymetry of the channel, and is then deflected eastward (at 80°E), merging with the northern ACC branch. Finally, a weak cyclonic circulation develops on the plateau, with magnitudes smaller than 0.1 m s^{-1} .

A good indicator of the properties of water masses is represented by oceanic fronts, defined in relation to temperature and salinity fields (Sokolov and Rintoul, 2009a). From the temporal mean of the sea surface height ($\overline{\text{SSH}}$), some main frontal branches can be identified: the black line in Fig. 2.5 represents the 3°C isoline and in white we show indicative contours of $\overline{\text{SSH}}$. The $\overline{\text{SSH}}$ contours are not evenly spaced, but they have been chosen because of the resemblance to observed ACC fronts: they align with frontal patterns given by the temporal mean of $|\nabla_H \text{SSH}|$. Although a detailed analysis of position and properties of the ACC fronts in our simulation is beyond the scope of this paper and a precise identification of fronts, comparable to realistic structures found by Sokolov and Rintoul (2009a), is not possible here, we can still identify typical frontal patterns, such as the Subtropical (in the KERG20 case, the northernmost white line) and the Polar front (the closest front to the Kerguelen Island).

A quantitative assessment of the model was conducted by computing the cumulative ACC transport across a path as shown by the colored line in Fig. 2.6. For the choice of the integration path, we took into account the different contributions to the eastward transport from the Kerguelen Plateau. This diagnostic is in good agreement with transports evaluated by Park et al. (2009), especially in the area north of the Kerguelen Island and in the Fawn Trough, red and blue branches in the figure, respectively. On the Plateau, between the Kerguelen and Heard Islands (green line) and between Heard Island and the Fawn Trough (magenta line), we found a total transport of 2 Sv ($1 \text{ Sv} = 10^6 \text{ m}^3 \text{ s}^{-1}$), which is 6 Sv less than in Park et al. (2009). Given the large range of modeled and observed transports across the subsections (1 to 120 Sv), we feel that this discrepancy is minor.

The surface 9-month average of the eddy kinetic energy (EKE) from a regional high-resolution altimetry product of the Kerguelen Plateau (RegionalKerguelen experimental product from AVISO) was compared with the model 200-day temporal mean, shown in Fig. 2.7 a. The three datasets show that the EKE is much larger in the area east of the plateau, away from the topography, and weaker over the plateau. Compared with the AVISO dataset, the magnitude of EKE in the region east of the Kerguelen Plateau is approximately a factor of 2 larger in KERG20; this discrepancy is largely eliminated when spatial filtering on scales similar to that used in satellite data processing is applied. The difference between observed and modelled EKE increases to be a factor of 4 larger in KERG80, which is most likely due to the additional fine scale variability at high resolution. We also calculated total kinetic energy spectra in the KERG80 region, at different depths,

by averaging zonally and in time (200-day mean). In Fig. 2.8 we show the spectra at 5 m depth. The energetic small-scales exhibit a typical slope $\propto k^{-2}$, comparable with previous findings (e.g. Capet et al., 2008a,c; Klein et al., 2008).

We conclude that, despite the idealised nature of our simulations, the dynamics of the Kerguelen area are well captured. In the following sections, we will present our results and discuss how the two resolutions impact the ocean circulation.

2.4 Results

We examine the differences in the circulation between the two experiments and the impacts that the small-scale features in the KERG80 case have on the vertical velocity (section 2.4.1) and transport of Lagrangian particles (section 2.4.2). In the following, horizontal spatial averages are denoted by $\langle \cdot \rangle$ and 200-day temporal averages by an overbar ($\bar{\cdot}$). A video of the surface temperature, velocity and relative vorticity at the two resolutions can be found in the supplementary material.

2.4.1 Frontal structures

We begin our analysis by comparing the surface velocity and vorticity fields from both resolutions. Figure 2.9 shows the emergence of transient localised fronts and fine-scale structures when increasing the resolution. The patterns that emerge in the KERG80 vorticity field are characteristic of features captured by resolutions of $O(1 \text{ km})$ (Capet et al., 2008a). These structures have high values of vertical relative vorticity, $\zeta_z = v_x - u_y$, localised in stretched filaments and at the edges of the mesoscale eddies (not shown).

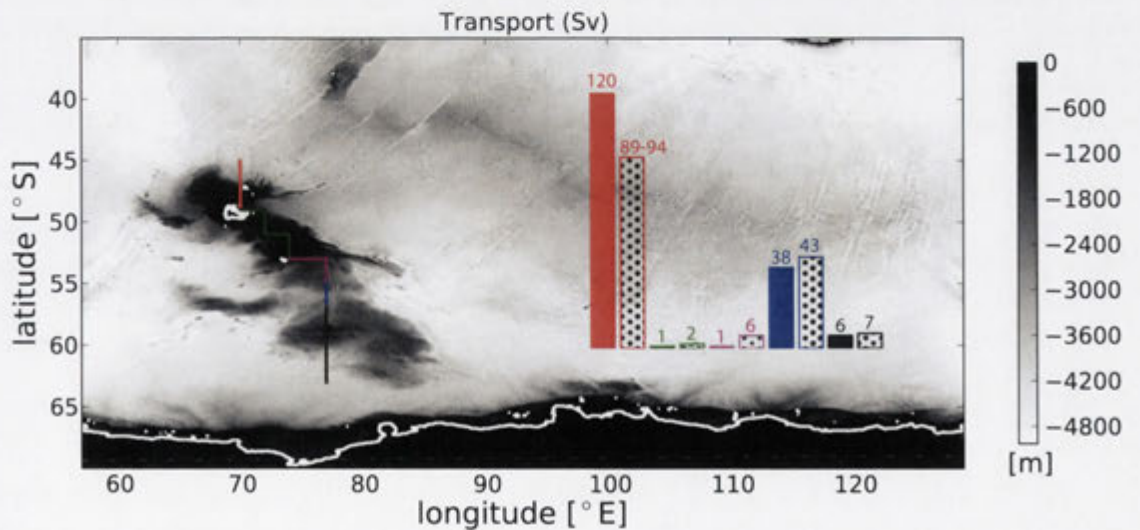
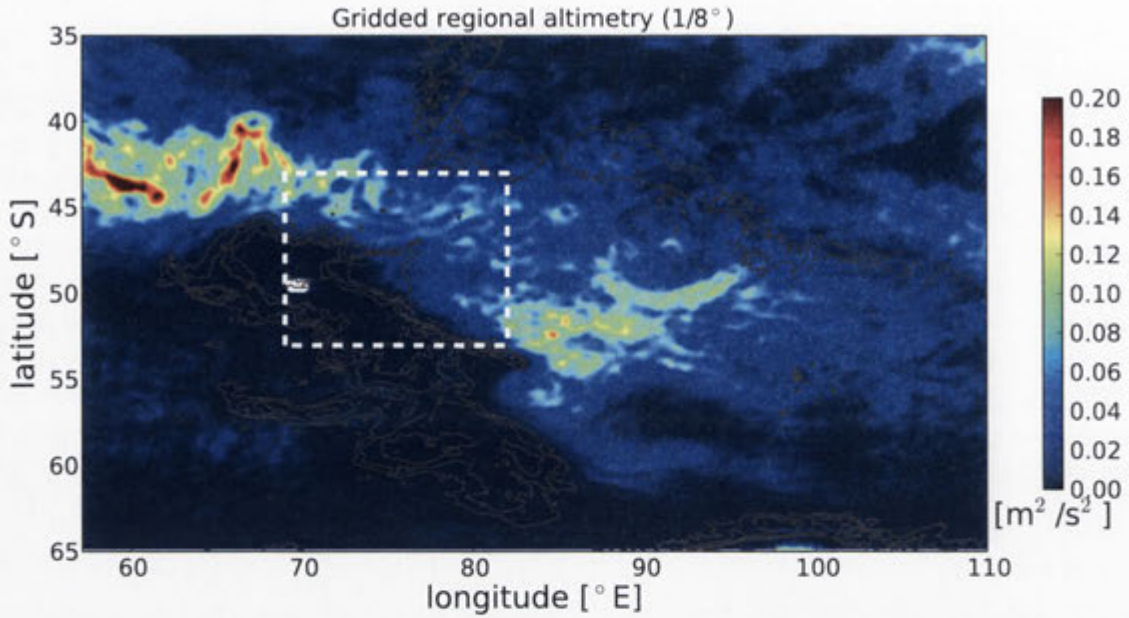
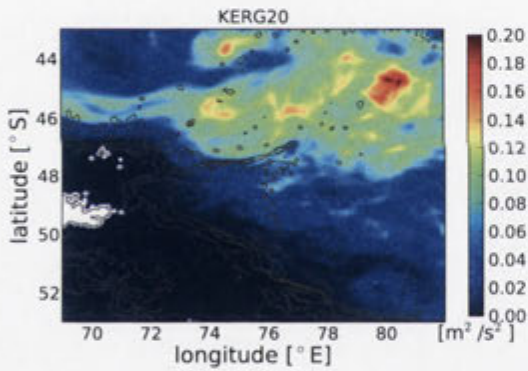


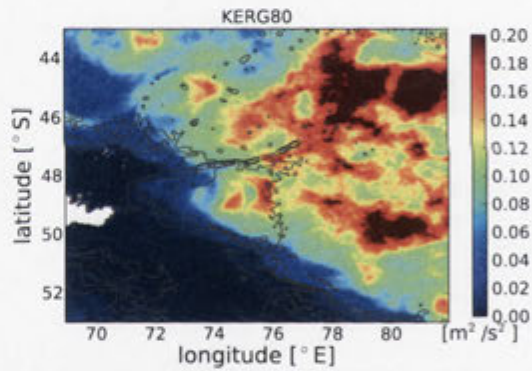
Figure 2.6: Cumulative transport for the KERG20 experiment, following the path drawn on the picture. Numbers are transports in Sv and the dotted bars report transports from Park et al. (2009).



(a)



(b)



(c)

Figure 2.7: (a) 9-month average (05/2011 to 02/2012) of the eddy kinetic energy (resolution of $1/8^\circ$), computed from a regional high-resolution altimetry product around the Kerguelen Plateau (data from AVISO); the white box indicates the area in panels (b) and (c). The 200-day average of surface eddy kinetic energy for (b) KERG20 and (c) KERG80 (the colormap is saturated and peak values are $0.4 \text{ m}^2 \text{ s}^{-2}$). Contours are bathymetry levels with 600 m steps.

There, ζ_z is comparable with the Coriolis frequency f , as measured by the Rossby number $\text{Ro} = |\zeta_z/f|$. A common feature observed at both resolutions is the absence of strong patterns over the plateau. Here, a weaker velocity field is present (Fig. 2.9 a, b), because the plateau acts as a natural barrier to the strong ACC fronts coming from the west. In the region east of the KP, this ACC flow, interacting with topography, generates instabilities and filaments.

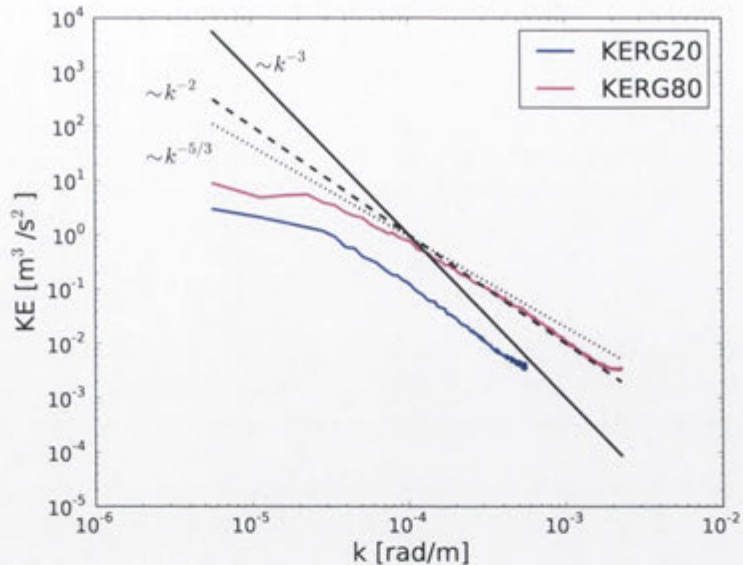


Figure 2.8: Time and zonal average of total kinetic energy spectra at 5 m depths, for KER20 (blue) and KER80 (magenta), computed in the KER80 region. Plotted are also typical spectrum slopes: -3 (solid), -2 (dashed) and -5/3 (dotted).

The strength of frontal structures increases with horizontal resolution. Figure 2.10 a, b show the surface density gradient, $|\nabla_H \rho(x, y)|$, at 50 m depth (where ∇_H is the horizontal gradient and ρ the local density). A field of strong fronts emerges at high resolution, whose structures are connected to strong vertical motions (Fig. 2.10 d, f). We have compared the magnitude of the vertical velocity (w) with observations from the SOFINE experiment (Phillips and Bindoff, 2014). We found that vertical velocities in excess of 100 m day^{-1} are routinely observed in this region, implying that the magnitude of velocities seen in our KER80 experiment are realistic. However, w is weaker in the KER20 case which indicates that at this resolution the vertical motion (and its contribution to transport) may be underestimated (note the different scales in Fig. 2.10 c-f between KER20 and KER80). The location of w in relation to fronts is also shown in panels c-f. In the KER80 case, the collocation of these features is consistent with an ageostrophic secondary circulation mechanism, which arises in connection to frontogenesis (Capet et al., 2008b; Taylor and Ferrari, 2011). In fact, where the magnitude of $|\nabla_H \rho|$ is strong, a dipolar structure emerges for the vertical velocity (Fig. 2.10 d, f). Figure 2.11 shows a particular example of this collocation: peaks in $|\nabla_H \rho|$ generate vertical velocities of order 200 m day^{-1} in either direction on opposite flanks of the front. Figure 2.10 c, e indicate that in the KER20 case w is under-resolved, with patchy structures on the scale of the grid. In the KER80 case the vertical velocity is well defined and penetrates deep into the water column (panel f indicates a maximum local depth of 800 m), which is related to the mixed layer depth (white line in panels e and f). The mixed layer depth was computed using a mixed layer criterion of $0.05 \text{ }^\circ\text{C}$, which represents the temperature difference between the surface and the depth of the mixed layer. Vertical profiles of temperature indicate

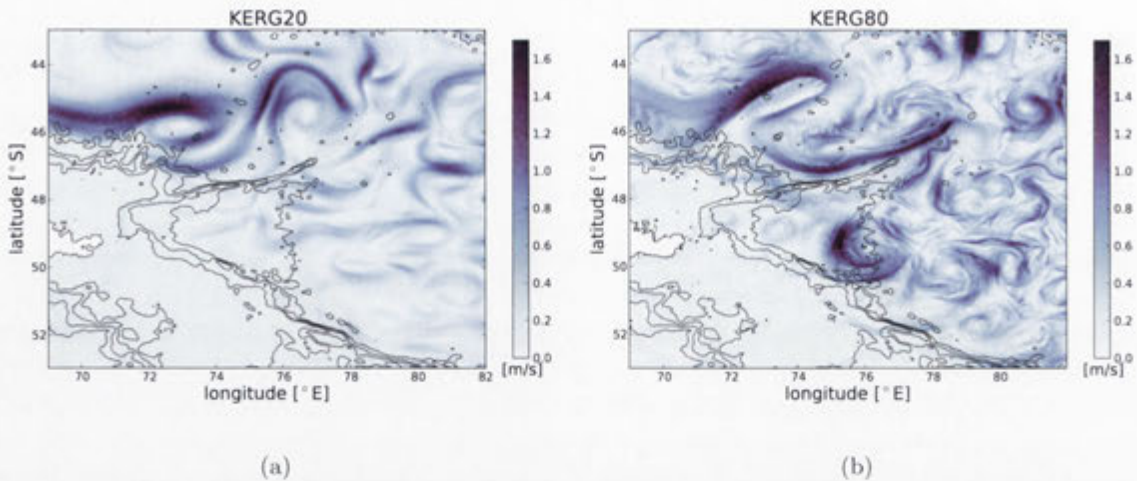


Figure 2.9: Snapshots of the magnitude of surface horizontal velocity for (a) KER20 and (b) KER80. In black are shown the topography contours for the first 3000 m, with an interval of 600m. The instantaneous fields are taken at the same model day.

that this choice more accurately depicts the depth of the mixed layer. We also point out that significant vertical displacement of particles requires persistent uplift/downlift, but since the horizontal velocities (Fig. 2.9 a, b) are three orders of magnitude larger than the vertical component (Fig. 2.10 c-f), this can occur only when the horizontal velocity aligns with extended regions of large $|w|$. The Lagrangian tracking method can be used to investigate this aspect (sections 2.4.2 and 2.5).

Another way to investigate the areas of major up/downwelling is the analysis of the temporal root mean square of the vertical velocity. We have calculated this metric for each resolution case, on a single level close to the surface (50 m depth) and computed the temporal mean over 200 days. We indicate it as $w_{rms,2D} = \sqrt{\overline{w^2}}$. The map, in Fig. 2.12, shows differences in the location, structure and magnitude at the two resolutions. We identify a region over the shallow plateau (number 1 in figure), where the vertical velocity is weak and the motion is mainly horizontal, at both resolutions. In the KER20 case the largest magnitudes are found in the northern half of the domain, while at $1/80^\circ$ resolution we can see two main areas, as indicated by number 2 and 3 in the figure. The second region presents strong vertical motion in the northern region, either located in the lee of topographic features or located in the southernmost area of the meander ($74^\circ\text{E}-76^\circ\text{E}$, $46^\circ\text{S}-47.5^\circ\text{S}$). Finally, the third region comprises the area from the eastern boundary of the plateau to the eastern side of the domain. In these last two locations the vertical motion is very strong and $w_{rms,2D}$ indicates the presence of filamentary structures.

Following the method presented by Capet et al. (2008a), we examine the vertical profile of the root mean square of w for each resolution. To highlight the contribution over the water column given by the different spatial structures present, the total field has been decomposed into the temporal mean (\bar{w}), mesoscale (w_M) and sub-mesoscale (w_S) components: $w = \bar{w} + w_M + w_S$. For the separation of the spatial scales at the mesoscale

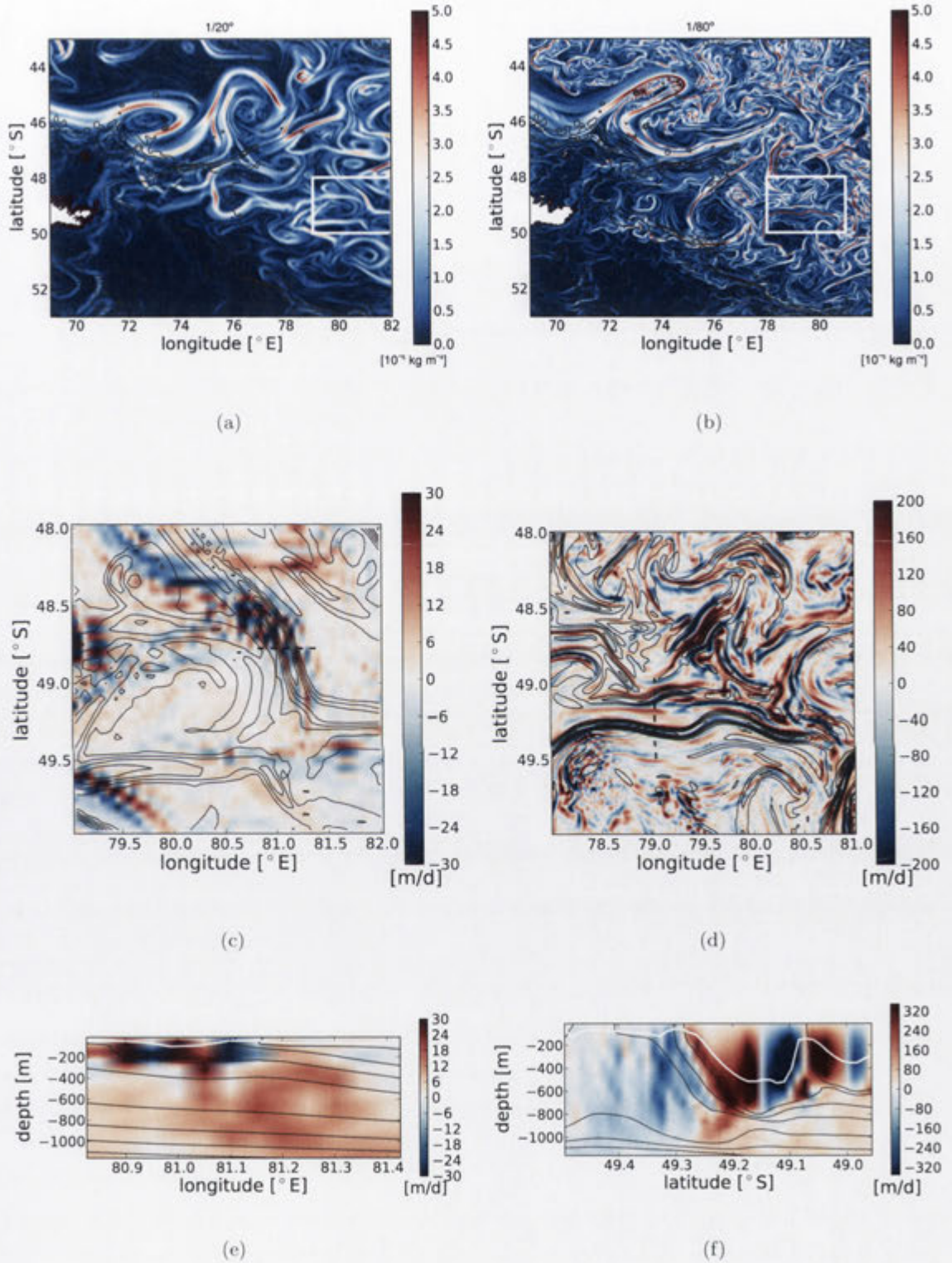


Figure 2.10: Frontal structures at approximately 50 m depth, for KERG20 and KERG80 cases. (a)-(b) $|\nabla_H \rho|$ (10^{-5}kg/m^4) and in black the topography contours for the first 3000 m, with an interval of 600 m. (c)-(d) $w(x, y)$ for the subdomains indicated by the white boxes in (a) and (b). In (c) and (d) contours represent $|\nabla_H \rho|$ with an interval of $1 \times 10^{-5} \text{kg/m}^4$ and the dashed black lines indicate the location of the vertical slices of $w(x, z)$ (e) and $w(y, z)$ (f). White lines in (e) and (f) indicate the mixed layer depths, while grey lines are isopycnals, with an interval of 0.1kg/m^3 . The instantaneous fields are taken at the same model day used in Fig. 2.9, for both resolutions. Note the different colour scales in (c)-(f).

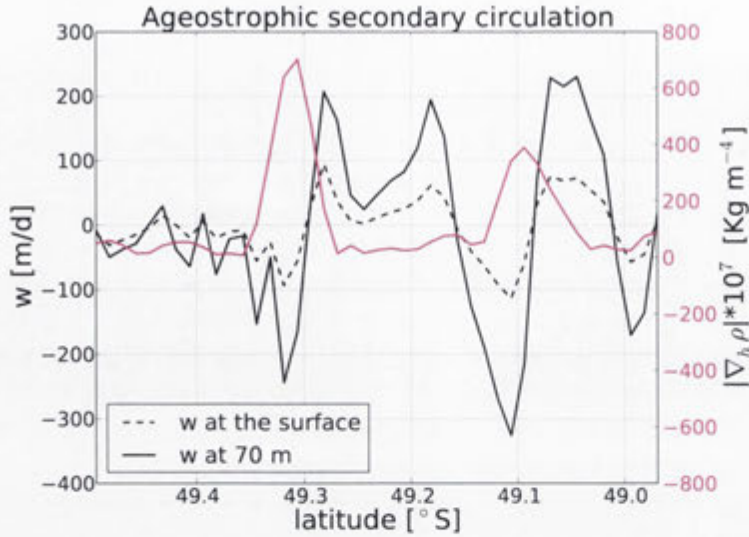


Figure 2.11: Meridional profiles of vertical velocities near the surface (5 m depth, dashed black) and at 70 m (solid black), for the dotted line shown in Fig. 2.10 d. The magenta line shows the profile for $10^7 |\nabla_h \rho|$ near the surface.

and sub-mesoscales, we applied a horizontal low-pass filter based on a spatial 2-dimensional convolution of $(w - \bar{w})$ with a constant rectangular window. The width of the window is 4 points for KERG20 and 16 for KERG80, so the filter has the same physical dimensions in both cases: the cutoff between the two scales is $1/5^\circ$, which corresponds to 22 km in the meridional and 15 km in the zonal directions, comparable to the 1st baroclinic Rossby radius in the KP region (Chelton et al., 1998). The mesoscale component, therefore, includes all the scales and variabilities except the finest sub-mesoscales. We computed horizontal spatial rms metrics over each level, which were then temporally averaged. Its sensitivity to the horizontal resolution is shown by the vertical profiles in Fig. 2.13. The notations shown in figure refer to: “ w_{rms} ” = $\sqrt{\langle w^2 \rangle}$, “ w_{Mrms} ” = $\sqrt{\langle w_M^2 \rangle}$ and “ w_{Srms} ” = $\sqrt{\langle w_S^2 \rangle}$. We point out that, purely due to the continuity condition, an enhancement of 4 times might be expected with a 4-fold increase of resolution. The rms profiles of w present the highest magnitudes in the KERG80 case, with the total w_{rms} 11-fold greater than the KERG20 profile. This increase in magnitude is particularly significant in the sub-mesoscale component, which reveals a strong signature close to the surface and to the bottom. The surface signature is dominated by sub-mesoscale activity, while mesoscale-induced vertical velocities are almost independent of depth. On the other hand, the sub-mesoscale component for KERG20 shows only minimal surface enhancement. The peak near the bottom is most likely due to flow interacting with topography. The mesoscale components and the topographically-induced sub-mesoscale velocities are similar in structure, although the magnitudes of each are larger at high resolution. Due to the enhancement of small scale components of velocity throughout the water column, we cannot exclude the presence of inertia-gravity waves in addition to

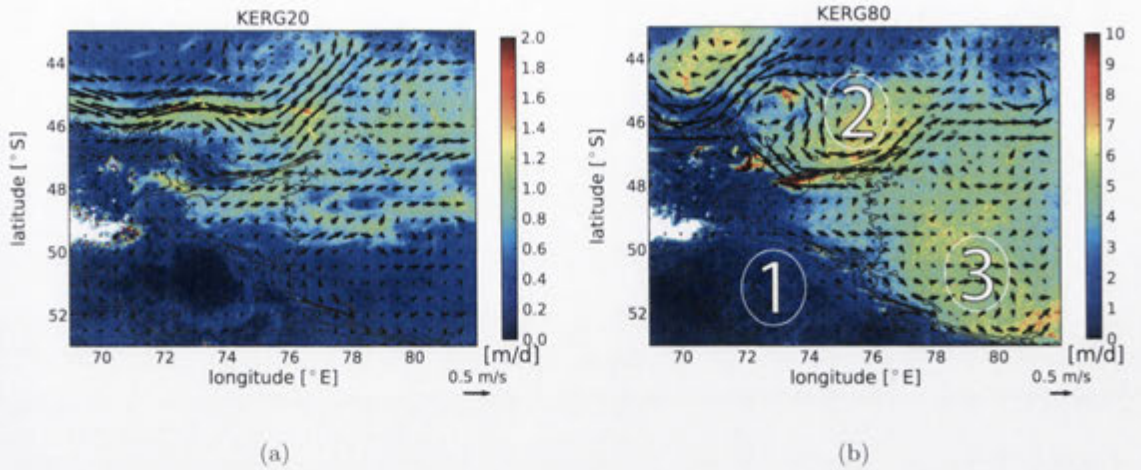


Figure 2.12: Two-dimensional map of the 200-day temporal root mean square of w at roughly 50 m depth for (a) KERG20 and (b) KERG80. The numbers in (b) indicate three different regimes of vertical motion (see text) and the arrows the temporal mean circulation at 50 m depth. The scales for $w_{rms,2D}$ are different in the two cases.

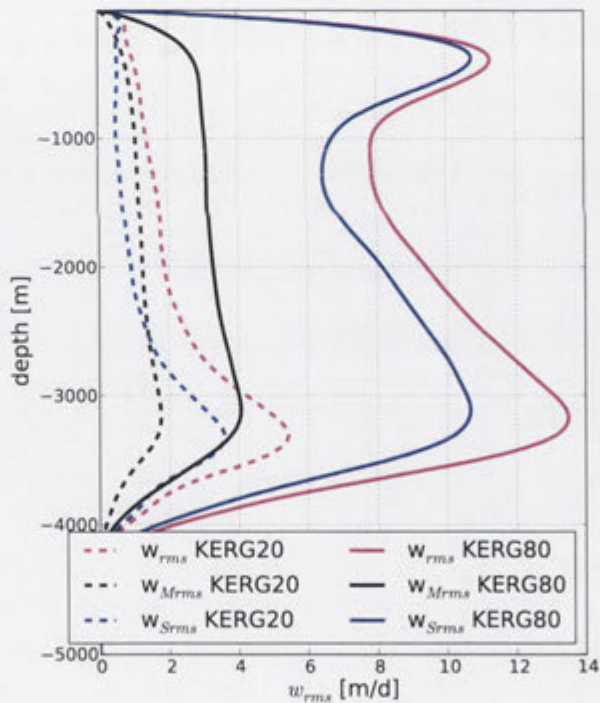


Figure 2.13: Vertical profiles of rms of the vertical velocity: total component (magenta), mesoscale (black) and sub-mesoscale (blue). Dashed lines show the profiles for KERG20, solid are for KERG80.

sub-mesoscales. The use of the Lagrangian model is therefore a valuable tool to estimate the net vertical transport.

These results show that the vertical velocity is stronger in the north and east side of the KERG80 domain, while over the plateau both the horizontal and vertical circulations

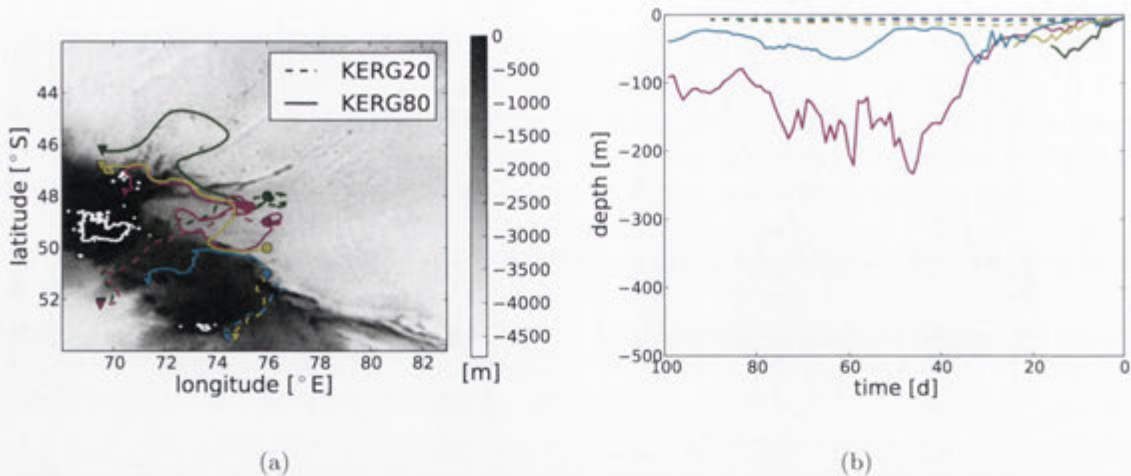


Figure 2.14: Example of Lagrangian particle trajectories over 100 days in the backward experiment for $1/20^\circ$ (dashed lines) and $1/80^\circ$ (solid) resolutions. The particles have been selected for display reasons and in order to capture the main paths. Horizontal paths are shown in (a), where coastlines are in white and the bathymetry is shown by the greyscale. Temporal vertical excursions are plotted in the panel (b).

are much weaker than the surroundings. Furthermore, the vertical velocity depends on the horizontal resolution and is enhanced at finer scales, especially near the surface. In the next section we will use the CMS (Paris et al., 2013) to investigate whether this feature results in more advective transport.

2.4.2 Particle analysis

The CMS Lagrangian particle model (Paris et al., 2013) is used to study the three-dimensional transport of particles in the flow, as a function of horizontal resolution. A series of experiments were implemented, tracking particles both backward and forward in time. The first series of experiments (backward) were designed to test the possible sources of surface water, in the lee of KP (red markers in Fig. 2.1). Here, 800 particles were placed at 5 m depth in each resolution experiment and their backward trajectories computed for the previous 100 days. An ensemble of representative trajectories for this case is shown in Fig. 2.14. The KERG20 particles are mainly derived from the south side of Kerguelen Island (approximately 95%) and in particular from the shallow plateau. In this case, just 8% of particles come from depths greater than 100 m (Fig. 2.15 a). On the other hand, more than 75% of the paths in KERG80 arrive via the circulation coming from the ACC and flowing along the eastern boundary of the plateau (61%) or in the strong meander north-east of the plateau (14%). The waters in this region are upwelled from deeper levels and 25% of the particles come from depths deeper than 500 m and 38% deeper than 100 m. The distribution of the trajectories as a function of depth, and integrated in time, is shown in Fig. 2.15 a, in which the KERG80 case presents sources of particles substantially deeper than in the lower resolution case.

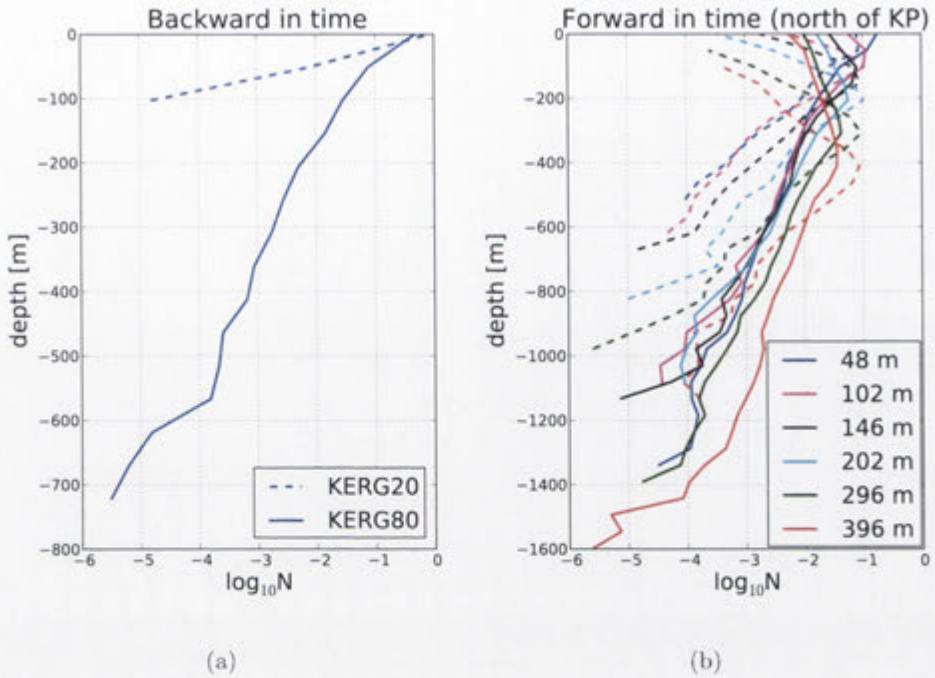


Figure 2.15: Log (base 10) of the particle counts at different depths with 50 m bins, in 6-hourly snapshots, over the 100-day integration and normalised by the total number of particles and snapshots. (a) Backward in time experiments (KERG20 is dashed, KERG80 is solid). (b) Forward experiments (including only particles released north of KP; colours refer to the depth of particle release; the dashed lines represent the KERG20 runs, while KERG80 results are shown by solid lines).

The second series of tests are run forward in time for up to 100 days and the particles are released at 6 different depth levels: $R_i = \{48, 102, 146, 202, 296, 396\}$ m. We performed two cases: (1) 1000 particles placed at each level in a location north of KP, inside the strong ACC (black markers in Fig. 2.1); (2) 500 particles released at each depth level, south of Kerguelen Island, as indicated by the green markers in Fig. 2.1. These last two experiments were performed to study the transport around and over the plateau and understand how the particles are advected in the water column. Fig. 2.16 shows example paths for the forward experiment (north of KP case), with initial depths at 200 m. At each resolution a fraction of particles flows through the meander in which the particles are mainly transported horizontally and their position in the water column does not substantially change, irrespective of resolution. This behaviour is well represented by the black lines passing through the meander in Fig. 2.16. Moreover, in the KERG80 case the particles (e.g. yellow and magenta in Fig. 2.16) coming from locations close to the plateau follow the circulation that develops along the eastern boundary of the plateau. The transport of particles here involves strong high-frequency upwelling/downwelling (Fig. 2.16 b) while carrying the waters into the eastern region of the domain (Fig. 2.16 a), which coincides with the area of small-scale activity (Fig. 2.10). The particles in KERG20 still reach

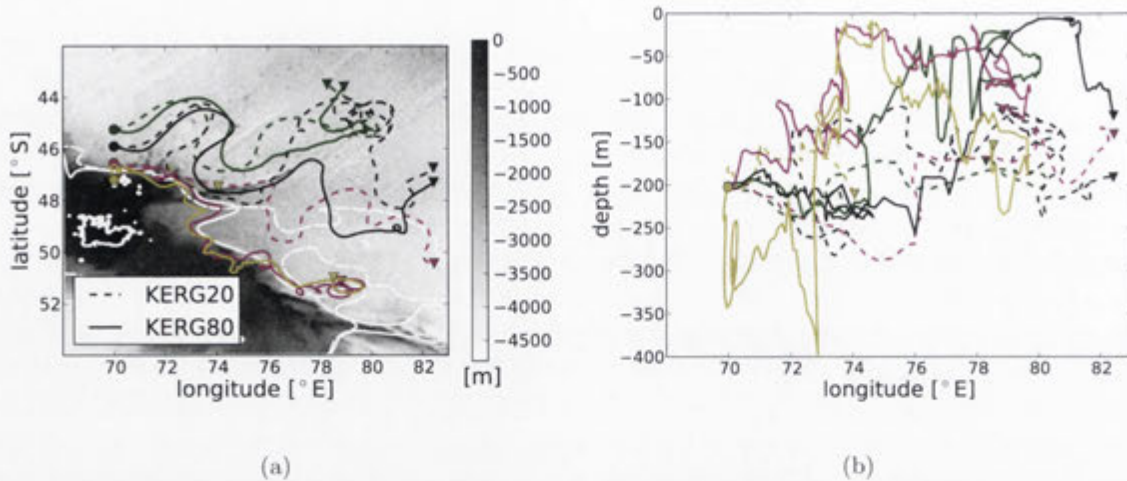


Figure 2.16: Lagrangian particle trajectories (over at most 100 days) in the forward experiment (north of KP) for (dashed lines) $1/20^\circ$ resolution and (solid) $1/80^\circ$, with particles released at 200 m depth. (a) shows horizontal paths, while vertical displacement of particles, as a function of longitude, is shown in panel (b). Shown in (a) are also $\overline{\text{SSH}}$ contours (white) as in Fig. 2.5. The particles have been selected with a step of 0.65° for display reasons and in order to capture the main paths. Color mapped in panel (a) is the bathymetry.

depths of 800 m (cyan line in Fig. 2.15 b), but only rarely, and their transitions are much slower (e.g. Fig. 2.16 b). We suggest that this behaviour, as will be discussed in the next section, is due to the lack of sub-mesoscale structures.

Furthermore, the KERG80 case generates a rapid spread of particles in the water column, as shown by the example of Fig. 2.16 and summarised in Fig. 2.15 b. In Fig. 2.15 b we present the number of particles found at different depths, integrated in time for up to 100 days. The diagnostic was evaluated for those trajectories reaching 74°E , in the domain defined by areas 2 and 3 of Fig. 2.12. The dramatic difference in the distributions at the two resolutions is captured in all the experiments. Both the excursions to depths and to shallower levels (down to 200 m) are significantly different in KERG20 and KERG80 and in the lower resolution cases the spreads are more gradual, remaining concentrated closer to the release depths. For those particles reaching a representative arrival depth in the range of (10–150) m (labeled A in Fig. 2.17) we have evaluated the percentage of their trajectories which had previously passed through other depths (indicated by S_n , $n = 1, 2, 3$ in Fig. 2.17). The computation was done for each experiment with particles released from initial depth R_i , $i = 1, 2, \dots, 6$. As expected from the results of Fig. 2.15 b, fewer particles are found in the surface levels of the KERG20 experiments and, for those trajectories reaching the arrival range depths, KERG80 generally gives more vertical exchange (exceptions are R_5 and R_6 passing through S_2). Some particles of KERG80 track an excursion of at least 450 m (approximately 10% in the R_6 particle release from 396 m). Particles released from $R_{1,2,3}$ quite commonly reach depths exceeding 400 m (S_2) or even 600 m (S_3) before returning to A in KERG80; this never occurred in KERG20. There are no KERG20

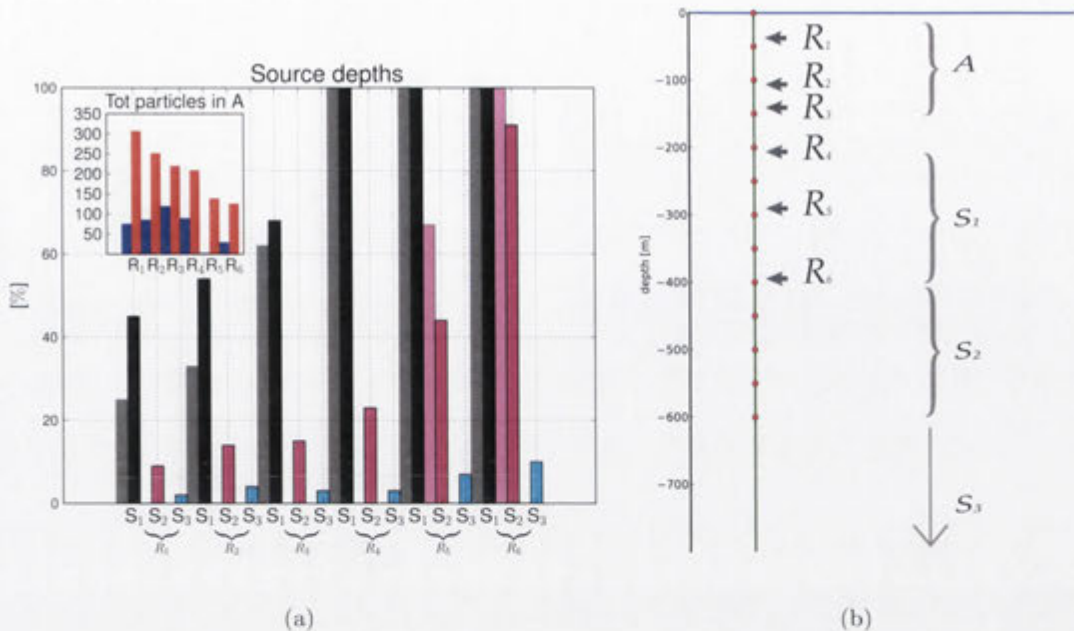


Figure 2.17: Depths through which particles have passed (over at most the previous 100 days) before their last arrival in the range 10–150 m (arrival depths indicated by A). (a) The total number of particles reaching the arrival depths as a function of the release depths ($R_i = \{48, 102, 146, 202, 296, 396\}$ m) is plotted in the inset. Here, blue bars are for KERG20 and red for KERG80. The main part of the plot represents the % of those particles reaching A, grouped by each release depth, and passing through different source depths (S_n , $n = 1, 2, 3$) before reaching A. S_1 refers to source depths in the range (200–400) m (black), S_2 to (400–600) m (magenta) and S_3 to depths below 600 m (cyan). The pale-coloured bars are for KERG20, while solid bars are for KERG80. In panel (b) a schematic plot of arrival, source and release depths is shown.

trajectories found in the arrival range coming from depths below 600 m, in contrast to KERG80, in which the % of particles reaching A from below 600 m was as high as 10%.

In the last group of experiments particles are integrated forward in time from locations south of KP (Fig. 2.18). The vertical spread of particles show similarities at both resolutions (Fig. 2.18 c, d) at each depth of release (only particles with 50 m starting depth are shown), while the horizontal paths indicate a sensitivity to the resolution (Fig. 2.18 a, b). A common pattern in the KERG20 case is a northward circulation above the plateau that drives the particles with release north of 51°S along the topographic contours. Moreover, almost none of these particles are found over KP west of 72°E in this case. At the highest resolution, the horizontal trajectories show a different behaviour. We found a wide horizontal spread of particles above the plateau, mainly of those particles released north of 51°S .

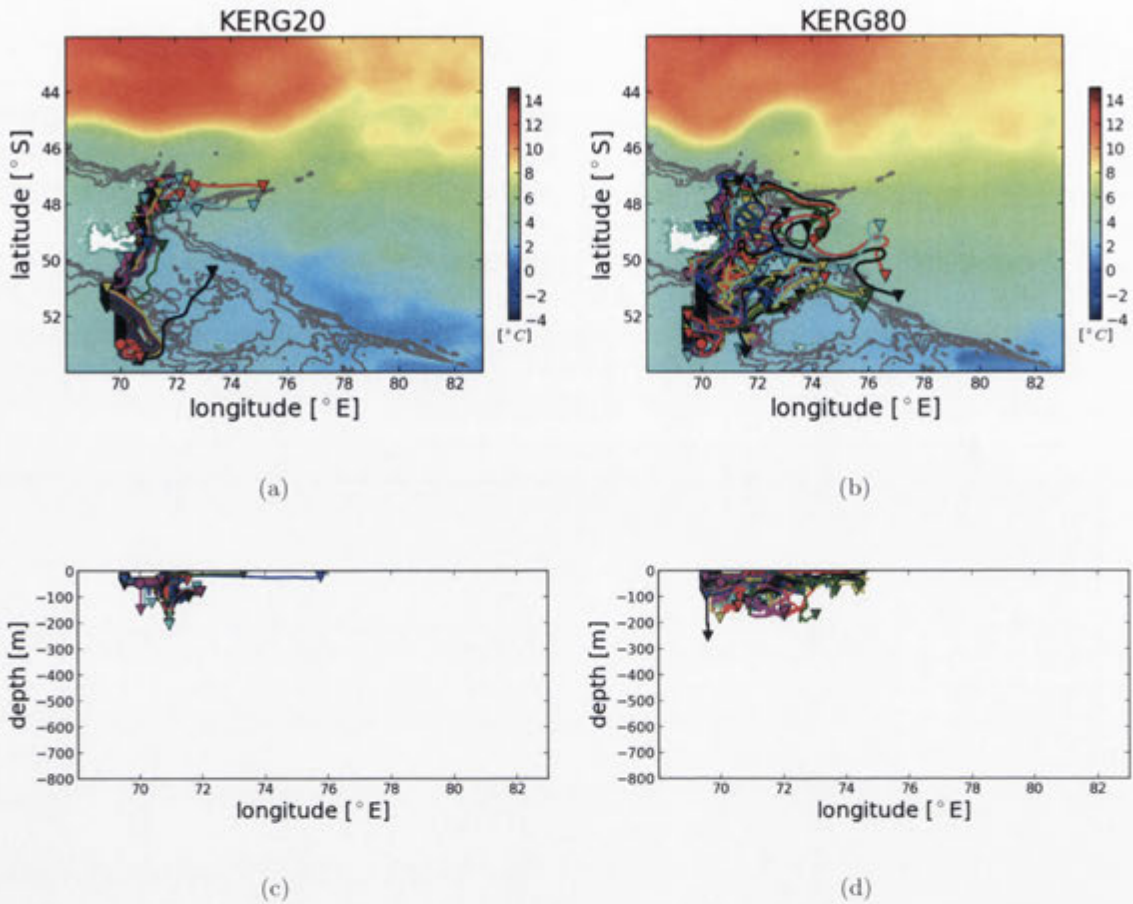


Figure 2.18: Lagrangian tracking of particles for the third series of experiments (particles initialised south of Kerguelen Island). (a)-(b) are the horizontal paths overlying the temporal average of temperature at 50 m depth, while (c)-(d) show the vertical displacement. The test case with initial depth at 50 m is shown. Contours in panels (a) and (b) represent the bathymetry for the first 3000 m, with an interval of 600 m.

2.5 Discussion and conclusions

We have conducted a series of experiments in the KP region of the Indian Ocean sector of the Southern Ocean, using the MIT general circulation model and examined the sensitivity of the vertical velocity to the horizontal resolution. We found clear differences in this metric, due to the development of near surface sub-mesoscale frontal structures that only the highest resolution case (KERG80) is able to resolve. Sub-mesoscale flow generates the highest magnitude vertical velocities in the upper part of the water column (down to 500 m). Moreover, the mesoscale component of w_{rms} (which is fully resolved at both resolutions) is twice the magnitude in the KERG80 case, compared with KERG20 (Fig. 2.13). We suggest that the energetic field that emerges in the sub-mesoscale-resolving case (KERG80) feeds back onto the larger scale field (w_M), transferring energy from high to low wavenumber structures (Fig. 2.8). Fig. 2.13 also shows that in both cases there are strong signatures of w_{rms} away from the surface. At depths of approximately 3000 m, the

peak in total w_{rms} and the sub-mesoscale component seem to arise from the interaction between the circulation and the deep topography east of the plateau. The continuity equation suggests we might expect a 4-fold increase of resolution to produce a 4-fold increase of w . However, the ratio between the 11-fold increase in total w_{rms} and 4-fold increase in resolution (ratio of 2.75) is greater than in previous studies. For example, Lévy et al. (2001) showed that w_{rms} increased by a factor of 1.7 for an increase in resolution of 3 times (ratio of 0.57), using an idealised configuration of an oligotrophic ocean. In the California Current system modelled by Capet et al. (2008a), the authors found that the w_{rms} increased by 15 times for a 6-fold change in resolution (ratio of 2.5); while in the model configuration of Lévy et al. (2012), representing the western sector of the North Atlantic or North Pacific Oceans, the ratio is just 0.2. We suggest that this higher ratio in our study is most likely due to the higher kinetic energy and the weaker stratification typical of the Southern Ocean. Thus, it is likely that the strong sub-mesoscale effects found in this study may extend to other parts of the Southern Ocean.

The strong vertical velocities that arise in the KER80 case show filamentary structures (Fig. 2.10). There is a strong correlation between $|\nabla_H \rho|$ and high w , as one can infer also from Fig. 2.11, which suggests the presence of a frontogenetic mechanism. Yet, we point out that this may not be the only (or even the main) mechanism present that generates high values of vertical velocity; high values of w are found also in regions of low density gradient, away from fronts (e.g. the large w found around 49.2°S of Fig. 2.11). Possible mechanisms that might contribute to the observed high vertical velocities are instabilities occurring along fronts (McWilliams and Molemaker, 2011), wind-driven pumping (Lee et al., 1994) or mixed layer instabilities (Boccaletti et al., 2007). The location of vertical circulation indicates similarities and differences between the two runs. A similar behaviour is found over the plateau, where the horizontal circulation is very weak and there is no evidence of frontal activity even in the KER80 case. Here, $w_{rms,2D}$ has low magnitude (Fig. 2.12). Most of the strong up/downwelling in the KER20 case happens in a band at latitudes north of 50°S (Fig. 2.12 a), while at the highest resolution (panel b, areas 2 and 3) strong vertical circulations are found to the east of the plateau. These two regions are areas of sub-mesoscale activity and frontogenesis, as seen in Fig. 2.10, which is a further indication of the role of sub-mesoscales and the importance of capturing their dynamics. Moreover, the influence of the meander and of the topography, which is relevant in locations of small topographic features, are only present in the KER80 case (region 2). We conclude that the different location and magnitude found at the two resolutions may have a strong influence on the vertical transport of tracers.

We found behaviour consistent with the above flow metrics in the transport of particles. The analysis of the advective transport measured by Lagrangian particle tracking confirms the sensitivity to horizontal resolution. According to the paths shown in Fig. 2.14, 2.16 and 2.18, three different regions can be identified. The first region is characterised by particles coming from south of Kerguelen Island (Fig. 2.18). In this case the particles able to pass KP and reach the eastern area of the domain originate from a shallow depth

(48 m), suggesting that here the vertical transport does not play a fundamental role in driving tracers into the plateau. At $1/20^\circ$ resolution, a small fraction of particles (less than 1%) is observed on the plateau, while in the $1/80^\circ$ case we found up to 15%. KERG20 paths are mainly trapped by the current flowing northward, while in the KERG80 case the particles spread more widely over KP, although in 100 days of integration they do not reach the area east of the plateau.

The second region comprises the meander feature and extends from north of KP (at approximately 70°E and 46°S) to the area east of the plateau. The circulation of the meander does not generate vertical displacement of the particles (black lines in Fig. 2.16) which, in the case of KERG80, may be due to weak sub-mesoscale structures. The lack of sub-mesoscales here may result from the proximity to the upstream boundary, where incoming flow is relatively laminar and sub-mesoscale instabilities are unable to form. Alternatively, the flow dynamics may simply be stabilised by strong shear within the front. Resolving this question would require additional model runs which are beyond the scope of the present paper.

Finally, a third region can be identified. This region is associated with two groups of paths. The first comprises those particles that follow the contours of the bathymetry and come from locations south of 46°S , at the longitude of 70°E . A second group is defined by the trajectories found east of KP. The first group of trajectories are not present in the KERG20 case (top panels of Fig. 2.16, which shows horizontal patterns of an ensemble of particles released at 200 m and the temporal mean of $\overline{\text{SSH}}$ contours, as represented in Fig. 2.5). We suggest that the evolution of these particular trajectories is correlated with the position of thermohaline fronts. The different circulation and thermohaline structures that arise in the two different models imply distinct impacts on the transport of particles. In the KERG20 case, the position of the northern front, indicated by $\overline{\text{SSH}}$ contours in Fig. 2.16, is shifted northward compared to KERG80 and drives the particles far from the boundaries of KP. Conversely, in the $1/80^\circ$ case the front is placed along the bathymetric contours, driving south-eastward the trajectories coming from south of 46°S . In the KERG80 case, these trajectories experience strong vertical motion due to the presence of strong small-scale filaments. The last group of paths arising in this region are those advected east of the KP, where high frontal activity is present in the KERG80 case (Fig. 2.10 b). Here, the impact of the sub-mesoscales is prominent and the particles are transported with rapid transitions upward and downward in the water column (e.g. Fig. 2.16 b). The evidence that such behaviour comes from small-scale structures may also be inferred from the comparison with the vertical structure of vertical velocity (see panels d and f of Fig. 2.10).

This study highlights the importance of resolving small-scale features in an ocean model, for a correct investigation of vertical transport and circulation. In the KP region this is fundamental if seen in the context of iron sources and transport, which consequently leads to a proper evaluation of the carbon export budget. We also suggest that the need for high horizontal resolution, such as $1/80^\circ$, may be dependent on the location. Higher resolu-

tion is required in areas such as along the eastern flank of the northern KP, or downstream of the ACC. In contrast, over the plateau the similarity in the two simulations suggests that a lower horizontal resolution may be sufficient to represent the ocean dynamics. From Fig. 2.10 it is clear that filaments are well resolved at $1/80^\circ$ resolution. Yet, experiments at higher resolution would be needed to determine whether any additional processes arising at finer scales play a significant role in vertical transport. We are presently undertaking a study aiming to couple such dynamics with bio-geochemical processes and understand the evolution of iron concentration in relation to physical structures.

Furthermore, the sensitivity of vertical transport to changes in horizontal resolution has important ramifications for modelling the ocean carbon cycle. Currently, global ocean models use horizontal resolutions that either do not, or barely, resolve mesoscale dynamics. Our results imply that such models may miss important processes that transport nutrients into the surface waters, and thus may poorly represent key processes important to carbon cycling in the upper ocean. It follows that considerable work is needed to understand and (in the absence of sub-mesoscale resolving models) better parameterise vertical fluxes or tracers due to sub-mesoscale processes.

Topographic influence on sub-mesoscale dynamics in the Southern Ocean

Abstract

Topography influences the circulation in the Southern Ocean, generating stationary meanders in the lee of topographic features, triggering hotspots of mesoscale eddy kinetic energy and modifying jets and fronts. However, the relationship between topography and sub-mesoscale flows (with length scales of order 1–10 km) has not yet been explored. The first sub-mesoscale-resolving ($1/80^\circ$ resolution) ocean model, with realistic topography of the Indian sector of the Southern Ocean, is used to investigate this interaction. The results show spatial inhomogeneity in sub-mesoscale activity that is correlated with topography. Topographic influence is primarily indirect: topography controls mesoscale flows, which in turn generate sub-mesoscale activity. Mesoscale eddy kinetic energy and strain rate can be used, to first order, to infer sub-mesoscale vertical velocity, implying a possible route to parameterise sub-mesoscale activity in coarser resolution models.

3.1 Introduction

The circulation in the Southern Ocean is characterised by the jets and eddies of the predominantly eastward Antarctic Circumpolar Current (ACC). The ACC, which encircles the Antarctic continent, is steered by topography, such that the position and structure of its jets and fronts deviate from the zonal direction, both spatially (e.g. Sokolov and Rintoul, 2009b) and temporally (Chapman and Morrow, 2014). Topography can produce quasi-stationary meanders (Naveira-Garabato et al., 2009) or Rossby waves in the lee of topographic features (e.g. Colton and Chase, 1983). It can excite hotspots of eddy kinetic energy (Thompson and Sallée, 2012) and is also involved in the generation of energetic internal tides (e.g. Park et al., 2008a) and enhancement of vertical mixing (e.g. Nikurashin et al., 2013). Thus, the Southern Ocean is a region where bottom topography directly

affects the surface flow. However, topographic effects on the sub-mesoscale structures in the Southern Ocean circulation are yet to be explored.

Sub-mesoscales are characterised by length scales of order (1-10) km, a vertical extension of few hundred meters and a lifetime of the order of several days, covering spatio-temporal scales which are difficult to observe and resolve in numerical models (Boccaletti et al., 2007; Fox-Kemper et al., 2008). Sub-mesoscale features can emerge from a range of mechanisms such as frontogenesis or frontal instabilities (e.g. Mahadevan and Tandon, 2006; Capet et al., 2008a; Thomas and Ferrari, 2008; Thomas et al., 2008) and can provide a route to dissipation, via loss of balance of geostrophic flows which yields a forward cascade of energy towards smaller scales (e.g. McWilliams et al., 2001; Molemaker et al., 2005). Furthermore, numerical studies have revealed that sub-mesoscales control vertical velocities and vertical transport (e.g. Chapter 2, Capet et al., 2008a; Lévy et al., 2001, 2012). Studies have also shown that sub-mesoscales influence the mixed-layer stratification (Lapeyre et al., 2006; Boccaletti et al., 2007; Fox-Kemper et al., 2008; Thomas and Ferrari, 2008; Mahadevan et al., 2010) and large-scale flows (Lévy et al., 2010). Typical sub-mesoscale vertical velocities are $O(100 \text{ m day}^{-1})$ in the weakly stratified, eddy-rich near-surface waters of the Southern Ocean (Chapter 2 and Phillips and Bindoff, 2014). The enhancement of vertical velocity, and hence transport, influences the carbon cycle by intensifying nutrient supply to the surface euphotic layers and consequently stimulating phytoplankton production (e.g. Klein and Lapeyre, 2009; Lévy et al., 2009). The Southern Ocean is a region of high anthropogenic carbon uptake (e.g. Khatiwala et al., 2009), where iron is a limiting nutrient (e.g. Boyd et al., 2000) and sub-mesoscale processes can enhance the supply of iron to the surface (Chapter 2). Regions of enhanced primary productivity are correlated with both strong sub-mesoscale activity and the occurrence of large sub-surface topography (Chapter 2). However, the extent to which topography might influence sub-mesoscales and their associated vertical velocities in this region has never been investigated before.

This study represents the first regional sub-mesoscale-resolving numerical model with realistic topography, which simulates the ocean circulation of the south Indian Ocean (Fig. 3.1) and examines the impact of topography on upper ocean sub-mesoscale processes. The south Indian Ocean is characterised by complex bathymetric structure, having deep ridges, notably the south-east Indian Ridge (SEIR), and a shallow plateau, the Kerguelen Plateau (KP, panel a); this complexity is responsible for deflecting and dividing the ACC, and consequently, producing an intense mesoscale eddy field. The model will be described in greater detail in section 3.2. The results will be presented in section 3.3 and conclusions in section 3.4.

3.2 Methods

Simulations are performed using the MITgem (Marshall et al., 1997) (in hydrostatic mode) with a horizontal resolution of $1/80^\circ$. These simulations are built on the sub-mesoscale-

resolving experiments described and validated in the study presented in Chapter 2, but now have a larger nested region at $1/80^\circ$ resolution. Furthermore, the present model is zonally-reentrant, located in the region 57°E – 129°E , 54°S – 40.5°S , which gives a size of 5760 points in longitude, 1080 in latitude and 150 vertical levels, making this the largest sub-mesoscale-resolving model we know of. The model uses partial cells for the topography and has a vertical resolution which increases from 10 m (close to the surface) to 50 m at depth. The maximum depth is 5000 m. The model is nested within a coarser resolution configuration (the $1/20^\circ$ resolution experiment discussed in Chapter 2 and open boundary conditions are used on the northern and southern boundaries, where daily zonal and meridional velocities, temperature, salinity and sea surface height are prescribed by the $1/20^\circ$ run. The $1/80^\circ$ model initial condition is interpolated from the equilibrated $1/20^\circ$ run. The model is forced and relaxed to temporally constant fields. All other parameters are as specified in 2.2. Statistical equilibrium is reached after 800 days, a further 400 days are run and analyses are performed over the last 200 days of simulation.

3.3 Results

In the following sub-sections the modelled ocean dynamics are analysed, with a particular emphasis on the local vertical motion as a proxy for sub-mesoscale activity and its relation to realistic topography (considering its variation, depth and roughness). Our analysis is mostly focused on the upper ocean vertical velocity w , as this is most relevant to nutrient transport into the euphotic zone and is better constrained than w near the bottom.

Temporal means are 200-day averages and are denoted by an overbar ($\bar{\cdot}$). Fluctuations (\cdot') are defined as the departure from the time mean, while $\langle \cdot \rangle$ indicates spatial averages. The domain used for the analysis includes the entire longitudinal extension of the model, but a smaller latitude range (53°S – 41.5°S) to avoid unrealistic boundary effects. Spatial filters are used to decompose the fluctuating component of the flow into mesoscale and sub-mesoscale components. The mesoscale component, indicated by the subscript “M”, has been obtained by applying a low-pass filter (a running mean over $1/5^\circ$, comparable to the first baroclinic Rossby radius at these latitudes (Chelton et al., 1998)) to the fluctuations, at each instant, and includes all scales from mesoscale upwards. We define the sub-mesoscales (“S”) as the residual between the fluctuations and “M”. This definition of sub-mesoscales will capture the frontal structures of interest, albeit with contamination from other dynamics occurring at the same length scale (such as internal waves and variability within a mesoscale eddy).

3.3.1 Frontal structures

Topography constrains the circulation in this region and the model captures its main features (see Chapter 2 and Park et al., 2008b, for a comparison). In particular, the simulation shows that the ACC interacts with the Kerguelen Plateau and is divided into two main streams, one flowing north of the plateau and one through the Fawn Trough

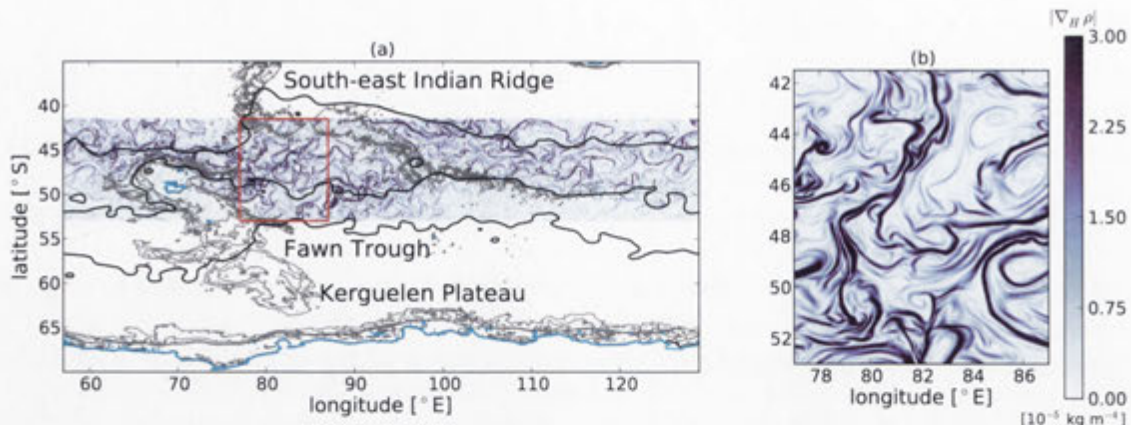


Figure 3.1: (a) The colours show a snapshot of surface density gradients $|\nabla_H \rho|$ over the entire $1/80^\circ$ domain, nested within the $1/20^\circ$ domain (the larger white area). Black contours are 200-day averages of sea surface height from the $1/20^\circ$ model (indicative values are, from the southernmost contour: -0.8 m, -0.4 m and 0.5 m), grey contours are isobaths for the first 3000 m, with 600 m steps, and land contours are in cyan. The red box in panel a defines the boundaries of the sub-region illustrated in panel b.

(shown by sea surface height contours from the $1/20^\circ$ resolution simulation in Fig. 3.1a). The northern stream generates a meander on the north-east side of KP, a well observed feature of this region (Naveira-Garabato et al., 2009; Phillips and Bindoff, 2014). Furthermore, the circulation through the Fawn Trough (just partially included in the $1/80^\circ$ model) interacts with the southward stream that comes from north of the plateau.

The horizontal density gradient $|\nabla_H \rho|$ (Fig. 3.1a,b) is a good indicator of sub-mesoscale structures. These structures are non-uniformly distributed over the domain, suggesting that their location might be constrained by the topography. Strong frontal activity is found downstream of KP (Fig. 3.1b shows a detailed closeup of $|\nabla_H \rho|$ in this location) and east of SEIR, with decay further towards the east. It is well-known that sub-mesoscale frontal structures are associated with large vertical velocities (e.g. Chapter 2, Capet et al., 2008a; Lévy et al., 2001), which might enhance vertical transport of nutrients from depth, through the mixed layer (e.g. Lévy et al., 2001). Some of the processes that can contribute to vertical motion are discussed by Mahadevan and Tandon (2006). Although an exhaustive study of these and other processes in this model is beyond the scope of this paper, we highlight the importance of more detailed analyses for future developments.

The vertical motion at a depth of 400 m is chosen as a proxy for near-surface sub-mesoscale activity. The 400 m fixed depth has been selected in order to focus on the vertical velocities near the base of the deepest mixed layers, where they can have a significant implication over nutrient supply. Fig. 3.2a shows the temporal average of the magnitude of the sub-mesoscale vertical velocity, $|\overline{w_S}|$, at this depth. The striking feature in this figure is the inhomogeneity, or patchiness, of $|\overline{w_S}|$. The patchiness is persistent in time: 100-day averages of $|\overline{w_S}|$, computed over different time periods, show consistent patterns of intensity (not shown). Figure 3.2a indicates that large $|\overline{w_S}|$ are predominantly

concentrated east of KP and east of SEIR, corresponding to locations of filamentary structures (Fig. 3.1a). Investigating the origin of such patchiness is the aim of the present work. An analysis of the possible causes follows.

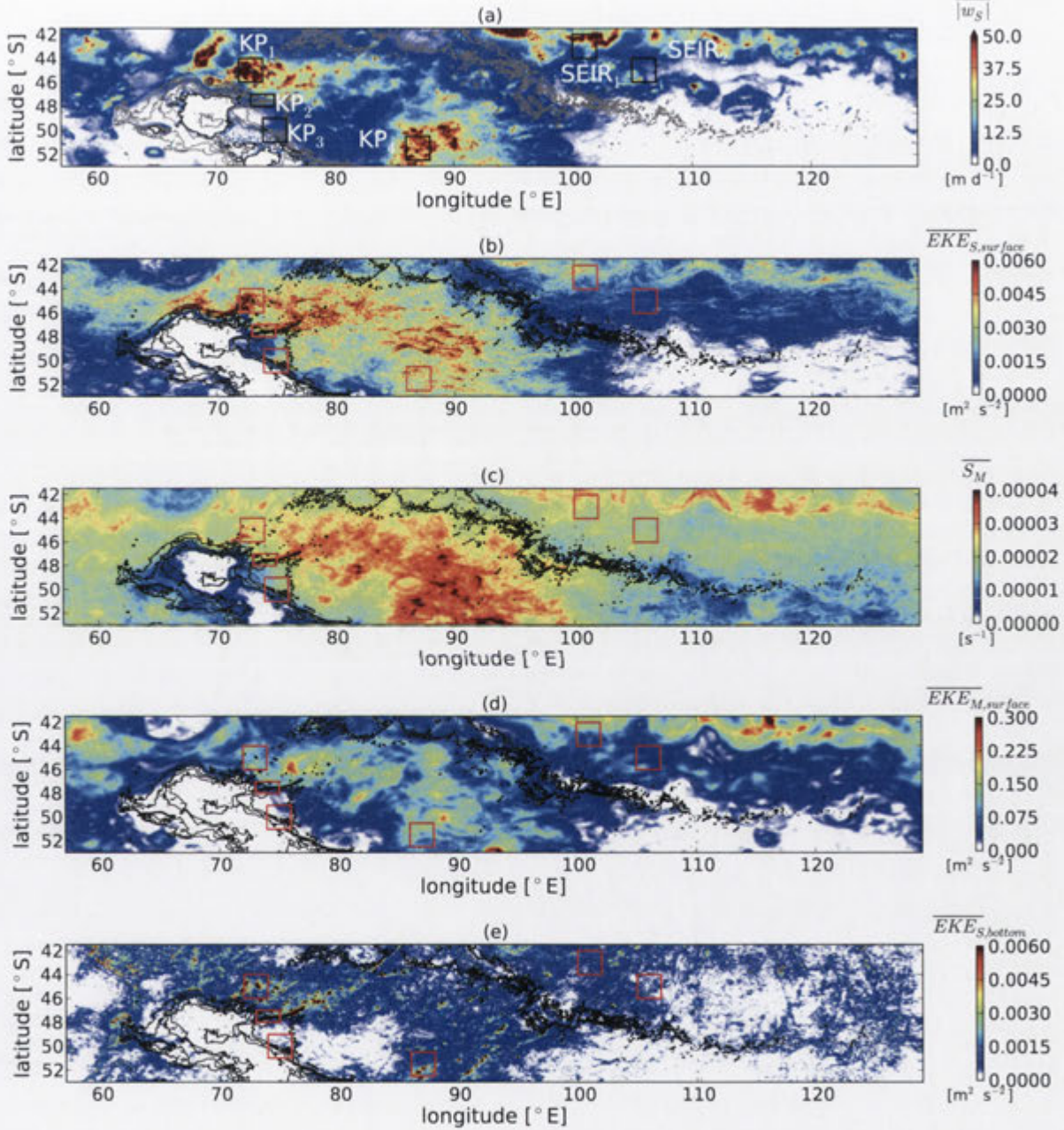


Figure 3.2: 200-day temporal averages of (a) magnitude of sub-mesoscale vertical velocity at 400 m (colour scale is saturated), (b) surface sub-mesoscale eddy kinetic energy, (c) surface mesoscale strain rate, (d) surface mesoscale eddy kinetic energy and (e) bottom sub-mesoscale eddy kinetic energy. Boxes indicate sub-regions for the analysis shown in Fig. 3.3. Grey (black) contours in panel a (b-e) are topographic contours for the first 3000 m, with a step of 600 m (maximum depth is 5000 m). The black contour in panel a is the 400 m isobath.

3.3.2 Causes of patchiness

In the following sub-sections, different mechanisms that aim to describe the patchiness highlighted in Fig. 3.2a will be investigated by using horizontal sections of the 200-day mean of mesoscale ($\overline{EKE_M} = \overline{(u_M^2 + v_M^2)}/2$) and sub-mesoscale ($\overline{EKE_S} = \overline{(u_S^2 + v_S^2)}/2$) eddy kinetic energy (Fig. 3.2b, d and e) and mesoscale strain rate ($\overline{S_M} = \sqrt{((u_M)_x - (v_M)_y)^2 + ((v_M)_x + (u_M)_y)^2}$), in panel c. Note that $\overline{EKE_M}$, purely obtained from the mesoscale field, does not consider cross-scale components. The vertical structure of key parameters is investigated via spatial and temporal averages over specific regions (indicated by the boxes in Fig. 3.2) as shown in Fig. 3.3, selected in order to consider different flow features and topographic depths. In each region we show vertical profiles of root mean square vertical velocity, decomposed into mesoscale ($RMS(w_M) = \sqrt{\langle w_M^2 \rangle}$, magenta lines) and sub-mesoscale ($RMS(w_S) = \sqrt{\langle w_S^2 \rangle}$, in black) components. The depth distribution of the topography in each box is illustrated by a histogram (red bars). Furthermore, indicative snapshots of vertical sections of w_M and w_S (Fig. 3.4) will be used as examples to depict properties of the vertical motion.

Direct generation

One plausible mechanism for the observed patchiness in the vertical motion is the direct interaction of the mean flow \mathbf{u} with topography H , i.e. vertical velocity due to bottom-generated vertical motion $w_{bottom} = -\mathbf{u}_{bottom} \cdot \nabla H$. We found that the near-surface patchiness of $\overline{|w_S|}$ does not correlate to the gradient of the topography (not shown), however ∇H presents non-negligible values in localised regions, where it can contribute to the magnitude of the near-surface vertical velocity. For example, regions such as KP₂ and KP₃, whose vertical profiles are shown in Fig. 3.3b,c, represent areas where the influence of the topography extends throughout the water column, as indicated by depth histograms. This connection between the near-surface sub-mesoscale vertical velocity and topography in KP₃ is evident in the snapshot of w_S in Fig. 3.4b. However, Fig. 3.2a shows that hotspots of $\overline{|w_S|}$ at 400 m depth are distant from the 400 m depth contour (black line in figure), indicating that this mechanism is unlikely to be the main driver for the patchiness in the sub-mesoscale vertical velocities. In addition, Fig. 3.2e, which shows the near-bottom $\overline{EKE_S}$ (computed considering velocities three grid points above the bottom), illustrates that topography directly influences sub-mesoscales most strongly at depths far below 400 m. Thus, we conclude that the main patches of strong sub-mesoscale activity at 400 m are not due to direct topographic interaction.

Internal waves

The model resolves the internal wave frequency range, having a time step of 60 seconds, but does not fully resolve the spatial scales of internal waves (and hence their associated energy). Nevertheless, some of the signal in $\overline{|w_S|}$ may be due to internal waves rather than sub-mesoscale flow; only the latter is of interest in this study, as advection by internal

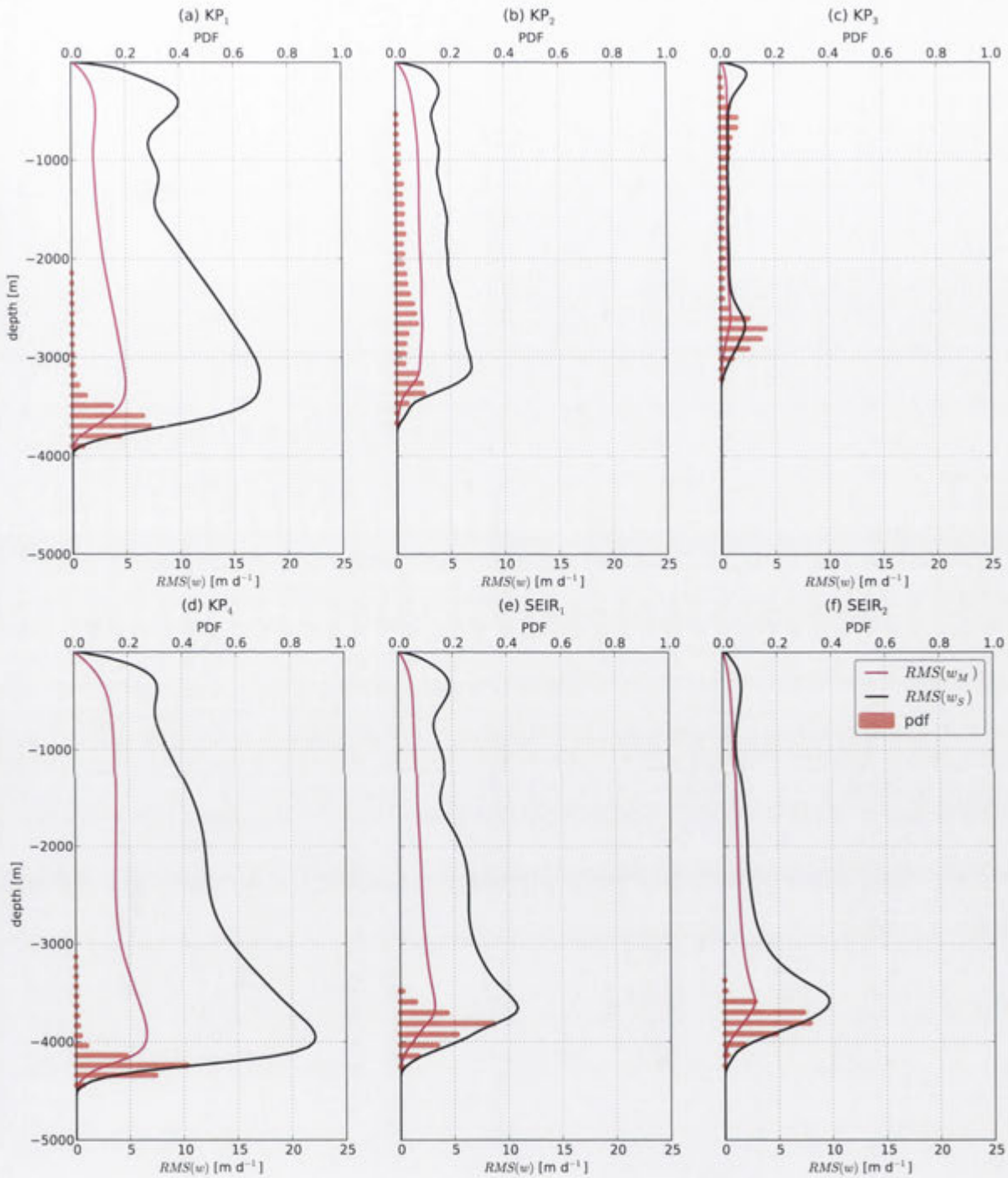


Figure 3.3: Vertical profiles of 200-day average of spatial root mean square mesoscale (magenta) and sub-mesoscale (black) vertical velocity for the boxes in Fig. 3.2 (x-axis indicates values in $[\text{m d}^{-1}]$); histograms show the probability density function of topographic depth.

waves will not produce significant net vertical nutrient transport. In particular, internal lee waves, generated by the interaction of the flow with rough topography, could be a component of the $\overline{|w_S|}$ signal at 400 m, perhaps contributing to its patchiness. We observe that the bottom $\overline{EKE_S}$ (Fig. 3.2e) is largest in deep regions of rough topography, creating

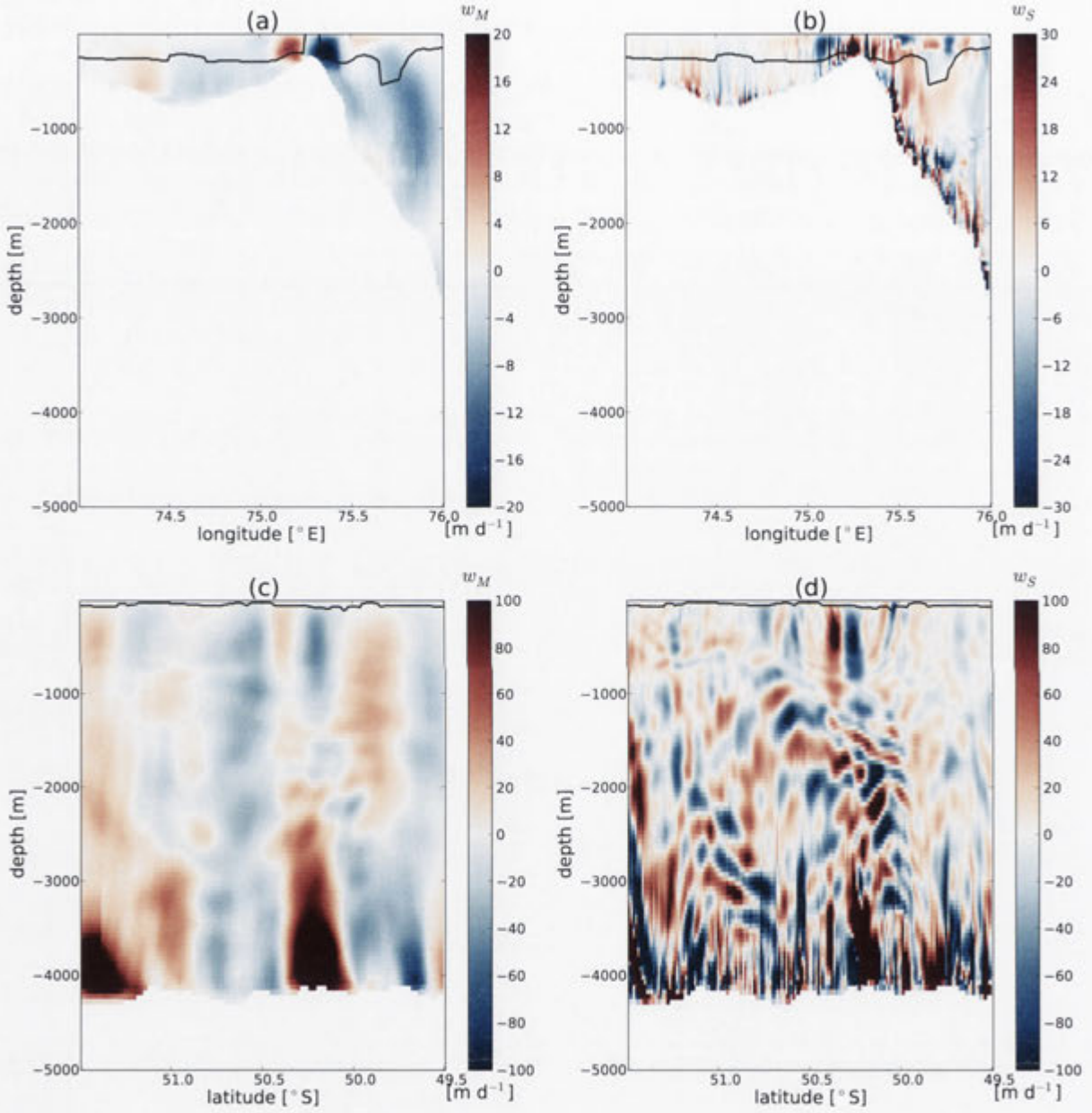


Figure 3.4: (a,b) Snapshot vertical sections at approximately 51°S (in KP₃ region) and (c,d) at 88°E (in KP₄). Panels a and c show mesoscale components of vertical velocity, while b and d show the sub-mesoscale components. The black lines represent the mixed layer depth, computed with a temperature criterion of $\Delta T = 0.05^\circ\text{C}$.

the maximum values of $RMS(w_S)$ at depth (Fig. 3.3) consistent with the generation of internal lee waves. However, strong $\overline{EKE_S}$ at the surface is broadly distributed, rather than being concentrated over regions of rough topography. Thus, further examination of the vertical extent of lee wave propagation is required.

The profiles of $RMS(w_S)$ in KP_1 , KP_4 , $SEIR_1$ and $SEIR_2$ (Fig. 3.3) show that the deep enhancement of vertical velocity decays with height, away from topography. However, the near-surface maxima in $RMS(w_S)$ stand out above this decay rate. Furthermore, the near-surface w_S signal in Fig. 3.4d, which has a vertical phase line, is decoupled from the signal near the bottom which has phase lines whose tilt is consistent with the dispersion relation for linear lee waves.

A movie of hourly-sampled vertical velocity over 30 days is available in the Auxiliary Material. The movie is composed of horizontal and vertical sections of unfiltered w at 400 m and 47°S, respectively, and partly includes the KP_1 and KP_2 boxes. It shows the occurrence of surface generated upper ocean structures (e.g. at 47°S, 82.5°E–84.5°E, from day 13 to 16, or 47°S, 87°E–89°E, from day 14 to 18), lee waves (e.g. around 47°S, 77°E, from day 6 to 10) and bottom-generated internal waves propagating to the upper ocean (e.g. around 47°S, 87°E in much of the movie). These waves propagating from the bottom to the surface contribute to the upper-ocean signal. However, it is clear from the vertical slice in the movie that the internal wave signal is mostly confined near the bottom and only occasionally reaches 400 m, except in a few isolated locations. We have investigated the temporal spectrum of w in a location around 47°S, 77°E at 400 m and found that its dominant frequencies are one order of magnitude lower than the Coriolis frequency. This indicates that the signal variability at 400 m is not dominated by propagating internal wave activity.

Despite this result, we cannot exclude a contamination from bottom-generated internal waves in the inhomogeneity of near-surface vertical velocities in Fig. 3.2, as stationary lee waves cannot be distinguished in such analysis. However, the large upper-ocean $RMS(w_S)$ peak found in these regions (Fig. 3.3) is a strong indication that internal wave activity cannot be the only component causing those large vertical velocities; sub-mesoscale processes must also contribute. In addition, $\overline{EKE_S}$ (Fig. 3.2b) is larger and more extensive than the near-bottom $\overline{EKE_S}$ (panel e), as expected from a near-surface source. We conclude that internal waves can affect the upper-ocean $\overline{w_S}$, but cannot explain its patchiness.

Sub-mesoscale flow

It has been shown above that the patchiness of vertical velocities is not directly generated by topography, but cannot exclude an internal wave signal. Our results suggest that the remaining part of the inhomogeneity is likely to be due to an indirect influence of the topography, by controlling the mesoscale eddy field and triggering a turbulent cascade of energy toward the smaller scales. Damerell et al. (2013) and Chapter 2 showed that the mesoscale meandering observed in the KP region, and its associated eddy kinetic energy, resulted from the interaction of the mean flow with the topography of KP and

the consequent steering of the large-scale flow. The comparison of the surface $\overline{EKE_S}$ in Fig. 3.2b with the mesoscale strain rate in panel c and the surface $\overline{EKE_M}$ in panel d shows a strong correlation between $\overline{EKE_{S,surface}}$ and the strain rate, suggesting that the underlying route transferring energy from mesoscales to sub-mesoscales occurs via straining of the mesoscale field (e.g. Hoskins and Bretherton, 1972). The sub-mesoscale eddy kinetic energy is aligned with patterns of $\overline{|w_S|}$. The correlation is sufficiently strong to propose that the patchiness in $\overline{|w_S|}$ is likely to be indirectly generated (at least in part) by the topographic influence on the mesoscale (and larger) flow. In the movie (Auxiliary Material) we see clear examples (in both the horizontal and vertical slice) of sub-mesoscale filaments being stretched and sharpened by mesoscale strain, leading to strong vertical motion just below the mixed layer and extending to around 1000 m depth (e.g. at 47°S, 84°E, from day 11 to 18). In most locations the w signal at 400 m largely originates in the surface region and is uncorrelated with the deeper variability.

Regions such as KP_1 , KP_4 , $SEIR_1$ and $SEIR_2$ are representative of the above proposed mechanism. Downstream of KP , the sub-mesoscale activity is stronger than in the area east of $SEIR$: this feature is also well reflected in the profiles of $RMS(w_S)$ (Fig. 3.3). The vertical extent of near-surface sub-mesoscale vertical velocities stretches well beyond the mixed layer depth (as the example in Fig. 3.4d illustrates), consistent with previous studies (e.g. Chapter 2, Lapeyre et al., 2006; Klein et al., 2008). This vertical extent might reflect an ageostrophic secondary circulation developing consequently to the strengthening of density fronts, due to mesoscale straining (Lapeyre et al., 2006). In $SEIR_1$ and $SEIR_2$ there is a strong correlation between spatial patterns of $\overline{EKE_S}$ and $\overline{S_M}$ and the magnitude of $\overline{|w_S|}$ (Fig. 3.2). However, the correlation is imperfect, reflecting the complexity of this flow. For example, KP_1 has a smaller strain rate than KP_4 , but nevertheless a comparable or larger $\overline{|w_S|}$ at 400 m. Strong lee waves (visible in the movie) may contribute to the anomalously large $\overline{|w_S|}$ at KP_1 .

We have analysed other regions in the model, whose data are not shown in the present paper for brevity, and which confirm the tendency described above. We conclude that, despite the imperfect correlation between mesoscale strain rate and sub-mesoscale vertical velocities, it is likely that the indirect generation via mesoscale strain is a major mechanism for the generation of the observed sub-mesoscale hotspots.

3.3.3 A proxy for sub-mesoscales

The significance of sub-mesoscale processes has been widely asserted (e.g. Chapter 2, Lévy et al., 2001; Lapeyre et al., 2006; Mahadevan and Tandon, 2006; Klein et al., 2008; Capet et al., 2008a), motivating the need to understand their dynamics and parameterise their effect in global ocean models (Boccaletti et al., 2007; Fox-Kemper et al., 2008). Eddy kinetic energy and strain rate provide evidence that the patchiness observed in the sub-mesoscale vertical motion is likely to be indirectly induced by topography via its influence on the mesoscale flow.

Further support for this interpretation is provided by Fig. 3.5, which shows the cor-

relation of sub-mesoscale vertical velocities with mesoscale eddy kinetic energy (panel a) and strain rate (panel b). For this analysis we have divided the domain into 216 boxes, each $2^\circ \times 2^\circ$. Temporal (200-day) and horizontal spatial averages are computed over each box. Mesoscale quantities, $\langle \overline{EKE_M} \rangle$ and $\langle \overline{S_M} \rangle$, are estimated at the surface, while sub-mesoscale vertical velocities are also vertically averaged over the top 400 m. The standard deviation, indicated by error bars, shows the fluctuation in space and time of $\overline{|w_S|}$ within each box. The scatter in the points may indicate the occurrence of a range of sub-mesoscale generation mechanisms, such as direct or wave-mediated topographic interaction. However, both the mesoscale eddy kinetic energy and the strain rate have a significant correlation with the vertical motion: we found a correlation coefficient r of 0.79 for $\langle \overline{EKE_M} \rangle$ and $r = 0.82$ for $\langle \overline{S_M} \rangle$. These strong correlations with the near-surface sub-mesoscale vertical velocities suggest a possible parameterisation of these fields in models with coarser resolution.

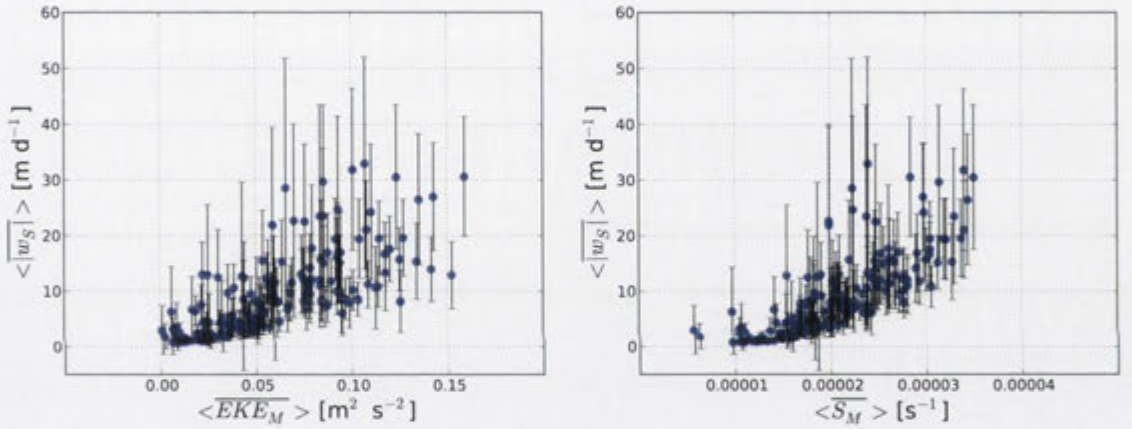


Figure 3.5: Vertical velocity dependence on mesoscale (a) surface eddy kinetic energy and (b) surface strain rate. Fields are 200-day and $2^\circ \times 2^\circ$ averages (vertical velocity is also averaged over the top 400 m) and the standard deviation computed for each box (216 boxes in total) is illustrated by the vertical bars.

As a comparison with the existing parameterisation of Fox-Kemper et al. (2008), we have investigated the correlation of vertical velocities with the horizontal gradient of mesoscale buoyancy and with the mixed layer depth (not shown). We have found a strong correlation ($r = 0.77$) of $\langle \overline{|w_S|} \rangle$ with the horizontal gradient of mesoscale buoyancy, but not with the mixed layer depth. A more detailed analysis would be required in order to investigate the implications of this result, however this is beyond the focus of the present work.

3.4 Conclusions

The model shows that in the south Indian Ocean the inhomogeneity in sub-mesoscale activity primarily occurs through indirect effects of the topography. From the interaction of

the large-scale flow with the topography, meanders and eddies develop and subsequently destabilise, transferring energy to smaller scales. Internal wave activity and direct generation of sub-mesoscale flows by the topography can be significant in specific regions, but these mechanisms are less widespread. Finally, we conclude that the correlation between sub-mesoscale activity and mesoscale strain, which is likely driven by frontogenesis (Hoskins and Bretherton, 1972), suggests a possible route to parameterise sub-mesoscale vertical velocities.

Quantifying the influence of sub-mesoscale dynamics on the supply of iron to Southern Ocean phytoplankton blooms

Abstract

Iron limits the phytoplankton growth in the Southern Ocean, a high nutrient, low chlorophyll environment. Episodes of natural iron fertilisation are pivotal to triggering phytoplankton blooms in the Southern Ocean, the Kerguelen Plateau bloom being one prominent example. Numerous studies have targeted the physical mechanisms responsible for supplying iron to the euphotic zone in the Kerguelen Plateau region and hence triggering a phytoplankton bloom. However, most studies have omitted a particular class of small-scale flows (known as sub-mesoscales) to the supply of iron. With a scale of order 10 km, sub-mesoscale filaments and fronts can dramatically increase vertical velocities and iron transport.

Here, an innovative technique is developed for the study of iron supply, that is built on Lagrangian analysis of numerical model outputs. We use this technique to contrast the contribution of mesoscale- ($1/20^\circ$ resolution) and sub-mesoscale-resolving models ($1/80^\circ$ resolution). We first advect Lagrangian particles using three dimensional velocity fields from the numerical simulations, then compute iron concentration along these Lagrangian trajectories. This technique allows us to investigate the sensitivity of iron supply to the horizontal resolution and shows a clear enhancement of iron fluxes, by a factor of 2, with the resolution. Thus, we infer that the vertical motion induced by the sub-mesoscales represents a previously neglected process to drive iron into the euphotic waters of the Kerguelen Plateau.

4.1 Introduction

The Southern Ocean has a profound influence on the past, present (e.g. Mayewski et al., 2009) and future (e.g. Takahashi et al., 2012) climate system. In this region, energetic mesoscale eddies and jets of the Antarctic Circumpolar Current (ACC) act to redistribute heat and mix water properties between the Atlantic, Pacific and Indian ocean basins. Furthermore, the Southern Ocean is the nexus of the meridional overturning circulation, where dense waters originating from the North Atlantic upwell and split into two directions: northward, where they become fresher and warmer and are subducted again forming the Antarctic Intermediate Water, or southward where their increase in density drives the formation and sinking of the world's densest water, Antarctic Bottom Water (e.g. Marshall and Speer, 2012; Talley, 2013). The Southern Ocean, thereby, helps to drive the global ocean circulation, and stores and recirculates heat, carbon and other gases, such as oxygen, exchanged with the atmosphere.

The Southern Ocean accounts for a substantial portion of the global sequestration of anthropogenic carbon dioxide (e.g. Khatiwala et al. (2009) estimated that the Southern Ocean contributed for over 40% of the oceanic uptake of anthropogenic CO₂ in 2008). The Southern Ocean is also important to the global carbon cycle and it is implicated in the large glacial to interglacial changes in atmospheric CO₂ (Sigman et al., 2010). Several processes impact the carbon cycle in the oceans, such as the biological and solubility pumps (e.g. Ducklow et al., 2001), as well as physical mechanisms active at regional scales such as upwelling and subduction (e.g. Marshall and Speer, 2012). In light of the Southern Ocean's primary role in influencing the carbon cycle, precise quantification of the individual processes that control carbon cycling in this region is critical for understanding and predicting our future climate.

Phytoplankton production is one process that has a direct impact over the export of carbon. However, in much of the Southern Ocean the phytoplankton activity is limited by the availability of iron (Boyd et al., 2000; Coale et al., 2004; de Baar et al., 2005). Martin (1990) hypothesised that iron can stimulate phytoplankton productivity and thereby contribute to a drawdown of atmospheric CO₂. Understanding the potential iron sources and physical mechanisms that can supply iron into the surface waters (and trigger a phytoplankton response) is therefore a prerequisite to understanding Southern Ocean phytoplankton blooms. One of the largest regular phytoplankton blooms occurs in the Kerguelen Plateau (KP) region of the Southern Ocean.

Recent studies have identified several physical mechanisms controlling dissolved iron delivery during the growth and evolution of the KP phytoplankton bloom. Iron input can come from aeolian dust deposition (Bucciarelli et al., 2001; Chever et al., 2010) or sediments, which can enter KP sunlit waters transported by the stirring action of eddies (Abraham et al., 2000; d'Ovidio et al., 2013), turbulent mixing due to tides and internal waves (Park et al., 2008a), wind-induced upwelling (Gille et al., 2014) or lateral advection (van Beek et al., 2008; Mongin et al., 2009) and mixing (Maraldi et al., 2009). However, calculations of the quantity of iron required to sustain the Kerguelen Plateau bloom

indicate that additional iron is required (Bowie et al., 2014).

It was recently proposed that sub-mesoscale dynamics (defined by a length scale less than 10 km and Rossby number greater than 1) could be an important supply of iron to the KP region (Chapter 2). The rich mesoscale eddy field (with length scales of $O(100\text{ km})$) gives rise to strong sub-mesoscale velocities in the Kerguelen Plateau region (Chapter 3) and which can dramatically increase vertical velocities and transport of particles (Chapter 2). Lévy et al. (2001) showed that sub-mesoscales can increase the nutrient vertical transport and consequently influence biological cycles in other parts of the ocean. In this study we aim to quantify the effect of sub-mesoscales on iron transport in relation to other processes, especially when compared to larger mesoscale flows.

Our approach is a numerical study of the dissolved iron concentration (DFe) and is based on the development of a mathematical model ($FeRRO_{SO}$), that associates the computation of DFe to Lagrangian particles, advected by a series of three dimensional high-resolution models of the Kerguelen Plateau region. The Lagrangian framework is reported in section 4.2, while $FeRRO_{SO}$ is described in section 4.3). We perform a sensitivity analysis on $FeRRO_{SO}$ parameters (subsection 4.3.2) and investigate iron fluxes in mesoscale- and sub-mesoscale-resolving models (section 4.4). The implications of these calculations are discussed in section 4.5.

4.2 Sub-mesoscale impact on Lagrangian paths

Numerical simulations of the ocean circulation around the Kerguelen Plateau have been run using the MITgcm of Marshall et al. (1997), forced and relaxed by temporally constant fields. The model is implemented at two horizontal resolutions: first, at $1/20^\circ$ resolution in order to capture the circulation with scales down to the mesoscales, and second, at $1/80^\circ$ resolution to explicitly include sub-mesoscales. Implementation, discussion and assessment of these experiments have been outlined in Chapter 2 and 3. We here aim to highlight the rich sub-mesoscale dynamics that the $1/80^\circ$ resolution model captures, and the approach that we have developed to investigate the impact of sub-mesoscales on the vertical motion. In particular, a Lagrangian particle-tracking framework has been implemented, from which a set of experiments (reported below) is used as foundation for the development of $FeRRO_{SO}$.

4.2.1 Lagrangian trajectories

The Connectivity Modelling System (CMS) of Paris et al. (2013) is used off-line, to integrate Lagrangian particle trajectories using velocity fields from the numerical simulations. The procedure followed is to seed regions of interest with a constant density of Lagrangian particles. The CMS software is then used to integrate the trajectory of these particles backwards in time. Given a sufficiently large number of particles, this technique informs us of both the sources of water and the path followed.

Particles are released in two different regions (boxes R_1 and R_2 in Fig. 4.1) chosen

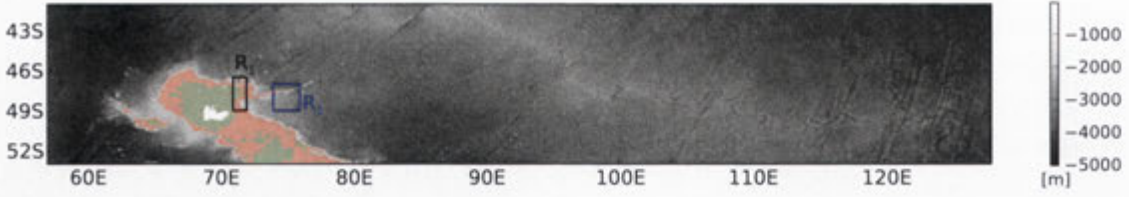


Figure 4.1: Kerguelen Plateau bathymetry. In green the area *ON* the plateau (defined by the 500 m isobath); in red is the transition zone, between the *ON* and *OFF* plateau area (grey shading, delimited by the 1500 m isobaths). The black and blue boxes delineate the particle release locations.

in order to isolate locations of diverse phytoplankton activity and with differing intensity of sub-mesoscale flows. A plot of chlorophyll concentration in this region can be found in Park et al. (2014) (Fig. 6), while the sub-mesoscale activity can be seen in 2.10b. R_1 is located at 71°E – 72°E , 46.5°S – 49°S , designed to capture the bloom observed near the plateau, which occurs in a region of relatively weak sub-mesoscale activity. Region R_2 , located at 74°E – 76°E , 47°S – 49°S , encompasses a region of an observed phytoplankton bloom downstream of the plateau, where intense sub-mesoscales dominate the circulation.

A total of 2142 and 3362 particles have been initialised in regions R_1 and R_2 respectively, over 2 different depths (75 m and 200 m), and equally spaced in the longitudinal and latitudinal directions, with a step of 0.05° in both directions. The release depths have been chosen in order to capture levels below and within the spatial mean mixed layer depth of that area (we estimated maximum spatial means of mixed layer depths of approximately 84 m and 113 m for the three regions in the $1/20^\circ$ model and 131 m and 152 m in the $1/80^\circ$ areas, at the time of release). It is at the deeper level, i.e. at 200 m, that the quantification of the vertical advective flux of iron is significant for the investigation of the meso- and sub-mesoscale flows. In order to explore how meso- and sub-mesoscales influence the transport of water particles, no turbulent scheme has been employed; Lagrangian particles are purely advected by daily snapshots of zonal, meridional and vertical velocity dataset. A timestep of 60 seconds is implemented over a maximum integration time of 200 days, with outputs saved every 12 hours.

We define two water sources: *ON* and *OFF* the plateau. We base this distinction on the observational study of Blain et al. (2007), in which their stations *ON* the plateau were those in water depth of less than 500 m and *OFF* the plateau included those with a depth exceeding 1500 m. Thus, we identify the 500 m isobath as the limit for our *ON* area (green region in Fig. 4.1). Beyond this, an *OFF* plateau region is defined, which includes a transition zone between the *ON* area and the 1500 m contour (red shaded area in Fig. 4.1).

At $1/20^\circ$ resolution, we found that waters originating from the plateau (*ON*) account for the 59% and 22% in case of R_1 and R_2 , respectively. At $1/80^\circ$ resolution, the *ON* particles account for the 75% (R_1) and 32% (R_2). This result highlights, first, that water sources are sensitive to the horizontal resolution and, second, that water sources differ

between the two regions under analysis.

Figure 4.2 shows several selected example Lagrangian trajectories for the $1/80^\circ$ resolution experiment (plotted are daily particle positions color-coded depending on the daily particle depth). Release and source positions of the particles are shown by circular and triangular markers, respectively (recalling that trajectories are integrated backwards in time). We highlight a range of different trajectories, including those crossing the plateau either north or south of the Kerguelen Island, as reported in Chapter 2, and deep trajectories coming from the south east region of the plateau (Fig. 4.2), likely captured by the deep western boundary current on the east flank of the plateau (McCartney and Donohue, 2007).

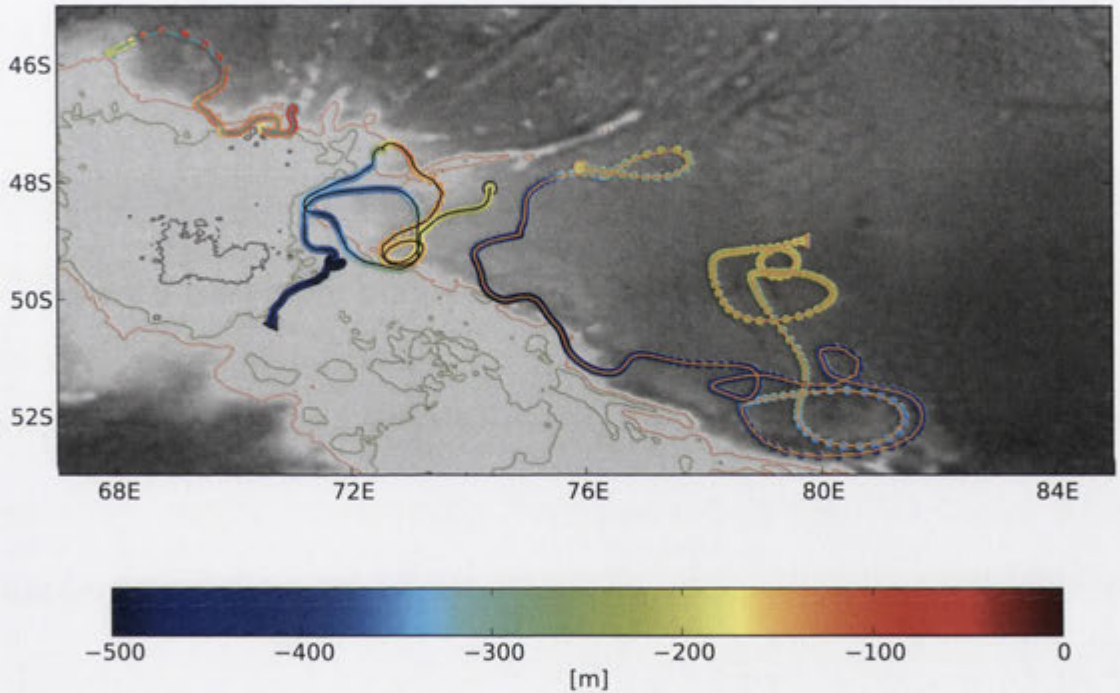


Figure 4.2: Examples of Lagrangian trajectories, daily sampled, color-coded depending on the daily depth, for the $1/80^\circ$ resolution experiment. Circular markers indicate the particle release location, while triangular the source position. Topography is shaded in grey. Green contours indicate the boundaries of the *ON* source, while red the *OFF* plateau source.

4.2.2 Depth distribution of tracked particles

The particle distribution in the water column, computed as a probability density function (PDF) of the source particle as a function of depth, over each region, is shown in Fig. 4.3. The PDFs are computed for the total number of particles released at both 75 m and 200 m and show the distribution for *ON* (dashed lines), *OFF* (dotted) and all particles (solid) for each region. The $1/20^\circ$ resolution profiles are shown in red, while the $1/80^\circ$ are in black. For each region, the PDF profiles are normalised to $\sum_{i=1}^N T_i$, where N refers to either the total number of *ON* or *OFF* particles, or to the total number of particles released

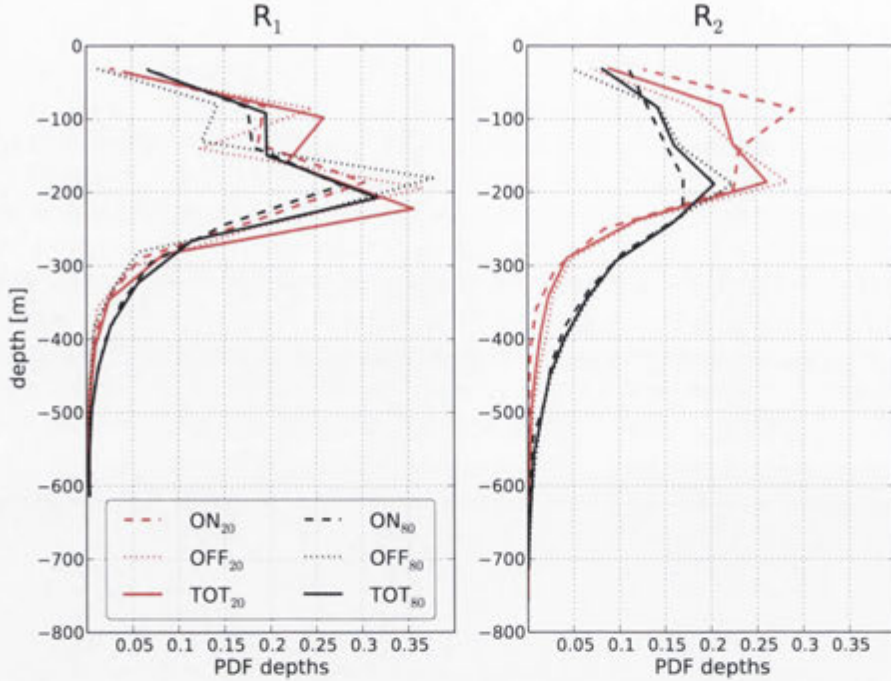


Figure 4.3: Probability density function of particle depth for the two regions of investigation, R_1 and R_2 . Colors indicate the different resolution (red is for the $1/20^\circ$ and black is for the $1/80^\circ$). Dashed lines are the profiles for the ON particles, dotted for the OFF and solid for the total amount of particles (TOT).

in the region. T_i indicates the lifespan of the particle i , which can be less than the total integration time of 200 days, as the particle can exit the model domain or reach land in less than 200 days. The figure shows that the impact of the horizontal resolution on the PDF profiles for the two regions of interest depends on the location of analysis and on the range of depths considered. For region R_1 , the PDF profiles are not significantly influenced by resolution. Furthermore, the mean depth of the total PDF profiles in R_1 (approximately 130 m at $1/20^\circ$ resolution and 171 m at $1/80^\circ$) are shallower than the mean depth in R_2 (approximately 163 m at $1/20^\circ$ and 191 m at $1/80^\circ$), suggesting that R_1 is a region with a higher probability of surface-sourced particles. On the contrary, there is a larger number of deep-sourced particles in R_2 , which increases with the resolution. The larger number of particles found at depths below 300 m in R_2 is not surprising when considering that the deep reaching sub-mesoscale activity present in this region cycles the water as deep as 1000 m (Chapter 2), and this is much stronger in the $1/80^\circ$ simulation than in the $1/20^\circ$.

4.3 Methods

We here describe the off-line model that has been implemented in order to compute the evolution of iron concentration on the trajectories of Lagrangian particles. Note that Lagrangian trajectories have been integrated backward in time, while the evaluation of iron concentration follows a forward in time integration, from the final position reached

by the particles to their initial.

4.3.1 FeRRO_{SO}

Iron concentration is computed by implementing a decay/replenishment model. This methodology has the advantage of being simple and easy to modify and discriminate the role of specific physical processes. Input of the model is a 3D position as a function of time. At each instant, FeRRO_{SO} estimates the concentration of iron for the i -th particle (DFe_i) by solving the following equation:

$$D\dot{F}e_i = -\lambda(z_i)DFe_i - f(z_i)(DFe_i - \langle DFe \rangle_i), \quad (4.1)$$

where $(\dot{})$ represents the time derivative. Parameters of (4.1) represent decay (λ) and replenishment (f) of iron. Replenishment occurs via restoring towards $\langle DFe \rangle_i$, a 3D function describing the temporal mean concentration of iron taken from climatology. Each of these terms are discussed in the following subsections. Three layers are identified in the model, with differing behaviour. These layers are depicted by the depths $z_1 = -100$ m and $z_2 = -200$ m.

Decay rate

In the upper region ($z_i \geq z_1$) DFe_i is constrained to decay with rate $\lambda(z)$. This decay rate λ (given in day^{-1}) depends exponentially on depth and is used to parameterise the loss of iron due to biological uptake in the euphotic layer, by phytoplankton activity. The decay rate has an e folding length δ of 35 m, a maximum value λ_0 at the surface and is constrained to decay to zero at z_1 :

$$\lambda(z_i) = \lambda_0 \frac{z_i - z_1}{z_1} e^{\frac{z_i}{\delta}}. \quad (4.2)$$

The vertical profile in (4.2), shown by the blue line in Fig. 4.4a, has been chosen in order to take into account the depth-dependent consumption of iron, associated with light irradiance. Mongin et al. (2009) estimated an optimal annual averaged decay rate at the surface of 0.015 day^{-1} . We test the sensitivity of dissolved iron concentration to the decay rate, with $\lambda_0 = (0.004, \mathbf{0.015}, 0.03) \text{ day}^{-1}$ (the bold value indicates our reference case).

Replenishment rate

The second term in the RHS of equation (4.1) determines the relaxation of DFe_i to the particle background mean concentration $\langle DFe \rangle_i$, whose value depends on the location of the particle. The timescale of the replenishment is governed by a structure function, $f(z_i)$. The function $f(z_i)$ (green line in Fig. 4.2a) depends on a timescale γ (units are day^{-1})

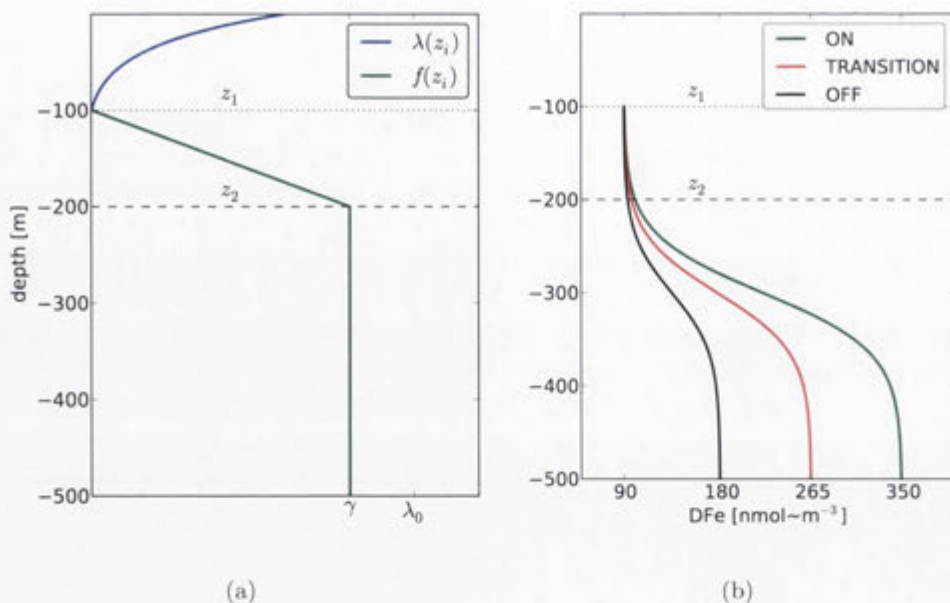


Figure 4.4: (a) Vertical profiles of (blue) decay rate $\lambda(z_i)$ from equation (4.2) and (green) structure function $f(z_i)$ for the relaxation term (4.3). (b) Vertical profiles of $\langle DFe \rangle_i$ as computed by solving (4.4), for the *ON* (green line) and *OFF* (black) the plateau areas, and in the transition zone (red) (for clarity, only the first 500 m are shown).

and depth z_i , as:

$$f(z_i) = \begin{cases} \gamma & z_i \leq z_2 \\ \frac{\gamma(z_i - z_1)}{z_2 - z_1} & z_1 < z_i < z_2 \\ 0 & z_i \geq z_1. \end{cases} \quad (4.3)$$

We allow a replenishment only at depths $z_i < z_1$: replenishment is thus distinct from the loss of iron to primary productivity in the euphotic zone. We vary the replenishment timescale $\tau = 1/\gamma$ from a minimum of 0.1 days to 10 days (0.1, 0.2, 0.5, 1, 5, 10).

Mean concentration of DFe

Below z_1 , the i -th particle is relaxed to a mean ($\langle \cdot \rangle$) concentration that depends on its relative position to the plateau and on its depth (Fig. 4.3):

$$\langle DFe \rangle_i = A - B \tanh\left(-\frac{300 + z_i}{z_2} \pi\right), \quad (4.4)$$

where $A = \frac{\max(\langle DFe \rangle) + \min(\langle DFe \rangle)}{2}$ and $B = \frac{\max(\langle DFe \rangle) - \min(\langle DFe \rangle)}{2}$. The minimum value of $\langle DFe \rangle$ in parameters A and B is defined as 90 nmol m⁻³, everywhere in the domain (based on the measured mixed layer value found by Blain et al. (2007)). The maximum value depends on the horizontal location of the particle. Based on observed mean concentrations of DFe at depth (Blain et al., 2007), we define a value of 350 nmol m⁻³ as

$\max(\langle DFe \rangle)$ in the *ON* region and 180 nmol m^{-3} as $\max(\langle DFe \rangle)$ in the *OFF* region. In the transition zone, we choose a maximum value given by the middle point between the two maximum concentrations in the *ON* and *OFF* regions. It must be noted that this mean concentration reflects processes for the supply of dissolved iron, such as diffusive, that has not been included in the model. This simple choice allows us to reduce the difficulty that including additional processes would bring.

The profile in (4.4) has been chosen to idealise the profile in Figure 2 of Blain et al. (2007) and to consider a ferricline, or the depth where the vertical gradient of DFe is maximum (Tagliabue et al., 2014), of 300 m. This value has been chosen in order to follow the result reported in Tagliabue et al. (2014) for the mean depth of the ferricline in the Southern Ocean, and in particular for the Kerguelen Plateau region (their Fig. 1a).

Furthermore, for depths above or equal to z_1 it is clear from (4.1) that the dissolved iron concentration reaches a zero steady state solution. This has been chosen in order to focus just on advective processes as mechanisms of supply of DFe .

Initialisation of DFe_i

The initial value of iron concentration depends on the depth of the particle: if deeper than z_1 , it is initialised to $\langle DFe \rangle_i$ from equation (4.4), otherwise its initial value is zero. This formulation has been chosen in order to isolate deep sources of dissolved iron and how the different flows influence its transport from depth.

4.3.2 Sensitivity to FeRRO_{SO} parameters

The FeRRO_{SO} model is a new technique designed to isolate different components of advective transport of tracers in a complex three dimensional flow field. Before using the model, we first explore the sensitivity of FeRRO_{SO} to a range of values of the governing parameters: the decay and replenishment rates (listed in sections 4.3.1 and 4.3.1 respectively). We focus on the total concentration of iron, as defined by equation (4.5) below, and on upwelling iron fluxes, computed as mean of local fluxes $w_i \cdot DFe_i$, where w_i is the upward vertical velocity of the i -th particle at the release time and location). The average concentration of iron is estimated as

$$[DFe] = \frac{\sum_{i=0}^N [DFe_i] \cdot dV_i}{V}, \quad (4.5)$$

where $[DFe_i]$ is the concentration of the i -th particle, computed at the seeding position occupied by the i -th Lagrangian particle. dV_i is the volume of the particle i at this location: we highlight that dV_i is valid only at the very moment of seeding, as this is the only instant in time where we can define a representative volume for each particle. At this instant, $dV_i = dx_i \cdot dy_i \cdot dz_i$, where the increment in the longitude direction (dx_i) is a function of latitude y_i (as our ocean circulation models use spherical coordinates) and varies between approximately 3580 m and 3830 m. Increments in latitude and depth are: $dy_i = 5560 \text{ m}$ and $dz_i = 125 \text{ m}$, for each particle. Finally, V represents the total volume

occupied by the particles: $V = \sum_{i=0}^N dV_i$. Note that for this calculation we evaluated a mean of both particles initialised at 75 m and 200 m, excluding those whose vertical displacement never exceeds z_1 .

The sensitivity is shown in Fig. 4.5: the left panel shows the sensitivity to the decay rate λ , with the dependence on the replenishment timescale τ on the right. Results show the difference from the reference case expressed as a percentage of $[DFe]$ (panels a,b) and of $w \cdot DFe$ (c,d). Results from the two regions are presented: black lines are for R_1 , blue for R_2 . $FeRRO_{SO}$ is not significantly sensitive to the chosen values of λ , in both regions: we can estimate a maximum change in $[DFe]$ of less than $\pm 1\%$ in both R_1 and R_2 . The sensitivity to the timescale of relaxation τ is also weak, giving approximately $\pm 3\%$ (R_1) and $\pm 4\%$ (R_2). The change in vertical fluxes (Fig. 4.5c) shows a larger sensitivity to the change of λ , of approximately $\pm 2\%$ in R_1 and $\pm 1.5\%$ in R_2 , while the sensitivity to the timescale is weaker, with a maximum change of less than $\pm 1\%$ (R_1) and $\pm 3\%$ (R_2) (Fig. 4.5d).

The results reported here are for the highest resolution case, however, we found similar sensitivity for the $1/20^\circ$ experiment. We conclude that the sensitivity of $FeRRO_{SO}$ to the choice of parameters is weak, which might indicate that the transition of the particles in the water column due to the advective contribution of mesoscale and sub-mesoscale flows act on timescales faster than the decay and restoring rates.

4.4 Results

Dissolved iron statistics are analysed with a focus on the sensitivity of total concentration of iron $[DFe]$ and vertical fluxes of iron to the horizontal resolution. The goal of this analysis is to delineate the contribution that sub-mesoscale dynamics, resolved only by the $1/80^\circ$ resolution model, have over the supply of iron. Emphasis is given also to the impact of the resolution upon the sources of iron, for the two regions of study. To investigate the different iron sources, we delineate between *ON* and *OFF* particles, where *ON* particles are those that reach the *ON* plateau region during their lifetime. Conversely, the *OFF* particles are defined as those that never touch the *ON* region; for this analysis *OFF* particles include those found in the transition zone (the *ON* boundaries are defined in subsection 4.3.1).

In addition, we have found that a fraction of particles remains in the first 100 m of the water column. We note that the number of these particles decreases with the resolution: in the lowest resolution case we estimated that 18% of particles in R_1 and the 33% in R_2 do not go deeper than 100 m, while only 13% of particles (in both R_1 and R_2) did not exceed 1000 m in the highest resolution case. These numbers are consistent with our findings (Fig. 4.3) that in the high resolution case there are more deep-reaching flows than at low resolution.

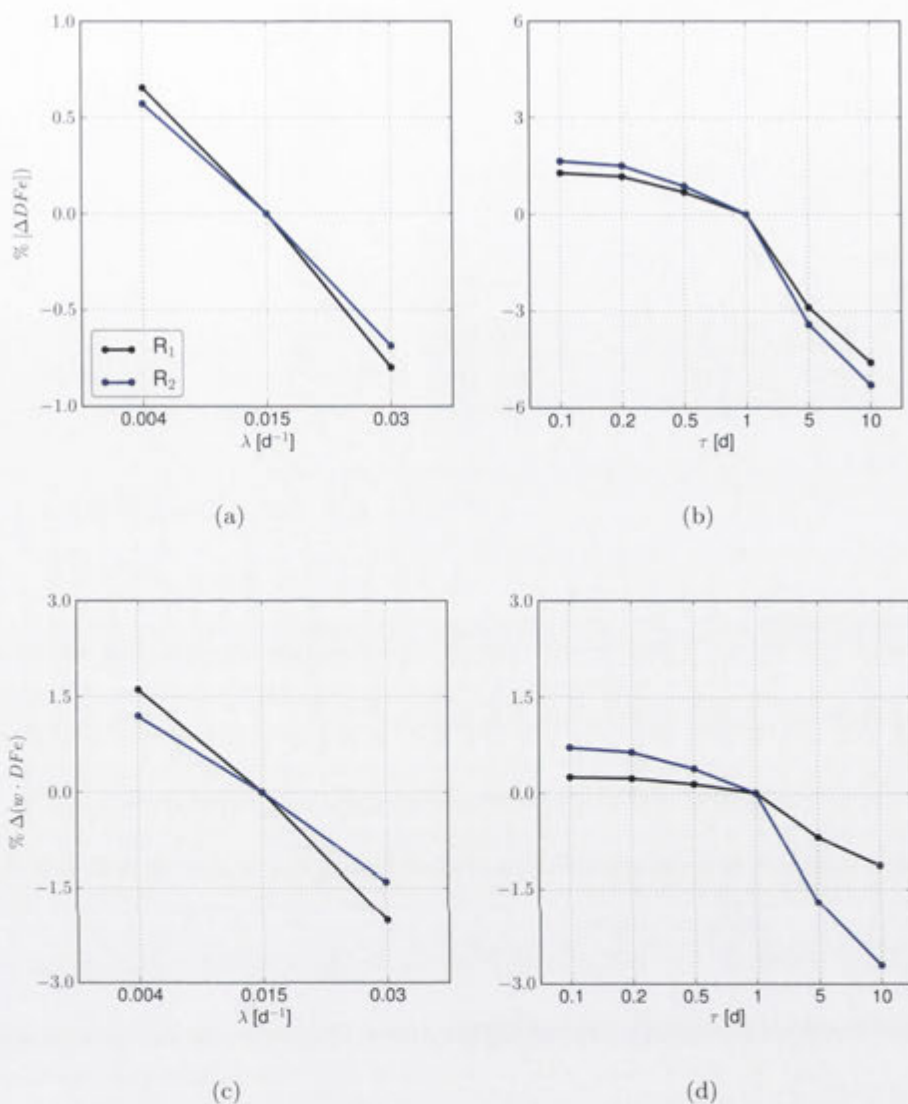


Figure 4.5: Sensitivity of dissolved iron concentration (a, b) and vertical iron fluxes (c, d) to decay rate (a, c) and relaxing timescale (b, d) for the particles in region R₁ (black lines) and R₂ (blue). Shown are results for the 1/80° resolution experiment. The ordinate axis indicates the difference from the reference case, expressed as a percentage.

4.4.1 Iron Concentration

The average concentration of iron has been computed in the two regions and a representative case with $\lambda_0 = 0.015 \text{ day}^{-1}$ and $\gamma = 1 \text{ day}^{-1}$ is shown in Fig. 4.6a. In this figure, red bars are used for the 1/20° resolution case, while black indicates the 1/80° resolution. $[DFe]$ has been separated into the contribution from particles that move over the plateau (*ON*) and particles that do not (*OFF*). The magnitude of the dissolved iron concentration for the two sources is shown in Table 4.1.

The sensitivity of $[DFe]$ to the resolution is evident from Fig. 4.6a, in both regions. In R₁, *ON* particles contribute 59% and 75% of the $[DFe]$ in the low and high resolution

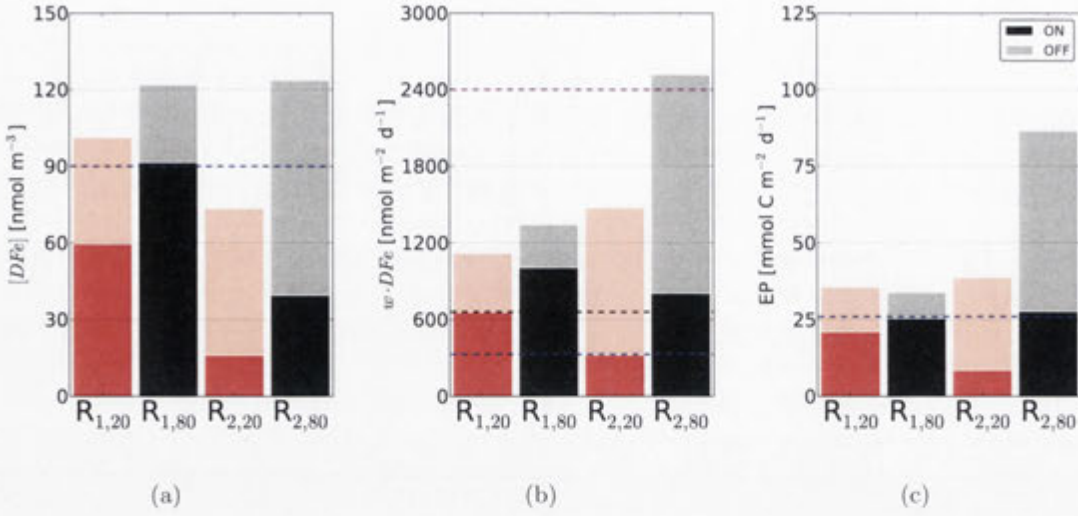


Figure 4.6: (a) Average dissolved iron concentration (particles released at both 75 m and 200 m are considered), (b) vertical fluxes of dissolved iron at 200 m and (c) export production estimated from the fluxes at 75 m for the two regions of analysis (R_1 and R_2). Red (black) bars show the results for the $1/20^\circ$ ($1/80^\circ$) resolution model. The contribution due to the *ON*, *OFF*, as a proportion of the total number of particles, are indicated by the different shading. The blue dashed line in panel a indicates the $[DFe]$ over the plateau as observed by Blain et al. (2007). In panel b, the horizontal dashed lines identify estimates by Bowie et al. (2014): vertical flux due to upwelling (blue), total vertical flux due to the sum of diffusion, upwelling and entrainment (black) and lateral advective iron supply (magenta). Blue line in panel c is the observed net primary production observed in region R_1 by Bowie et al. (2014).

case, respectively. The highest resolution case has slightly more $[DFe]$ (approximately 20 nmol m^{-3}) than the $1/20^\circ$ resolution case and at both resolutions the simulated $[DFe]$ shows an enhancement with respect to the $(90 \pm 34) \text{ nmol m}^{-3}$ of mean dissolved iron concentration observed by Blain et al. (2007) (estimated in the surface mixed layer both *ON* and *OFF* the plateau; dashed blue line in Fig. 4.6a).

In R_2 *ON* particles account for 22% and 32% of the $[DFe]$ in the $1/20^\circ$ and $1/80^\circ$ resolution case, respectively. The greater contribution of the *OFF* particles is consistent with the greater eddy activity in the vicinity of the region and its greater distance from the plateau. Again, the highest resolution simulation has more $[DFe]$ than the lowest resolution case (about 49 nmol m^{-3}), but for this region the lowest resolution case has less DFe than observed (about 20%) than Blain et al. (2007) estimates, while more at the highest (approximately 33% more).

4.4.2 Vertical fluxes of DFe

Vertical fluxes, computed for the case $\lambda_0 = 0.015 \text{ day}^{-1}$ and $\gamma = 1 \text{ day}^{-1}$, are shown in Fig. 4.6b. We focus our investigation on the flux into the base of the mixed layer; hence, only the upward fluxes into the 200 m layer are here presented. The sensitivity to the

Resolution	R _{1,TOT}	R _{1,ON}	R _{1,OFF}	R _{2,TOT}	R _{2,ON}	R _{2,OFF}
Concentration of iron averaged between 75 m and 200 m [nmol m ⁻³]:						
1/20°	100	59	41	73	16	57
1/80°	120	90	30	122	39	83
Vertical fluxes of iron estimated at 75 m [nmol m ⁻² d ⁻¹]:						
1/20°	749	442	307	814	179	635
1/80°	711	533	178	1816	581	1235
Vertical fluxes of iron estimated at 200 m [nmol m ⁻² d ⁻¹]:						
1/20°	1106	653	453	1449	319	1130
1/80°	1299	974	325	2472	791	1681
Export productivity estimated at 75 m [mmol C m ⁻² d ⁻¹]:						
1/20°	36	21	15	39	9	30
1/80°	34	25	9	87	28	59
Total productivity estimated at 75 m [mmol C m ⁻² d ⁻¹]:						
1/20°	73	43	30	79	17	62
1/80°	69	51	18	177	57	120

Table 4.1: Dissolved iron concentration, vertical iron fluxes and estimated production for the two regions of analysis, due to *TOT*, *ON* and *OFF* particles, and at the two resolutions. The export production estimates (EP) are computed from a DFe/C ratio of 0.021 mmol Fe mol⁻¹ C (from Bowie et al., 2014), and then converted into total production using an fe ratio of 0.49 (from Sarthou et al., 2008).

horizontal resolution of upwelling iron fluxes is, as for the $[DFe]$, more dramatic in R₂ than in R₁. We note that the vertical flux in the second region is larger by a factor of 2 in the 1/80° case, while the flux at the highest resolution in R₁ is just 15% larger. The values of upward vertical fluxes due to the different sources in presented are Table 4.1.

To put these values into context, we compare them with estimates of upwelling fluxes by Bowie et al. (2014). We are able to compare only region R₁ with their “plume” stations. Here, the authors found a maximum vertical flux of 330 nmol m⁻² d⁻¹ (indicated by a blue horizontal line in Fig. 4.6b), that, compared to our measurements, is smaller by a factor of 3.3 in the 1/20° resolution case and of 4 in the 1/80°. Bowie et al. (2014) estimated also a maximum total vertical supply of dissolved iron (due to upwelling, diffusion and entrainment) of 661 nmol m⁻² d⁻¹, 1.7 times smaller than our estimate of iron fluxes (due to only upwelling) at the 1/20° resolution. In the high resolution case our physical DFe supply is nearly double the estimate of Bowie et al. (2014), but it is still significantly less than Bowie et al. (2014) estimate of atmospheric and sediment supply.

4.4.3 Primary production estimates

To estimate the export production in the two regions we consider two calculations: vertical supply of iron to the euphotic zone (i.e. at 75 m; equation 4.6) and a biological uptake computed using the decay rate (equation 4.9). Then, we use a DFe/C ratio to convert the estimate into an estimate for carbon export (EP). DFe/C is the mixed layer cellular uptake ratio, as observed in the “plume” region by Bowie et al. (2014) and estimated as (0.021 ± 0.002) mmol Fe mol⁻¹ C.

The export based on the vertical supply of iron is given by:

$$\frac{w \cdot DFe}{DFe/C}. \quad (4.6)$$

At 75 m, and in the release location, we estimate an export primary production of (36 ± 3) mmol C m⁻² d⁻¹ in R₁ for the 1/20° resolution model and of (34 ± 3) mmol C m⁻² d⁻¹ at 1/80° resolution. Given an absence of observed values in R₂, we use the same conversion ratio for this region and find that at the lowest resolution its export primary production is approximately (39 ± 8) mmol C m⁻² d⁻¹, whereas it is (87 ± 8) mmol C m⁻² d⁻¹ in the highest resolution case. Fig. 4.6c shows the estimates of EP, per region, resolution and source of particles. The blue line represents an observed EP (localised in region R₁) of approximately (26 ± 1) mmol C m⁻² d⁻¹ computed from the downward particulate iron export of (541 ± 216) nmol m⁻² d⁻¹ of Bowie et al. (2014). Estimates of the simulated EP relative to each source are reported in Table 4.1.

In R₁ the EP is about a third above the observed value at each resolution. In region R₂ we note an increase of more than a factor of 2 in the EP due to the resolution. Here, we cannot compare to any estimates, although we would expect EP in region R₂ to be similar or less than R₁ because R₂ is further away from KP than R₁.

The estimated export productivity can be converted into total primary productivity by using the fe ratio, equal to the uptake of new iron/uptake of new + regenerated iron, of 0.49 (Sarrouh et al., 2008). In region R₁ we find a total primary productivity of approximately 73 mmol C m⁻² d⁻¹ and 69 mmol C m⁻² d⁻¹ at 1/20° and 1/80° resolution, respectively. In R₂ the estimated values are 78 mmol C m⁻² d⁻¹ (1/20°) and 177 mmol C m⁻² d⁻¹ (1/80°). This compares to an observed PP estimates in R₁ of 132 mmol C m⁻² d⁻¹. Total primary productivity estimates for the *ON* and *OFF* particles are shown in the last row of Table 4.1. In R₁ our estimate of vertical DFe supply is 1.3 more than what is required to meet the estimated particulate iron export. In R₂ our estimate is 1.5 to 3.3 times the estimated particulate iron export.

While our simulated vertical iron supply is an upper bound particularly at R₂, the supply due to sub-mesoscale processes is substantial, approaching the value estimate for iron supply from the sediments on the KP and is much greater than the estimated export.

However, we highlight that the computation of export production based on upward iron fluxes gives a maximum estimate, as physical flows can transport iron downward as well. Hence, we can calculate the biological export of iron at the base of the euphotic layer

(z^*) as the flux required to balance the loss of iron by biological consumption ($S(z)$):

$$S(z) - \frac{\partial \phi_{Fe}(z)}{\partial z} = 0. \quad (4.7)$$

$\phi_{Fe}(z)$ represents the vertical flux of iron and its value at $z = z^*$ can be obtained by integrating (4.7) over the euphotic layer:

$$\phi_{Fe}(z^*) = - \int_{z^*}^0 S(z) dz. \quad (4.8)$$

The consumption $S(z)$ is given by the first term in the right hand side of equation (4.1):

$$S(z) = -\lambda(z)DFe(z),$$

where $\lambda(z)$ is given by (4.2). From simple passages, we can obtain a general formulation for the biological export of iron:

$$\phi_{Fe}(z^*) \sim \lambda_0 \delta \left[\frac{\delta}{z^*} \left(e^{z^*/\delta} - 1 \right) - 1 \right] DFe(z^*). \quad (4.9)$$

In our model we use $z^* = z_1 = 75$ m and $\delta = 35$ m. The biological export of iron in (4.9) can be then converted into export production using the Fe/C ratio and total production using the fe ratio. We find that at $1/20^\circ$ resolution the total production accounts for approximately $7 \text{ mmol C m}^{-2} \text{ d}^{-1}$ in R_1 and $3 \text{ mmol C m}^{-2} \text{ d}^{-1}$ in R_2 , while at $1/80^\circ$ we estimate $9 \text{ mmol C m}^{-2} \text{ d}^{-1}$ and $10 \text{ mmol C m}^{-2} \text{ d}^{-1}$ in R_1 and R_2 , respectively.

While these numbers are much smaller than the upwelled supply of iron estimated above (from equation 4.6) they still account for the significant portion of measured iron EP. In R_1 , vertical physical supply accounts for about a third of the estimate particulate iron export (26 ± 1) $\text{mmol C m}^{-2} \text{ d}^{-1}$. In this region adjacent to the KP the horizontal supply of iron is more important consistent with previous observations. In the $1/80^\circ$ resolution R_2 , the estimate iron export is nearly a half the measured export. In this region resolving the sub-mesoscale vertical supply of iron is important and could be the dominant mechanism of iron supply.

4.5 Discussion and Conclusions

FeRRO_{SO} represents an innovative technique for the study of specific processes affecting iron concentration in iron-limited waters, such as the Southern Ocean. The model has been applied to a framework that does not incorporate the contribution of diffusive mechanisms as our motivation was to specifically investigate the impact of sub-mesoscale advection on the supply of iron. FeRRO_{SO} has just two parameters, a decay and a replenishment time-scales, chosen to represent bio-geochemical processes not explicitly resolved in FeRRO_{SO} . We show these two parameters have a weak effect on the final estimates of iron concentration and fluxes. This insensitivity to parameters is due to the timescale of

the upward/downward advection of the particles in the upper 100 m of the water column being shorter than the iron decay timescale. Also, in case of the replenishment timescale τ , which we have varied over two orders of magnitudes, we have not found a significant difference in the behaviour of FeRRO_{SO} . Thus we conclude that FeRRO_{SO} is robust and that it does not depend on the choice of parameters.

While the results presented above are not sensitive to the choice of the parameters, they do depend on the location of investigation and on the horizontal resolution of the numerical model. This sensitivity reflects the different dynamics resolved by the simulations, which are also strongly affected by the location of analysis (Chapter 3). We have shown that iron concentration, fluxes and primary productivity are comparable in region R_1 , where the sub-mesoscale activity is weak (Chapter 2). Conversely, in region R_2 , where the sub-mesoscale dynamics are the most active (Chapter 2), we simulate an increase in iron estimates with the horizontal resolution, demonstrating that sub-mesoscale processes have an impact on the transport of dissolved iron.

At R_1 we estimate a vertical iron supply that is slightly greater than the observed value reported in Bowie et al. (2014), but it shows little difference with resolution. Moreover here it is less than a third the estimate for horizontal advection of iron from the KP. We confirm that in this region the dominant contribution to the supply of iron is most likely due to lateral processes. R_1 is closer to KP than R_2 , which might explain the larger impact of the lateral supply.

Our results suggest that in R_2 the vertical supply is a first order mechanism for the supply of iron. Furthermore, as the vertical flux increases with the resolution, we conclude that iron supply in this region is likely to be predominantly due to sub-mesoscale upwelling of dissolved iron. However, we are not able to compare our estimated iron supply of R_2 with any observed estimates. Following Mongin et al. (2009) we can expect a smaller lateral advection into this region (as they found that the lateral supply decays with the distance from the plateau). We find that the vertical iron supply, approaches the estimated value for the horizontal advection of DFe in R_1 . Furthermore, using the calculation from the decay rate (equations 4.2 and 4.9) we find that the simulated EP accounts for about a half the measured EP. This calculation requires an assumption that EP from R_1 can be used for R_2 which may not strictly hold; the observed EP most likely provides an upper estimate.

From the large difference in the $1/80^\circ$ vertical fluxes between the two regions (almost 2-fold), a similar difference in the concentration could be expected. Yet, the difference in the concentration is just about 2%. The reason is likely due to a combination of downward iron flux (which may be as large as the upward component) and biological uptake.

We highlight that in our numerical simulations no seasonal cycle has been modelled and, therefore, FeRRO_{SO} estimates are purely indicative of a mean state. It would be of great interest for the scientific community to investigate how the seasonal variation can affect the iron supply, however this is beyond the scope of the present work. Furthermore, a future development should include a more realistic implementation of bio-geochemical

processes.

We conclude that sub-mesoscale dynamics can affect the near-surface budgets of dissolved iron concentration and export production, by enhancing the vertical advective fluxes of dissolved iron concentration in Southern Ocean conditions. We suggest that sub-mesoscale fluxes need to be parameterised in coarser resolution models for the quantification of iron budgets; however, these parameterisations need to take into account the complex spatial variations present in sub-mesoscale dynamics.

Conclusions

5.1 Summary

Investigating the role that sub-mesoscale processes play in the ocean dynamics is not a trivial quest. The spatial and temporal scales of these processes make observations particularly difficult and their representation in ocean models often requires parameterisation. The research of the present work has opened a path towards a new investigation of sub-mesoscale dynamics in regional ocean models.

The foundation of this thesis has been the implementation of an ultra-high-resolution numerical ocean model that, at $1/80^\circ$ horizontal resolution, constitutes the first Southern Ocean sub-mesoscale-resolving model. Moreover, with the use of a realistic topography and a total domain size given by $(5760 \times 1080 \times 150)$, this model represents the new frontier in sub-mesoscale numerical studies.

The sub-mesoscale-resolving ocean model of the south Indian Ocean has unveiled the presence of a sub-mesoscale activity which is not uniformly distributed in space, but instead forms hotspots (Chapter 3). The strength of this sub-mesoscale activity varies widely, depending on the location: in areas of strong circulation (such as east of the Kerguelen Plateau), the magnitude of sub-mesoscales is greatest; whereas, in areas where the circulation is very weak (e.g. over the plateau) it is much smaller. A major finding of this thesis is that the inhomogeneity at the sub-mesoscales is indirectly due to the topography, where the topography controls the large-scale flow, mesoscale eddies are created via instabilities, which in turn generate sub-mesoscale structures. These findings also highlight that topographically-induced internal wave activity and direct generation of sub-mesoscale flows by the topography are found to be significant only in specific regions and are not the main components of the observed inhomogeneity.

In the south Indian Ocean, sub-mesoscale flows generate upper-ocean vertical velocities dramatically larger than mesoscale velocities: instantaneous values show that vertical velocities are one order of magnitude larger in the sub-mesoscale case (Chapter 2). This result, which might be expected from other studies, represents the first quantification of the sub-mesoscale vertical velocities in Southern Ocean numerical models. In addition, by enhancing the resolution from $1/20^\circ$ to $1/80^\circ$, the root mean square of the sub-mesoscale vertical velocities sees an 11-fold enhancement, for an increase in resolution of 4 times, which gives a ratio (equal to 2.75) larger than found in previous studies of sub-mesoscale

dynamics. These large vertical velocities have a significant impact on the vertical transport of Lagrangian particles. Specifically, they induce a wider spread in the water column and advect waters from greater depths than the $1/20^\circ$ resolution vertical velocities.

The horizontal resolution has a large impact also on the advective vertical fluxes of iron, with an enhancement associated with the increase of the resolution up to 2 times (Chapter 4). Iron concentration and fluxes are not only sensitive to the resolution, but this sensitivity is found depending on the location of analysis, with a larger difference associated to the region with stronger sub-mesoscale activity. Finally, by supplying more iron into the upper-ocean, sub-mesoscale dynamics are therefore found to sustain a larger primary productivity.

5.2 Future directions

Sub-mesoscale-oriented studies are rapidly evolving and this work has pushed at the frontiers of Southern Ocean modelling. However, there are still open questions which can lead to future research paths. In particular, the computationally expensive nature of these ultra-high-resolution simulations has prevented additional experiments with different forcing, such as temporally-varying winds or heat fluxes. Furthermore, numerical and observational studies would both acquire a substantial benefit if a more exhaustive comparison with high-resolution observations were conducted. And finally, as sub-mesoscale processes need to be parameterised in coarser-resolution models, the numerical simulations here presented could offer a valuable test for existing parameterisations and, additionally, guide towards new implementations.

5.2.1 Towards more realistic simulations

Numerical simulations presented in this thesis have been forced by constant annual averages of wind stress, heat and freshwater fluxes. This constant forcing has the advantage of reducing the degree of complexity in the implementation and analysis, but comes at the expense of a complete representation of the variability of the circulation and dynamics of the Southern Ocean. In particular, future generations of high-resolution ocean models should be able to integrate a more realistic forcing, including high-frequency winds, a seasonal cycle and sea ice (and its dynamics).

Temporal high-frequency winds have been seen to enhance the magnitude of vertical velocities, as well as stimulating new production in an idealised numerical simulation of oligotrophic waters, by triggering transient fluxes of nutrients into the surface (Lévy et al., 2009). Spatial and temporal high-frequency winds in a regional model of the ocean circulation around the Hawaiian islands have also been seen to magnify vertical velocities, via non-linear interactions between the wind stress and the vertical relative vorticity (Calil et al., 2008). Therefore, adding this variability in the wind forcing would improve the study of sub-mesoscale dynamics and their impact on biological processes in the Southern Ocean.

However, variability in the wind forcing may also trigger the generation of near-inertia

gravity waves. Numerical simulations found that these waves can deeply penetrate in the water column, with maxima in their vertical velocity found around 2000 m and in some cases extending to the upper levels (Komori et al., 2008; Blaker et al., 2012). The order of magnitude of their vertical velocities is comparable to the sub-mesoscale-generated vertical velocity. Therefore, particular considerations and analyses must be taken into account to distinguish them from sub-mesoscale dynamics.

Observations in the Southern Ocean, already difficult all year round, are made even more extreme in winter, due to the the rigid temperatures and the increase in intensity of winds and mean sea swell. In this context, the capability of simulating a seasonal cycle could help to fill a gap in winter-time observations and to study the seasonal cycle of sub-mesoscale features, which are amplified in winter (e.g Mensa et al., 2013).

The Southern Ocean is location for the formation of the densest water in the world, the Antarctic bottom water, which relies on the existence of polynyas, regions of open water surrounded by ice, and sea ice formation. Sea ice is also fundamental in the heat exchange between ocean and atmosphere and omitting its representation and dynamics can lead to non realistic air-sea fluxes, ocean stratification and dynamics around Antarctica (which can then affect the ocean circulation around the globe). For example, Hewitt et al. (2001) found that representing sea ice formation alone and not its dynamics in an ocean-sea-ice model led to a non realistic sea ice distribution in the Southern Ocean. In turn, this gave rise to different responses in the climate sensitivity of the model. Consequently, adding dynamical sea ice model would undoubtedly be fundamental for a realistic representation of the Southern Ocean dynamics and circulation.

Finally, Chapter 2 and 4 employ Lagrangian particles for the study of the impact of the resolution on the vertical transport and fluxes of iron. These particles have several advantages: first, their simulations are computationally very cheap; second, they can be implemented off-line; and, finally, they allow the investigation of sources and horizontal and vertical distributions of waters, as they can be advected both backward and forward in time. However, there are caveats on such analyses as they omit the diffusive contribution of the flow and do not permit to simulate the response and distribution of a biological system. Also, the Lagrangian technique does not give any information about the temporally-evolving vertical structure of a nutrient profile, an important aspect for phytoplankton bloom studies. To cover these limitations, an improved methodology would require to incorporate a sophisticated bio-geochemical (or BGC) model, that could include an iron cycle, to the physical model. So far BGC models with iron cycles have been implemented at coarser resolutions (e.g. Gregg et al., 2003; Parekh et al., 2004; Moore et al., 2004; Moore and Braucher, 2008; Völker and Tagliabue, 2014), but have never been used at sub-mesoscales. The accuracy of these models relies not only on the capability to represent complex bio-geochemical processes, but also on how accurate the initial distribution of dissolved iron is (as highlighted by Moore et al., 2004). A database of large-scale iron distribution in the Southern Ocean has just become available (Tagliabue et al., 2012), however to extend the application of such models to the scales of few km,

an improved compilation of iron sources is needed. Furthermore, by adding a seasonal cycle to high-resolution physical-bio-geochemical models, it would be possible to simulate and investigate the life cycle of a phytoplankton bloom in iron-limited Southern Ocean waters, and to investigate the seasonal response of vertical fluxes of iron and its spatial and temporal evolution.

5.2.2 Coupling of high-resolution models and observations

Ocean models are valuable tools for the investigation of processes that are difficult to observe. However, they always need validation in order to be used as realistic predictions and description of processes, either physical, biological or chemical.

A first assessment of the numerical models presented in this thesis is included in Chapter 2. In this assessment, the ocean mean state and the magnitude of vertical velocities in the models were compared with estimates from the Southern Ocean Fine Structure (SOFINE, Phillips and Bindoff, 2014) and the cumulative transport of the ACC to the evaluations of Park et al. (2009). However, a more thorough comparison of the three dimensional velocity and hydrographic structure at the SOFINE site would be of considerable benefit, not only for the validation of the numerical simulations, but also to provide additional information of the state of water masses where observations are lacking.

Compared to the Northern Hemisphere, Southern Ocean observations are in deficit and sparse. In particular, sub-mesoscale observational campaigns so far are very limited. In the Southern Ocean these studies include a glider-based experimental study of mixed layer dynamics and phytoplankton distribution in the Sub-Antarctic zone (Swart et al., 2014) and the investigation of the vertical structure of the three dimensional velocity field with profiling floats during the SOFINE campaign (Phillips and Bindoff, 2014). For an advancement in the study of the biological activity in the Kerguelen Plateau, observations of vertical velocities, nutrients, chlorophyll and hydrography are necessary across sub-mesoscale fronts. In combination with recent studies (e.g. Park et al., 2014; Bowie et al., 2014), the results discussed in these pages could be used to help planning future observational campaigns at this site.

5.2.3 Improved parameterisation in global ocean models

Large-scale numerical models, such as climate models, rely on the parameterisation of processes that occur at unresolved scales. Their fidelity, therefore, depends on the precision of such parameterisations.

Chapter 3 attempts a comparison with the existing sub-mesoscale parameterisation of Fox-Kemper et al. (2008), by looking at the correlation between the vertical velocities and the main components of such parameterisation: the horizontal gradient of mesoscale buoyancy and the mixed layer depth. No detailed study has been possible at this stage, however the scientific community would benefit from the development of a more detailed comparison. In particular, the numerical simulations presented in this thesis can be used to identify if ageostrophic baroclinic instabilities occur in the simulations and to look at

their impact on the restratification of the mixed layer (e.g. Thomas and Ferrari, 2008; Fox-Kemper et al., 2008; Canuto and Dubovikov, 2010), over Southern Ocean conditions. Two existing parameterisations can be tested: the overturning streamfunction of Fox-Kemper et al. (2008) and vertical tracer flux of Canuto and Dubovikov (2010), where this latter, compared to Fox-Kemper et al. (2008), is based on more arbitrary conditions and includes wind forcing. Such an investigation could reveal if and where these parameterisations are valid, in a sub-mesoscale model with realistic topography, and help to guide further improvements. On this subject, Chapter 3 suggested a new parameterisation based on the mesoscale eddy kinetic energy and strain rate, whose development has not yet been done, but which could be used to compare with Fox-Kemper et al. (2008) and Canuto and Dubovikov (2010) .

Bibliography

- Abraham, E. R., C. S. Law, P. W. Boyd, S. J. Lavender, M. T. Maldonadok, and A. R. Bowie, 2000: Importance of stirring in the development of an iron-fertilized phytoplankton bloom. *Nature*, **407**, 727–730.
- Adcroft, A. and J.-M. Campin, 2004: Rescaled height coordinates for accurate representation of free-surface flows in ocean circulation models. *Ocean Modell.*, **7** (3–4), 269–284.
- Adcroft, A., C. Hill, and J. Marshall, 1997: Representation of topography by shaved cells in a height coordinate ocean model. *Mon. Weather Rev.*, **125** (9), 2293–2315.
- Blain, S., G. Sarthou, and P. Laan, 2008: Distribution of dissolved iron during the natural iron-fertilization experiment KEOPS (Kerguelen Plateau, Southern Ocean). *Deep Sea Res. Part II*, **55** (5), 594–605.
- Blain, S., et al., 2007: Effect of natural iron fertilization on carbon sequestration in the Southern Ocean. *Nature*, **446**, 1070–1074.
- Blaker, A. T., J. J. Hirschi, B. Sinha, B. De Cuevas, S. Alderson, A. Coward, and G. Madec, 2012: Large near-inertial oscillations of the Atlantic meridional overturning circulation. *Ocean Modell.*, **42**, 50–56.
- Boccaletti, G., R. Ferrari, and B. Fox-Kemper, 2007: Mixed layer instabilities and restratification. *J. Phys. Oceanogr.*, **37** (9), 2228–2250.
- Bowie, A. R., et al., 2014: Iron budgets for three distinct biogeochemical sites around the Kerguelen archipelago (Southern Ocean) during the natural fertilisation experiment KEOPS-2. *Biogeosc. Discuss.*, 17 861–17 923.
- Bown, J., M. Boye, P. Laan, A. Bowie, Y.-H. Park, C. Jeandel, and D. M. Nelson, 2012: Imprint of a dissolved cobalt basaltic source on the Kerguelen Plateau. *Biogeosc.*, **9**, 5279–5290.
- Boyd, P. W., et al., 2000: A mesoscale phytoplankton bloom in the polar Southern Ocean stimulated by iron fertilization. *Nature*, **407** (6805), 695–702.
- Bucciarelli, E., S. Blain, and P. Tréguer, 2001: Iron and manganese in the wake of the Kerguelen Islands (Southern Ocean). *Mar. Chem.*, **73** (1), 21–36.
- Calil, P. H., K. J. Richards, Y. Jia, and R. R. Bidigare, 2008: Eddy activity in the lee of the Hawaiian Islands. *Deep Sea Res. Part II*, **55** (10), 1179–1194.

- Canuto, V. and M. Dubovikov, 2010: Mixed layer sub-mesoscale parameterization – Part I: Derivation and assessment. *Ocean Sci.*, **6**, 679–693.
- Capet, X., J. C. McWilliams, M. J. Molemaker, and A. F. Shchepetkin, 2008a: Mesoscale to submesoscale transition in the California Current system. Part I: Flow structure, eddy flux, and observational tests. *J. Phys. Oceanogr.*, **38** (1), 29–43.
- Capet, X., J. C. McWilliams, M. J. Molemaker, and A. F. Shchepetkin, 2008b: Mesoscale to submesoscale transition in the California Current system. Part II: Frontal processes. *J. Phys. Oceanogr.*, **38** (1), 44–64.
- Capet, X., J. C. McWilliams, M. J. Molemaker, and A. F. Shchepetkin, 2008c: Mesoscale to submesoscale transition in the California Current system. Part III: Energy balance and flux. *J. Phys. Oceanogr.*, **38** (10), 2256–2269.
- Carlson, C., N. Bates, D. Hansell, and D. Steinberg, 2001: Carbon cycle. *Encycl. Ocean Sci.*, 390–400.
- Chapman, C. C. and R. Morrow, 2014: Variability of Southern Ocean jets near topography. *J. Phys. Oceanogr.*, **44** (2), 676–693.
- Chelton, D., R. DeSzoek, M. Schlax, K. El Naggar, and N. Siwertz, 1998: Geographical variability of the first baroclinic Rossby radius of deformation. *J. Phys. Oceanogr.*, **28**, 433–460.
- Chever, F., G. Sarthou, E. Bucciarelli, S. Blain, A. R. Bowie, et al., 2010: An iron budget during the natural iron fertilisation experiment KEOPS (Kerguelen Islands, Southern Ocean). *Biogeosc.*, **7**, 455–468.
- Coale, K. H., et al., 2004: Southern Ocean iron enrichment experiment: carbon cycling in high- and low-Si waters. *Science*, **304** (5669), 408–414.
- Colton, M. T. and R. R. P. Chase, 1983: Interaction of the Antarctic Circumpolar Current with bottom topography: An investigation using satellite altimetry. *J. Geophys. Res.*, **88** (C3), 1825, doi:10.1029/JC088iC03p01825.
- Cunningham, S., S. Alderson, B. King, and M. Brandon, 2003: Transport and variability of the Antarctic Circumpolar Current in Drake Passage. *J. Geophys. Res.*, **108** (C5), doi:10.1029/2001JC001147.
- Damerell, G. M., K. J. Heywood, and D. P. Stevens, 2013: Direct observations of the Antarctic Circumpolar Current transport on the northern flank of the Kerguelen Plateau. *J. Geophys. Res.*, **118** (3), 1333–1348, doi:10.1002/jgrc.20067.
- Daru, V. and C. Tenaud, 2004: High order one-step monotonicity-preserving schemes for unsteady compressible flow calculations. *J. Comput. Phys.*, **193** (2), 563–594.

- de Baar, H. J., A. G. Buma, R. F. Nolting, G. C. Cadée, G. Jacques, and P. J. Tréguer, 1990: On iron limitation of the Southern Ocean: Experimental observations in the Weddell and Scotia Seas. *Mar. Ecol. Prog. Ser.*, **65**.
- de Baar, H. J., et al., 2005: Synthesis of iron fertilization experiments: From the iron age in the age of enlightenment. *J. Geophys. Res.*, **110** (C9), doi:10.1029/2004JC002601.
- d'Ovidio, F., S. De Monte, A. Della Penna, C. Cotté, and C. Guinet, 2013: Ecological implications of eddy retention in the open ocean: A Lagrangian approach. *J. Phys. A: Math. Theor.*, **46** (25), 254023.
- Ducklow, H. W., D. K. Steinberg, and K. O. Buesseler, 2001: Upper ocean carbon export and the biological pump. *Oceanogr.*, **14** (4), 50–58.
- Ferrari, R. and C. Wunsch, 2009: Ocean Circulation Kinetic Energy: Reservoirs, Sources, and Sinks. *Ann. Rev. Fluid Mech.*, **41**, 253–282.
- Fox-Kemper, B., R. Ferrari, and R. Hallberg, 2008: Parameterization of mixed layer eddies. Part I: Theory and diagnosis. *J. Phys. Oceanogr.*, **38** (6), 1145–1165.
- Gille, S., M. Carranza, R. Cambra, and R. Morrow, 2014: Wind-induced upwelling in the Kerguelen Plateau Region. *Biogeosc.*, **11**, 6389–6400.
- Gregg, W. W., P. Ginoux, P. S. Schopf, and N. W. Casey, 2003: Phytoplankton and iron: validation of a global three-dimensional ocean biogeochemical model. *Deep Sea Res. Part II*, **50** (22), 3143–3169.
- Haine, T. W. and P. D. Williams, 2002: The role of nonhydrostatic dynamics in controlling development of a surface ocean front. *Ocean Modell.*, **4** (2), 121–135.
- Hewitt, C., C. Senior, and J. Mitchell, 2001: The impact of dynamic sea-ice on the climatology and climate sensitivity of a GCM: A study of past, present, and future climates. *Climate Dyn.*, **17** (9), 655–668.
- Hoskins, B. J. and F. P. Bretherton, 1972: Atmospheric frontogenesis models: Mathematical formulation and solution. *J. Atmosph. Sci.*, **29** (1), 11–37.
- Jackett, D. R. and T. J. McDougall, 1995: Minimal adjustment of hydrographic profiles to achieve static stability. *J. Atmos. Ocean. Tech.*, **12** (2), 381–389.
- Khatiwala, S., F. Primeau, and T. Hall, 2009: Reconstruction of the history of anthropogenic CO₂ concentrations in the ocean. *Nature*, **462** (7271), 346–349.
- Klein, P., B. L. Hua, G. Lapeyre, X. Capet, S. Le Gentil, and H. Sasaki, 2008: Upper ocean turbulence from high-resolution 3D simulations. *J. Phys. Oceanogr.*, **38** (8), 1748–1763.
- Klein, P. and G. Lapeyre, 2009: The oceanic vertical pump induced by mesoscale and submesoscale turbulence. *Ann. Rev. Mar. Sci.*, **1**, 351–375.

- Komori, N., W. Ohfuchi, B. Taguchi, H. Sasaki, and P. Klein, 2008: Deep ocean inertia-gravity waves simulated in a high-resolution global coupled atmosphere-ocean GCM. *Geophys. Res. Lett.*, **35** (4).
- Lapeyre, G., P. Klein, and B. L. Hua, 2006: Oceanic restratification forced by surface frontogenesis. *J. Phys. Oceanogr.*, **36** (8), 1577–1590.
- Large, W. G., J. C. McWilliams, and S. C. Doney, 1994: Oceanic vertical mixing: A review and a model with a nonlocal boundary layer parameterization. *Rev. Geophys.*, **32** (4), 363–403.
- Lee, D.-K., P. Niiler, A. Warn-Varnas, and S. Piasek, 1994: Wind-driven secondary circulation in ocean mesoscale. *J. Mar. Res.*, **52** (3), 371–396.
- Lévy, M., D. Iovino, L. Resplandy, P. Klein, G. Madec, A.-M. Tréguier, S. Masson, and K. Takahashi, 2012: Large-scale impacts of submesoscale dynamics on phytoplankton: Local and remote effects. *Ocean Modell.*, **43–44**, 77–93.
- Lévy, M., P. Klein, and M. Ben Jelloul, 2009: New production stimulated by high-frequency winds in a turbulent mesoscale eddy field. *Geophys. Res. Lett.*, **36** (16), doi:10.1029/2009GL039490.
- Lévy, M., P. Klein, and A.-M. Tréguier, 2001: Impact of sub-mesoscale physics on production and subduction of phytoplankton in an oligotrophic regime. *J. Mar. Res.*, **59**, 535–565.
- Lévy, M., P. Klein, A.-M. Tréguier, D. Iovino, G. Madec, S. Masson, and K. Takahashi, 2010: Modifications of gyre circulation by sub-mesoscale physics. *Ocean Modell.*, **34**, 1–15.
- Mahadevan, A., 2006: Modeling vertical motion at ocean fronts: Are nonhydrostatic effects relevant at submesoscales? *Ocean Modell.*, **14**, 222–240.
- Mahadevan, A. and A. Tandon, 2006: An analysis of mechanisms for submesoscale vertical motion at ocean fronts. *Ocean Modell.*, **14** (3-4), 241–256.
- Mahadevan, A., A. Tandon, and R. Ferrari, 2010: Rapid changes in mixed layer stratification driven by submesoscale instabilities and winds. *J. Geophys. Res.*, **115** (C03017), doi:10.1029/2008JC005203.
- Maraldi, C., M. Mongin, R. Coleman, and L. Testut, 2009: The influence of lateral mixing on a phytoplankton bloom: Distribution in the Kerguelen Plateau region. *Deep Sea Res. Part I*, **56**, 963–973.
- Marshall, J., A. Adcroft, C. Hill, L. Perelman, and C. Heisey, 1997: A finite-volume, incompressible Navier Stokes model for studies of the ocean on parallel computers. *J. Geophys. Res.*, **102** (C3), 5753–5766, doi:10.1029/96JC02775.

- Marshall, J. and K. Speer, 2012: Closure of the meridional overturning circulation through Southern Ocean upwelling. *Nat. Geosci.*, **5** (3), 171–180.
- Martin, A. P., K. J. Richards, A. Bracco, and A. Provenzale, 2002: Patchy productivity in the open ocean. *Glob. Biogeochem. Cycles*, **16** (2), 9–1, doi:10.1029/2001GB001449.
- Martin, J. H., 1990: Glacial-interglacial CO₂ change: The iron hypothesis. *Paleoceanogr.*, **5** (1), 1–13.
- Mayewski, P. A., et al., 2009: State of the Antarctic and Southern Ocean climate system. *Rev. Geophys.*, **47** (1).
- Mazloff, M. R., P. Heimbach, and C. Wunsch, 2010: An Eddy-Permitting Southern Ocean State Estimate. *J. Phys. Oceanogr.*, **40** (5), 880–899.
- McCartney, M. S. and K. A. Donohue, 2007: A deep cyclonic gyre in the Australian–Antarctic Basin. *Progr. Oceanogr.*, **75** (4), 675–750, doi:10.1016/j.pocean.2007.02.008.
- McGillicuddy, D. J., et al., 2007: Eddy/wind interactions stimulate extraordinary mid-ocean plankton blooms. *Science*, **316** (5827), 1021–1026.
- McGillicuddy Jr, D. and A. Robinson, 1997: Eddy-induced nutrient supply and new production in the Sargasso Sea. *Deep Sea Res. Part I*, **44** (8), 1427–1450.
- McWilliams, J. C., J. Molemaker, and I. Yavneh, 2001: From stirring to mixing of momentum: Cascades from balanced flows to dissipation in the oceanic interior. Tech. rep., DTIC Document.
- McWilliams, J. C. and M. J. Molemaker, 2011: Baroclinic frontal arrest: A sequel to unstable frontogenesis. *J. Phys. Oceanogr.*, **41** (3), 601–619.
- Mensa, J. A., Z. Garraffo, A. Griffa, T. M. Özgökmen, A. Haza, and M. Veneziani, 2013: Seasonality of the submesoscale dynamics in the Gulf Stream region. *Ocean Dynamics*, **63** (8), 923–941.
- Molemaker, M. J., J. C. McWilliams, and I. Yavneh, 2005: Baroclinic instability and loss of balance. *J. Phys. Oceanogr.*, **35** (9), 1505–1517.
- Mongin, M., E. Molina, and T. W. Trull, 2008: Seasonality and scale of the Kerguelen plateau phytoplankton bloom: A remote sensing and modeling analysis of the influence of natural iron fertilization in the Southern Ocean. *Deep Sea Res. Part II*, **55**, 880–892.
- Mongin, M. M., E. R. Abraham, and T. W. Trull, 2009: Winter advection of iron can explain the summer phytoplankton bloom that extends 1000 km downstream of the Kerguelen Plateau in the Southern Ocean. *J. Mar. Res.*, **67**, 225–237.
- Moore, J. and O. Braucher, 2008: Sedimentary and mineral dust sources of dissolved iron to the world ocean. *Biogeochem.*, **5** (3).

- Moore, J. K., S. C. Doney, and K. Lindsay, 2004: Upper ocean ecosystem dynamics and iron cycling in a global three-dimensional model. *Glob. Biogeochem. Cycles*, **18** (4), doi:10.1029/2004GB002220.
- Naveira-Garabato, A. et al., 2009: RRS James Cook Cruise 29, 01 Nov-22 Dec 2008. SOFine Cruise Report: Southern Ocean. *Southampton, UK: National Oceanography Centre, Southampton, 216pp. (National Oceanography Centre Southampton Cruise Report, No.35).*
- Nikurashin, M., G. K. Vallis, and A. Adcroft, 2013: Routes to energy dissipation for geostrophic flows in the southern ocean. *Nat. Geosci.*, **6** (1), 48–51.
- Orsi, A. H., T. Whitworth, and W. D. Nowlin, 1995: On the meridional extent and fronts of the Antarctic Circumpolar Current. *Deep Sea Res. Part I*, **42** (5), 641–673.
- Parekh, P., M. J. Follows, and E. Boyle, 2004: Modeling the global ocean iron cycle. *Glob. Biogeochem. Cycles*, **18** (1), doi:10.1029/2003GB002061.
- Paris, C. B., J. Helgers, E. van Sebille, and A. Srinivasan, 2013: Connectivity Modeling System: A probabilistic modeling tool for the multi-scale tracking of biotic and abiotic variability in the ocean. *Environ. Modell. Softw.*, **42**, 47–54.
- Park, Y.-H., I. Durand, E. Kestenare, G. Rougier, M. Zhou, F. d'Ovidio, C. Cotté, and J.-H. Lee, 2014: Polar Front around the Kerguelen Islands: An up-to-date determination and associated circulation of surface/subsurface waters. *J. Geophys. Res.*, **119** (10), 6575–6592, doi:10.1002/2014JC010061.
- Park, Y.-H., J.-L. Fuda, I. Durand, N. Garabato, and C. Alberto, 2008a: Internal tides and vertical mixing over the Kerguelen Plateau. *Deep Sea Res. Part II*, **55**, 582–593.
- Park, Y.-H., F. Roquet, I. Durand, and J.-L. Fuda, 2008b: Large-scale circulation over and around the Northern Kerguelen Plateau. *Deep Sea Res. Part II*, **55**, 566–581.
- Park, Y.-H., F. Vivier, F. Roquet, and E. Kestenare, 2009: Direct observations of the ACC transport across the Kerguelen Plateau. *Geophys. Res. Lett.*, **36** (18), doi:10.1029/2009GL039617.
- Phillips, H. E. and N. L. Bindoff, 2014: On the non-equivalent barotropic structure of the Antarctic Circumpolar Current: An observational perspective. *J. Geophys. Res.*, **119**, doi:10.1002/2013JC009516.
- Planquette, H., et al., 2007: Dissolved iron in the vicinity of the Crozet Islands, Southern Ocean. *Deep Sea Res. Part II*, **54** (18), 1999–2019.
- Resplandy, L., M. Lévy, F. D'Ovidio, and L. Merlivat, 2009: Impact of submesoscale variability in estimating the air-sea CO₂ exchange: Results from a model study of the POMME experiment. *Glob. Biogeochem. Cycles*, **23** (1), GB1017, doi:10.1029/2008GB003239.

- Sabine, C. L., et al., 2004: The oceanic sink for anthropogenic CO₂. *Science*, **305** (5682), 367–371.
- Sarthou, G., D. Vincent, U. Christaki, I. Obernosterer, K. R. Timmermans, and C. P. Brussaard, 2008: The fate of biogenic iron during a phytoplankton bloom induced by natural fertilisation: Impact of copepod grazing. *Deep Sea Res. Part II*, **55** (5), 734–751.
- Sigman, D. M., M. P. Hain, and G. H. Haug, 2010: The polar ocean and glacial cycles in atmospheric CO₂ concentration. *Nature*, **466** (7302), 47–55.
- Smith, W. H. F. and D. T. Sandwell, 1997: Global sea floor topography from satellite altimetry and ship depth soundings. *Science*, **277** (5334), 1956–1962.
- Sokolov, S. and S. R. Rintoul, 2009a: Circumpolar structure and distribution of the Antarctic Circumpolar Current fronts: 1. Mean circumpolar paths. *J. Geophys. Res.*, **114** (C11), C11 018, doi:10.1029/2008JC005108.
- Sokolov, S. and S. R. Rintoul, 2009b: Circumpolar structure and distribution of the Antarctic Circumpolar Current fronts: 2. Variability and relationship to sea surface height. *J. Geophys. Res.*, **114** (C11), C11 019, doi:10.1029/2008JC005248.
- Swart, S., S. Thomalla, and P. Monteiro, 2014: The seasonal cycle of mixed layer dynamics and phytoplankton biomass in the Sub-Antarctic Zone: A high-resolution glider experiment. *J. Mar. Sys.*, doi:10.1016/j.jmarsys.2014.06.002.
- Tagliabue, A., T. Mtshali, O. Aumont, A. Bowie, M. Klunder, A. Roychoudhury, and S. Swart, 2012: A global compilation of dissolved iron measurements: focus on distributions and processes in the Southern Ocean. *Biogeosc.*, **9** (6), 2333–2349.
- Tagliabue, A., J.-B. Sallée, A. R. Bowie, M. Lévy, S. Swart, and P. W. Boyd, 2014: Surface-water iron supplies in the Southern Ocean sustained by deep winter mixing. *Nat. Geosci.*, **7** (4), 314–320.
- Takahashi, T., C. Sweeney, B. Hales, D. W. Chipman, T. Newberger, J. G. Goddard, R. A. Iannuzzi, and S. C. Sutherland, 2012: The changing carbon cycle in the Southern Ocean. *Oceanogr.*, **25** (3).
- Talley, L. D., 2013: Closure of the global overturning circulation through the Indian, Pacific, and Southern Oceans: Schematics and transports. *Oceanogr.*, **26** (1), 80–97.
- Talley, L. D., G. L. Pickard, W. J. Emery, and J. H. Swift, 2011: *Descriptive Physical Oceanography: An Introduction*. Academic press.
- Taylor, J. R. and R. Ferrari, 2011: Ocean fronts trigger high latitude phytoplankton blooms. *Geophys. Res. Lett.*, **38** (23), doi:10.1029/2011GL049312.
- Thomas, L. and R. Ferrari, 2008: Friction, frontogenesis, and the stratification of the surface mixed layer. *J. Phys. Oceanogr.*, **38** (11), 2501–2518.

- Thomas, L. N., A. Tandon, and A. Mahadevan, 2008: *Submesoscale processes and dynamics*, 17–38. Wiley Online Library.
- Thompson, A. F. and J.-B. Sallée, 2012: Jets and topography: Jet transitions and the impact on transport in the Antarctic Circumpolar Current. *J. Phys. Oceanogr.*, **42** (6), 956–972.
- Toggweiler, J. and B. Samuels, 1995: Effect of Drake passage on the global thermohaline circulation. *Deep Sea Res. Part I*, **42** (4), 477–500.
- van Beek, P., M. Bourquin, J.-L. Reyss, M. Souhaut, M. Charette, and C. Jeandel, 2008: Radium isotopes to investigate the water mass pathways on the Kerguelen Plateau (Southern Ocean). *Deep Sea Res. Part II*, **55** (5), 622–637.
- van Sebille, E., P. J. van Leeuwen, A. Biastoch, C. N. Barron, and W. P. M. de Ruijter, 2009: Lagrangian validation of numerical drifter trajectories using drifting buoys: Application to the Agulhas system. *Ocean Modell.*, **29**, 269–276.
- Völker, C. and A. Tagliabue, 2014: Modeling organic iron-binding ligands in a three-dimensional biogeochemical ocean model. *Mar. Chem.*, doi: 10.1016/j.marchem.2014.11.008.
- Ward, M. L. and A. M. Hogg, 2011: Establishment of momentum balance by form stress in a wind-driven channel. *Ocean Modell.*, **40** (2), 133–146.